UNIVERSITY OF CALIFORNIA SAN DIEGO

# Using the Biophotonic Toolbox to Study Neurodegeneration In Vitro

A dissertation submitted in partial satisfaction of the
requirements for the degree Doctor of Philosophy

in

Bioengineering

by

Christopher Carmona

Committee in charge:

Professor Michael W. Berns, Chair
Professor Yingxiao Wang, Co-Chair
Professor William C. Mobley
Professor Alexandra Newton
Professor Daryl C. Preece

2022

The Dissertation of Christopher Carmona is approved, and it is acceptable in quality and form for publication on microfilm and electronically.

University of California San Diego

2022

TABLE OF CONTENTS

LIST OF FIGURES

# LIST OF TABLES

# ACKNOWLEDGEMENTS

This research was supported by grants from the Beckman Laser Institute Foundation, the Institute of Engineering and Medicine, the Air Force Office of Scientific research under FA9550-14-1-0034, and the National Institute for Neurological Disorders and Stroke of the National Institutes of Health under P01NS092525-01A1.

Chapter 2, in part, is co-authored by Janna Sage and Sicily Panattil. Janna Sage contributed a significant portion of evaporative rate measurements. Sicily Panattil contributed greatly to the design and to the fabrication of a 3D printed mold used to investigate evaporation mitigation studies with a PDMS based lid. The dissertation author was the primary author of this chapter.

Chapter 3, in part, is co-authored with Weishan Li and Janna Sage. Figure 3.3 and Figure 3.4 were produced by Weishan Li. Weishan contributed greatly to the development of our GUI-based, Fluorescence Emissions Signal Analyzer (FESA) with a particular focus on batching and ROI segmentation. Janna Sage aided in both the collection of calcium-imaging data, presented in the results throughout the chapter, and the routine maintenance of cultures used throughout these studies. The dissertation author was the primary author of this chapter.

# VITA

2015 Bachelor of Science, Biophysics, University of California, Los Angeles

2018 Master of Science, Bioengineering, University of California, San Diego

2022 Doctor of Philosophy, Bioengineering, University of California, San Diego

# PUBLICATIONS

Wakida, N.W.**,** Gomez-Godinez, V., Li, H.,Nguyen, J., Kim, E.K., Dynes, J., Othy, S., Lau,. A.L., Ding, P., Shi, L., **Carmona, C.,** Thompson, L.M.,Cahalan, M.D., Berns, M.W, "Calcium Dynamics in astrocytes during phagocytosis*," Front. Bioeng. Biotechnol.*, Published 27 August 2020.

Gomez-Godinez, V., Morar, V., **Carmona, C.**, Gu, Y., Sung, K., Shi, L.Z., Wu, C., Preece, D., and Berns, M.W., "Laser-Induced Shockwave (LIS) to Study Neuronal Ca2+ Responses," *Front. Bioeng. Biotechnol.*, Published 16 February 2021.\

**Carmona, C.**, Preece, D., Gomez-Godinez, V., Zhi, L.Z., Berns, M.W., "Probing mechanobiology with laser-induced shockwaves," *Proc. Of Optics and Photonics, Optical Trapping and Optical Manipulation XIV*, San Diego, California. SPIE. 25 August 2017

DeVore, P., Jiang, Y., Lynch, M., Miyatake, T., **Carmona**, **C.**, Chan, A.C, Muniam, K., and Jalali, B., "Silicon Photonics Cloud (SiCloud)," Proc. SPIE 9367, Silicon Photonics X, 93670G. 27 Feburary 2015, Doi:10.117/12.2077331.

**Carmona, C.**, Langan, P., Smith, J.C., and Petridis L., "Why Genetic Modification of Lignin Leads to Low-Recalcitrance Biomass." Physical Chemistry Chemical Physics.17(1):358-364. 7 January 2015. Doi:10.1039/c4cp05004e.

# PRESENTATIONS

"Characterization of Forces Imparted on Cells Using Laser-Induced Shockwaves". IEM 10th Anniversary Symposium. Poster. October 2018

"Characterization of Forces Imparted on Cells Using Laser-Induced Shockwaves". Presentation only. Proc. SPIE 10723, Optical Trapping and Optical Micromanipulation XV, 107230D, 17 September 2018.

"Characterization of Forces Imparted on Cells Using Laser-Induced Shockwaves". Poster. Siegman International School on Lasers. Poster. August 2018.

"Characterization of Forces Imparted on Cells Using Laser-Induced Shockwaves" Poster. University of California, San Diego, Jacobs Research Expo. April 2018.

"Characterization of Forces Imparted on Cells Using Laser-Induced Shockwaves" Poster. Bioengineering Day. April 2018.

“Understanding Neurodynamics Through Light Field Microscopy.” 20th International C. Elegans Meeting; 2015 June 24; Los Angeles, CA, United States of America. Genetics Society of America; c2015.

“Simulation Analysis of the Effects of Partial Charge Modifications on the Hydrophobicity of Lignin,” Proc. of 80th Annual Meeting of the APS Southeastern Section. American Physical Society. Sloan Convention Center, Bowling Green, Kentucky. 22 November 2013.

## FIELDS OF STUDY

Major Field: Bioengineering

Studies in Biophotonics
Professor Michael W. Berns

Studies in Neuroscience
Professor William C. Mobley

# ABSTRACT OF THE DISSERTATION

## Using the Biophotonics Toolbox to Study Neurodegeneration In Vitro

by

Christopher Carmona

Doctor of Philosophy in Bioengineering

University of California San Diego, 2022

Professor Michael W. Berns, Chair
Professor Yingxiao Wang, Co-Chair

In neurons, intracellular calcium has the dual role of charge carrier and intracellular messenger. The signaling function of calcium has aspects that are particularly important to neurons. Synaptic transmission, the form of secretion that leads to the release of neurotransmitters, the process of learning and the formation and consolidation of memory, long term potentiation or depression of synaptic transmission, the direct coupling between depolarization of the plasma membrane and the increase of intracellular calcium are all under the control of calcium signals. Neuronal viability depends on proper functioning of all these processes and to a greater degree depend on the precise temporal and spatial regulation of calcium signals than most other eukaryotic cells.

The primary focus of this work is the development of experimental and analytical tools for studies of chronic neurodegenerative disorders. This work investigates the spontaneous calcium activity in primary, dissociated cortical neurons as compared to Huntington’s disease (HD) model cells. The relative fluorescence variation of calcium-sensitive Fluo 4 is measured and analyzed using a custom, GUI-based software tool: Fluorescence Emissions Signal Analyzer (FESA). Characterization of intracellular calcium activity with well-defined parameters within emissions signal activity across several timepoints throughout incubation highlight calcium dysregulation among HD model cells. In addition, methods for optimizing the viability of long-term neuronal cultures are investigated and discussed. Furthermore, a fluorescence microscopy system capable of measuring and generating optically-coupled shear stresses via laser-induced shockwaves is described. Shear stress induced by laser-induced shockwaves is a contactless model for traumatic brain injury (TBI) in vitro that offers high levels of reproducibility and spatiotemporal precision. Results from this work have potential applications towards high-throughput methods for the discovery of novel, therapeutic avenues for chronic neurodegenerative disorders such as HD and TBI.

# Chapter 1: Introduction

## 1.1. Intracellular Calcium

Early life on earth consisted of single cells with the capacity to carry out all vital functions. While successful, unicellular life inherently restricts the interplay between cells to competition for nutrients. At some point competition between organisms was replaced by cooperation, and multicellular life evolved. Cooperation between cells naturally demands communication and the development of agents that could exchange messages between cells. The increasing complexity of multicellular organization drove the evolution of cells with distinct functional tasks. The number of intracellular signaling molecules as well as the degree of their complexity increased. Thus, multicellular life brought with it both intercellular and intracellular exchange of messages as an additional, but essential, regulation category. The third most abundant metal found in nature, calcium, was amply available to cells at early evolutionary stages, which led to its adoption as a regulator.[1]

While the basic principles of calcium regulation were already present in prokaryotes and protists,[2,3] calcium regulation gradually grew to cover nearly all aspects of cell function after the transition to multi-cellularity. Calcium signaling is ubiquitous across cell biology and linked to various functions including metabolism, membrane transport, hormonal regulation, and motility. In animal fluids and tissues, the concentration of calcium varies between 2.1 and 2.6 mM, sub-divided in three forms: the ionized form ($Ca^{2+}$), complexed to organic compounds, and bound to small molecular weight inorganic molecules.[4] While the equilibrium among these three forms in the extracellular spaces may vary somewhat, the proportion of ionized calcium is generally not distant from that of complexed calcium. Total calcium concentration is on the order of millimolar inside cells, however, the cytosol of most cells have calcium concentrations that are about 10,000-fold lower. This nanomolar concentration is achieved by the ligation of calcium to specific proteins that contain sites with the necessary affinity and specificity for $Ca^{2+}$. There are two broad classes of proteins with roles in the regulation of calcium. The first class of proteins are soluble in the cytoplasm, sequestered inside cellular organelles, or organized in insoluble non-membranous structures such as the cytoskeleton. This class of proteins buffers $Ca^{2+}$ to the nanomolar range without modifying its total content in cells. In addition, this class of proteins serve as intermediate messengers that change conformation upon $Ca^{2+}$-binding and transmit signals to secondary targets to which they bind. In this manner, $Ca^{2+}$ is considered a second messenger[5] by regulating specific protein targets during signal transduction. Interestingly, $Ca^{2+}$ has the property of auto-regulation, which is distinctive among second messengers; in other words protein systems that control cellular $Ca^{2+}$ may be regulated by $Ca^{2+}$ itself. [6] The second class of proteins that control cell $Ca^{2+}$ are intrinsic to membranes, and transports $Ca^{2+}$ in or out of cells, or between the cytosol and the lumen of the organelles.

In neurons, intracellular calcium has the dual role of charge carrier and intracellular messenger. Like other cells, neurons use both extracellular and intracellular sources of calcium. However, unlike other cells, the signaling function of $Ca^{2+}$ has aspects that are peculiar and particularly important to neurons. Synaptic transmission, the form of secretion that leads to the release of neurotransmitters, the process of learning and the formation and consolidation of memory, long term potentiation (LTP) or depression of synaptic transmission, the direct coupling between depolarization of the plasma membrane and the increase of intracellular $Ca^{2+}$ are all under the control of $Ca^{2+}$ signals. [6] Neuronal viability depends on proper functioning of all these processes and to a greater degree depend on the precise temporal and spatial regulation of $Ca^{2+}$ signals than most other eukaryotic cells.

Several $Ca^{2+}$ binding proteins are expressed in the nervous system. They can be functionally categorized into two groups: the $Ca^{2+}$ buffers and the $Ca^{2+}$ sensors. The $Ca^{2+}$ buffers control the duration and the spread of $Ca^{2+}$ signals with the aid of $Ca^{2+}$ clearance mechanisms. The $Ca^{2+}$ sensors translate changes in $Ca^{2+}$ concentration into specific signals. Calmodulin (CaM) is the best known among them and the molecular mechanisms by which it decodes $Ca^{2+}$ has been determined. Fluctuations in intracellular $Ca^{2+}$ not only alter the subcellular distribution but also induce different conformational states of CaM that result in target-specific activation. [6,7] The major target proteins of CaM are $Ca^{2+}$/CaM-dependent kinases (CaMK) and the phosphatase calcineurin, which contribute to several neuronal regulatory pathways involved in synaptic plasticity and gene expression. [6] While a clear distinction between $Ca^{2+}$ buffers and $Ca^{2+}$ sensors are not always straightforward since, sensors also buffer calcium through binding. CaM is the best example of this dual nature as it is present in the brains at high concentrations of up to 100 µM. [6] The majority of $Ca^{2+}$ buffers have dissociation constants in the low micromolar range therefore, in a resting cell they are mostly in their $Ca^{2+}$-free forms. Several studies in knock-out mice have revealed that the deletion of one $Ca^{2+}$ binding protein is not compensated by the overexpression of others, which highlights the importance of varying quantities of proteins within

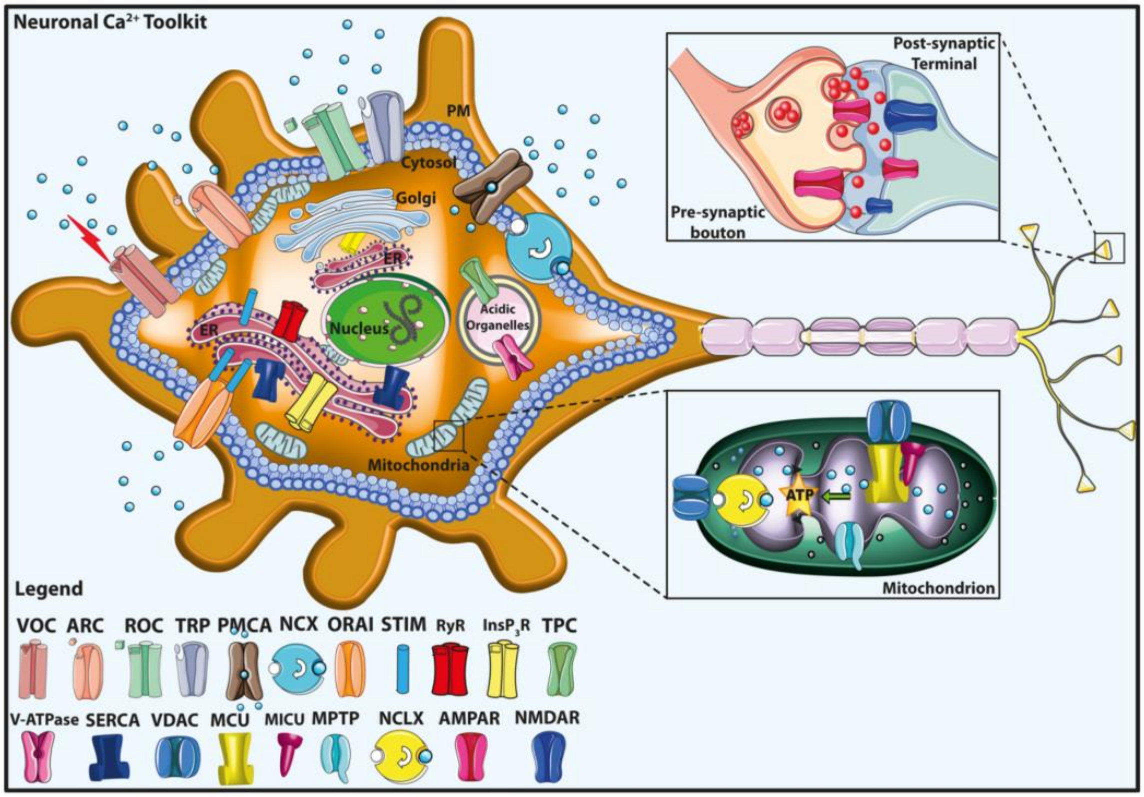

Figure 1.1 - Neuronal calcium (Ca2+) signaling toolkit. The Ca2+ transport proteins, the receptors of the plasma membrane (PM), and the intracellular organelles, including mitochondria, endoplasmic reticulum (eR), Golgi apparatus, and acidic organelles, are indicated. The mitochondrial Ca2+ handling systems (proteins) are shown in greater detail in the bottom right *inset*. The *top right inset* shows a schematic view of the pre-synaptic bouton and the post-synaptic termination. The legend on the *bottom left* indicates the Ca2+ transporter proteins. *VOC* voltage-gated Ca2+ channel, *ROC* receptor-operated Ca2+ channel, *ORAI* the pore-forming subunit of store-operated Ca2+ entry channel (*SOC*), *STIM* the Ca2+ sensor, *TPC* two-pore channel, *ARC* arachidonic acid-regulated Ca2+ channel, *TRP* transient receptor potential channel, *PMCA* plasma membrane Ca2+ ATPase, *V-ATPase* vacuolar H+ ATPase, *InsP3R* inositol 1,4,5 tris–phosphate receptors, *RyR* ryanodine receptor, *NCX* plasma membrane Na+/Ca2+ exchanger, *SERCA* sarco-/endoplasmic reticulum Ca2+ ATPase, *MCU* mitochondrial Ca2+ uniporter, *MICU* mitochondrial Ca2+ uniporter regulator, *NCLX* mitochondrial Na+/Ca2+ exchanger, *VDAC* voltage-dependent anion channels, *MPTP* mitochondrial permeability transition pore, *AMPAR* 2-amino-3-hydroxy-5-methyl-4-isoxazolepropionic acid receptor, *NMDAR N*-methyl-d-aspartate receptor. [6]

respective cell types.[6] The restricted expression in particular classes of neurons and their high Ca$^{2+}$ sensitivity contribute towards the non-redundancy of Ca$^{2+}$ sensor proteins with respect to CaM. [6]

Plasma membrane $Ca^{2+}$ channels are traditionally divided into groups according to their mechanism of operation: the voltage-gated $Ca^{2+}$ channels (VOC), the receptor-operated $Ca^{2+}$ channels (ROC), and the store-operated $Ca^{2+}$ entry channels (SOC), which are activated upon depletion of cellular $Ca^{2+}$ stores. The VOC transduce electrical signals occurring at the cell surface membrane resulting from local rises of intracellular $Ca^{2+}$. In neurons, the VOC mediate the generation and propagation of the nerve impulses and aid in cell homeostasis. [6] The ROC are activated upon the binding of specific ligands, such as neurotransmitters, to receptors in their extracellular domain. Several prevalent $Ca^{2+}$ channels are shown in **Figure 1.1**[6] and described in further detail below.

The main excitatory neurotransmitter in the mammalian brain is L-glutamate and it activates two classes of receptors: the ionotropic receptors (iGluRs), and the metabotropic receptors (mGluRs). Alpha-amino-3-hydroxy-5-methyl-4-isoxazole propionic acid-sensitive receptors (AMPARs) and *N*-methyl-d-aspartate sensitive receptors (NMDARs) are the two principal types of ionotropic glutamate receptors. [6] AMPARs mediate fast excitatory synaptic transmission in the mammalian central nervous system (CNS), and are permeable to $Na^{+}$ and $K^{+}$, but may also become permeable to $Ca^{2+}$. NMDARs are permeable to both $Na^{+}$, which contributes to postsynaptic depolarization, and $Ca^{2+}$, which generates $Ca^{2+}$ transients and determines intracellular physiological responses. [6] NMDAR activation not only requires glutamate, but also membrane depolarization, which removes $Mg^{2+}$ that normally blocks the channel. Thus, NMDARs respond to glutamate relatively slower than AMPARs. NMDARs can be found in extra- and postsynaptic sites. Interestingly, studies have found that certain pro-death pathways are preferentially activated by extra-synaptic NMDARs via translocation of the Forkhead transcription factor FoxO3a into the nucleus.[6,8] According to the theory of neuronal health[9], neurons can exist in a dynamic spectrum of states that consists of extremes from fully-functional and resilient to dysfunctional and vulnerable to insults. A neuron may be influenced by a multitude of signals and stimuli, but it is understood to shift towards health and robustness by synaptic NMDAR activity. Episodes of synaptic NMDAR activity promote neuroprotection that lasts beyond the duration of the episode and continues after signaling pathways are no longer active. [10] NMDAR activity is typically augmented by release from internal stores, after which $Ca^{2+}$ is transduced to the cell soma where it enters the nucleus. [10] Nuclear $Ca^{2+}$ is a potent activator of neuronal gene expression. One important target of nuclear $Ca^{2+}$ is the nuclear $Ca^{2+}$/ calmodulin-dependent protein (CaM) kinase IV and the transcription factor cyclic-AMP response element binding protein (CREB). [10] CREB is the prototypical signal-regulated transcription factor, whose role in neuronal survival and several other processes that include synaptic plasticity, addiction, neurogenesis, and learning and memory is well documented. [6,11-15] In hippocampal neurons, CREB-dependent gene expression is causally linked to the long-lasting phase of activity-dependent neuroprotection against apoptotic and excitotoxic insults. [6] This form of neuroprotection is dependent on nuclear $Ca^{2+}$ signaling. Another target of synaptic NMDAR and nuclear $Ca^{2+}$-CREB signaling is the gene that encodes the neurotrophin brain-derived neurotrophic factor (BDNF). [6] BDNF has neuroprotective properties[16] and can rescue neurons from NMDAR blockade-induced neuronal death.[17] The mGluRs are coupled to G proteins and are homodimers that are organized by their seven transmembrane domains. They are encoded by eight genes (mGluR1-8) and generate $Ca^{2+}$ signals through the activation of downstream signaling cascades that activate phospholipase C and activate, or inhibit, adenylyl cyclase. They are expressed in neuronal and glial cells in the brain, spinal cord, and peripheral neurons with mGluR1 most abundantly expressed in the mammalian CNS. [6] There are two types of neuronal depolarization that are produced, the first a rapid transient depolarization related to the release of $Ca^{2+}$ from intracellular stores and a prolonged and larger depolarization resulting from the activation of TRP channels. TRP channels are a class of channels localized in the endoplasmic reticulum (ER) and Golgi membranes that can generate changes in intracellular $Ca^{2+}$ concentration either directly as an entryway or indirectly by causing cell depolarization and triggering VOCs.

The plasma membrane $Ca^{2+}$ ATPase (PMCA) and the plasma membrane $Na^{+}/Ca^{2+}$ exchanger (NCX) are the two systems responsible for $Ca^{2+}$ extrusion to the extracellular environment. [6] PMCA pumps belong to the family of P-type ATPases, which are characterized by the temporary conservation of ATP energy in the form of a phosphorylated enzyme intermediate. CaM a calcium-buffering protein with a dissociation constant in the nanomolar range, interacts directly with the PMCA pump. [6,18] In the absence of CaM, the C-terminal tail of the pump folds over, binding two sites in the main body leading to auto-inhibition. CaM binding to the C-terminal domain relieves auto-inhibition. PMCA pumps are ubiquitously expressed; however, the four basic isoforms (PMCA1,-2,-3,and -4) are specifically distributed amongst different tissues, with isoforms 2 and 3 being especially abundant in neurons. The NCX accomplishes $Ca^{2+}$ extrusion by using the electrochemical gradient of Na+: during each cycle three Na+ ions enter the cell and one $Ca^{2+}$ ion is extruded against its gradient. Three different genes encoding NCX isoforms (NCX1,-2,-3) have been identified, however, all three basic NCX isoforms are essentially co-expressed in brain neurons. [6] Thus, making it difficult to attribute specific functions to each isoform. NCX can also work in reverse since, the direction of the movement of transported ions depends on the electrochemical gradients of $Na^+$ and $Ca^{2+}$.

The SOC are activated by the release of $Ca^{2+}$ from the ER. While they were initially described in non-excitable cells, they have been documented in other cell types such as neurons and skeletal muscle cells. Stromal interacting molecules (STIMs) are calcium-sensor proteins that have a $Ca^{2+}$ binding domain located in the ER lumen. During ER calcium store depletion, STIMs oligomerize, subsequently translocate to the plasma membrane and interact with calcium-conducting channels, composed of ORAI sub-units, to induce calcium influx and store refilling. This process is referred to as store-operated calcium entry (SOCE). [6] SOCE was originally proposed as a mechanism for assuring the refilling of intracellular calcium stores. [19] More recently, the notion has emerged that the influx through this pathway may provide direct $Ca^{2+}$ signals to targets localized to spatially restricted areas close to the sites of $Ca^{2+}$-entry thus, initiating specific signaling pathways.[6]

The release of Ca2+ from the ER occurs in neurons via two types of $Ca^{2+}$ channels/receptors: ryanodine receptors (RyR) and inositol-1,4,5-tris-phosphate receptors (InsP3Rs).[5,6] While InsP3Rs are ubiquitously expressed in many cell types, RyRs are more characteristic of neurons and muscle cells. Activation of various G-protein-coupled receptors on the cell membrane precedes release and, subsequent, binding of second messenger InsP3 to InsP3Rs, which then triggers $Ca^{2+}$ release. Increased cytoplasmic levels of intracellular calcium is a major trigger for $Ca^{2+}$ release via RyRs and is often referred to as calcium-induced calcium release (CICR). RyRs are also regulated by other intraneuronal messengers such as cyclic adenosine diphosphate ribose (cADP-ribose). $Ca^{2+}$ reuptake in the ER is mediate by the P-type $Ca^{2+}$ ATPase SERCA pump that replenishes stores and thus, together with PMCA and the NCX, re-establishes resting cytosolic $Ca^{2+}$ values after a $Ca^{2+}$ transient induced by cell stimulation. [6] The SERCA pump is ubiquitously distributed in tissues and has no distinctive characteristic in neurons.

Mitochondria are also major players in the regulation of $Ca^{2+}$ signals. These organelles participate in both $Ca^{2+}$ buffering and sub-cellular signaling with the ER that permit them to take advantage of localized $Ca^{2+}$ release by vicinal ER channels and to accumulate $Ca^{2+}$ in the matrix. $Ca^{2+}$ regulates the ability of mitochondria to provide ATP to energy-demanding processes by boosting the activity of three enzymes: pyruvate dehydrogenase (indirectly via its phosphatase activation), isocitrate dehydrogenase, and α-ketoglutarate dehydrogenase (by binding directly to the enzymes). [6] The mitochondrial electrophoretic uniporter (MCU) mediates the entry of $Ca^{2+}$ into the mitochondrial matrix and is driven by the negative membrane potential generated by activity of the respiratory chain components of the inner membrane. [6] A mitochondrial NCX (NCLX) mediates the efflux of $Ca^{2+}$ from the mitochondria. [6] Similarly, $Ca^{2+}$ efflux can be mediated by the transient opening of the mitochondrial permeability transition pore (mPTP). [6]

A primary motivation for this dissertation is a novel characterization of intracellular calcium activity. In order to do so 1) methods for establishing reproducibly, viable cultures are validated, 2) analytical tools are developed to interpret calcium-sensitive fluorescent dye emissions data 3) statistical comparisons of well-defined parameters are performed between disease model neurons and wild type controls across several days of incubation.

## 1.2. Calcium Dysregulation

Calcium toxicity results from two primary groups of mechanisms.[20] The first are mechanisms that sustain the excess accumulation of intracellular calcium concentrations ($[Ca^{2+}]_i$). Typical mechanisms that disrupt $[Ca^{2+}]_i$ homeostasis include oxidative stress, endoplasmic reticulum stress, mitochondrial dysregulation, abnormal aggregation and/or interaction of proteins (e.g. Aβ, α-synuclein, and mutant Huntingtin protein (mHtt)). [20] The second group are phenomena that are precipitated by the excess accumulation of $[Ca^{2+}]_i$.

The original calcium hypothesis[21] asserts that sustained disruption of mechanisms that normally regulate $[Ca^{2+}]_i$ signaling is pivotal for triggering adverse changes in neuronal function.[21] While the calcium hypothesis is typically associated with Alzheimer's disease and brain aging, there appear to be drastic similarities in calcium dysregulation amongst several chronic neurodegenerative disorders. The crucial challenge of the calcium hypothesis is to provide a heuristic account for the causal relationships between the phenomena of brain aging and a spectrum of chronic brain disorders. [21] The updated calcium hypothesis offers a more integrative explanation: “a decline in the functioning of a neuron is the necessary and sufficient condition that affects the performance of a neural net; it is the deterioration in the workings of a neural net that underlies impairments of behaviors and the expression of clinical phenotypes." [21] The updated hypothesis replaces the notion of healthy neuronal function vs. disease neuronal function, as a distinct dichotomy with quantitative, objective measures of performance on a continuous scale. [21] In the interest contextualizing calcium dysregulation further, I discuss examples of calcium dysregulation found in separate chronic neurodegenerative disorders that are primary subjects of this dissertation. [21]

### 1.2.1. Huntington's Disease

Huntington's disease (HD) is a dominantly inherited neurodegenerative disorder that currently has no disease-modifying treatment.[22] Mutant Huntingtin protein (mHTT) features an expanded stretch of glutamine residues (polyQ) near the N-terminus; the mutant protein induces widespread changes in neurons that affect axonal trafficking and signaling, synaptic function, gene expression, mitochondrial function, calcium homeostasis, and proteostasis. Homeostatic maintenance of calcium is essential for normal neuronal signaling; moreover, effectively modulating calcium levels protects neurons in the setting of increased neuronal excitation and calcium entry. It is well established that calcium homeostasis differs between wild-type neurons and those that model Huntington's Disease (HD).[23-30] For example, increased basal levels of intracellular calcium are present and mitochondria isolated from cells obtained from HD patients are more sensitive to calcium loading.[24] One clue to abnormal regulation comes from studies of the RyR, which is in the ER. RyR dysfunction, as reflected in R6/2 HD mouse models, is posited to cause excessive calcium leak from ER into the cytosol with consequently reduced calcium in intracellular membrane stores.[25] Increased cytosolic calcium could dysregulate the activity of calcium binding proteins, including kinases; decreased intracellular stores could blunt responses to signaling events. Another clue is that mHTT sensitizes the InsP3R, also present in the ER membrane, to IP3; this enhances calcium release in response to activation of metabotropic glutamate receptors.[23,27] Finally, there is evidence that in HD there is a relative increase in the ratio of extrasynaptic N-methyl-D-aspartate receptors (exNMDARs) to synaptic NMDARs (sNMDARs); an increased ratio of extrasynaptic to synaptic receptors has been linked to inhibition of cell survival and plasticity.[27,28] Studies of NMDAR activation point to increased duration of the calcium response, but not its peak, in HD models.

There is compelling evidence for mHTT-induced mitochondrial dysfunction and calcium dysregulation. In human tissues and HD models deficits in energy metabolism were attributed to mitochondrial dysfunction.[30] Mitochondrial transport and morphology were also impacted. Trafficking defects preceded changes in neuronal function in HD models in vitro and in vivo. [30] Reduced trafficking may be linked to changes in morphology of mitochondria. [29,31] mHTT down-regulated mitochondrial biogenesis, in HD brain and models, via reduced expression of the peroxisome proliferator-activated receptor gamma coactivator 1 alpha (PGC1a).[23] $Ca^{2+}$ buffering in mitochondria is reduced in cells expressing mHTT; the mechanism(s) is uncertain, but cells expressing mHTT show reduced mitochondrial membrane potential that depolarize at lower levels of $[Ca^{2+}]_i$.[30] $Ca^{2+}$ dysregulation also results from non-mitochondrial sources; mHTT, but not wildtype HTT, interacts directly with the Inositol 1,4,5-trisphophate receptor type 1 (InsP3R1) with dysregulation of calcium flux from the ER.[23,25] Store operated calcium entry (SOCE) may also be affected.[23]

### 1.2.2. Traumatic Brain Injury

Traumatic brain injury (TBI) is an acquired form of injury resulting from an external mechanical force resulting from rapid acceleration/deceleration due to mechanical impact, blast waves, or penetration by a projectile.[32] TBI can be characterized into three main categories: 1) a closed head injury (cTBI) also referred to as a non-penetrating or blunt injury, 2) a penetrating or open head injury (pTBI) that occurs when an object pierces the skull and breaches the dura mater damaging the brain parenchyma, or 3) an explosive blast injury (bTBI) that occurs when the brain gets hit by a high frequency blast wave generated from improvised explosive devices. [32] The first phase of injury occurs at the moment of insult and includes contusion, laceration, diffuse axonal injury, and intracranial hemorrhages. The second phase of injury are initiated at the time of insult, but do not appear clinically for hours or even days after then.

Some acute and chronic consequences of TBI are shown in **Figure 1.2**. [32] The moment of insult, a TBI patient typically experiences contusion and laceration, diffuse axonal injury, and intracranial hemorrhaging. While not discussed here, ischemia caused by a reduction in cerebral blood flow, is an important mechanism underlying secondary brain damage as well. Mechanisms detailing injury following hyperglycemia and glutamate accumulation are shown in **Figure 1.3a**. [33] The mechanisms by which elevations in $[Ca^{2+}]_i$ trigger secondary calcium-dependent

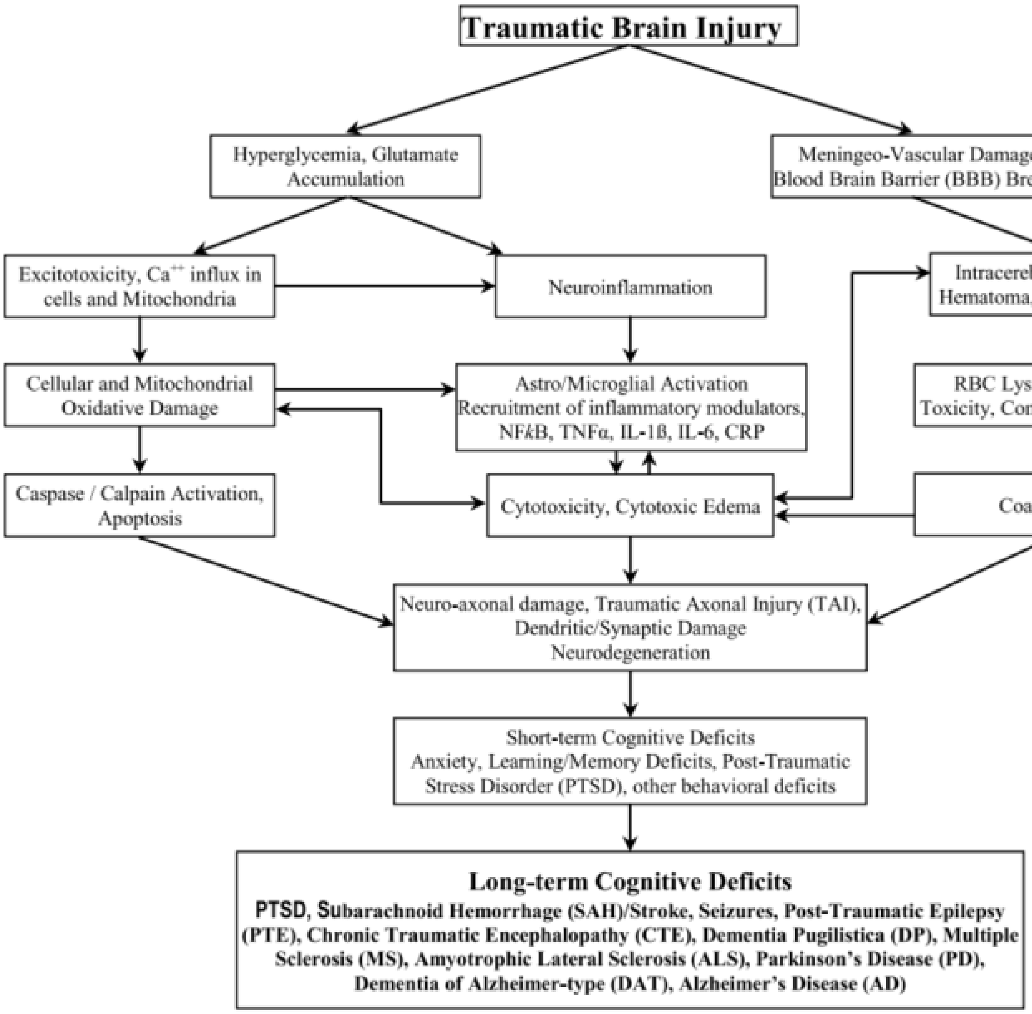

Figure 1.2 – Acute and chronic consequences of traumatic brain injury (TBI).[32]

phenomena that result in neurotoxicity are detailed in **Figure 1.3b**. [33] Upon insult or injury, trauma and ischemia work together to deplete the brain of ATP. The loss of adenosine triphosphate (ATP) leads to significant events including the breakdown of the membrane potential and depolarization, which subsequently leads to a sustained elevation in $[Ca^{2+}]_i$. As seen in **Figure 1.3b**, [33] elevation of $[Ca^{2+}]_i$ results in the biased activation of apoptotic and necrotic regulatory pathways. Moreover, the consequences of TBI generate a positive feedback cycle that initiates upon injury and appears to manifest as symptoms in patients later in time.

## 1.3. Calcium Imaging

The development of calcium imaging involved both the improvement of calcium sensors and the development of the appropriate instrumentation. Early dyes such as aequorin and arsenazo III provided early insights into calcium-dependent regulation of neuronal processes but were often tedious to implement because of dye delivery issues.[34] Roger Tsien and colleagues provided a breakthrough with more sensitive and versatile fluorescent calcium indicators resulting from the hybridization of highly calcium-selective chelators like EGTA or BAPTA with a fluorescent chromophore. [34,35] Among the first generation of fluorescent calcium indicators (quin-2, fura-2, indo-1, fluo-3) fura-2 became particularly popular among neuroscientists. Fura-2 is typically excited

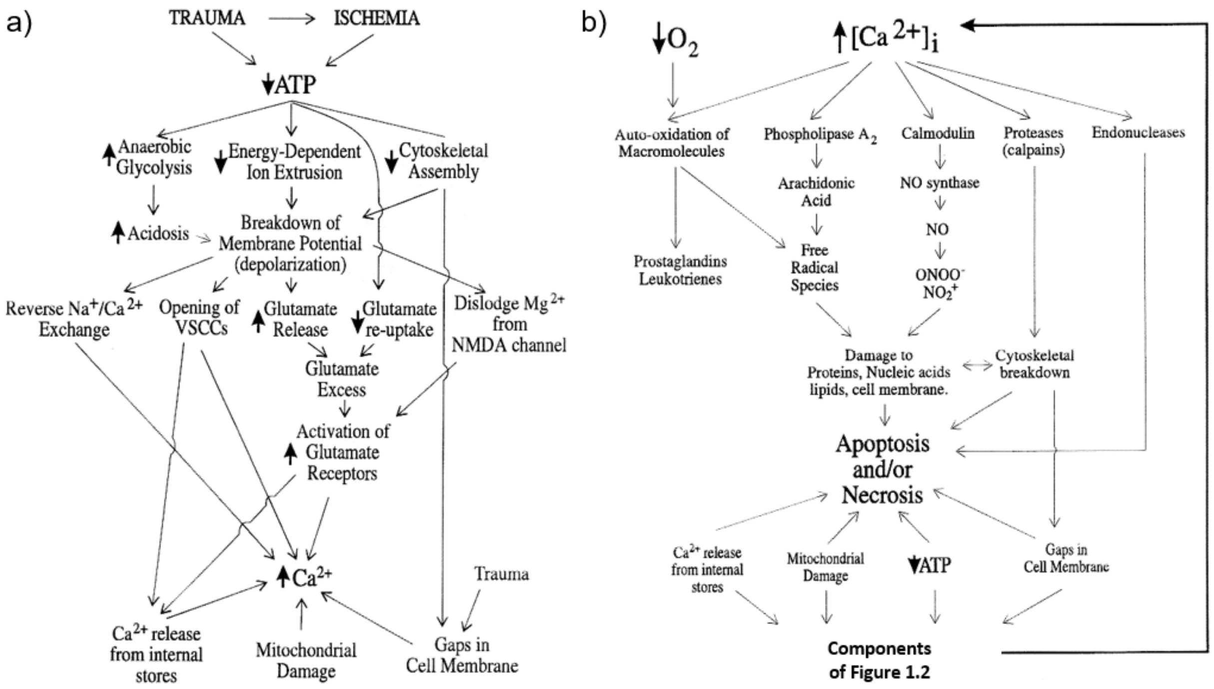

Figure 1.3 – a) Mechanisms by which trauma and ischemia produce $[Ca^{2+}]_i$ elevations. Voltage-gated $Ca^{2+}$ channel (VSCC). b) Mechanisms by which $[Ca^{2+}]_i$ elevations trigger secondary Ca-dependent phenomena, which result in neurotoxicity.[33]

at both 350 nm and 380 nm with the ratio of emissions at those wavelengths directly relating to the amount of intracellular calcium. Thus, the use of fura-2 allowed for quantitative calcium measurements based on the ratioing of signals obtained with alternating excitation wavelengths. Over several years, many calcium indicators with wide excitation spectra and affinities for calcium have been introduced and popularized for their relative ease of use and large signal-to-noise ratios. A significant next step was the introduction of protein-based genetically encoded calcium indicators (GECIs), which has seen tremendous progress to date.[34] However, GECIs will not be discussed in-depth since they will not be a primary focus in this dissertation. The development of new imaging instrumentation occurred in parallel with the development of fluorescent indicators. These developments included implementation of video imaging with CCD cameras and high-speed confocal microscopy.[34] It was the combination of higher signal strength of new fluorescent probes and emerging technology that allowed for real-time fluorescence observations of biological processes at a single-cell level. [34]

Extensive studies have been performed on Fluo 4 and various other conventional $Ca^{2+}$-sensitive indicators.[36-37] Studies have shown fluo-4 does not impair normal physiological signaling at concentrations up to 5 µM. [37] The $Ca^{2+}$-binding affinity in vitro is measured at 345 nM, however, measurements in sub-cellular regions of HeLa cells yielded 1000 nM ± 130 nM and 1260 nM ± 160 nM in the cytsol and nucleus, respectively. [36] For context, the extracellular free calcium is typically 1.2 mM while the resting cytosolic free calcium is approximately 100 nM.[34,38] During electrical activity, the concentration of intracellular calcium can rise transiently to levels that are ten to 100 times higher than resting levels. [38] Fluor 4 offers the best contrast among several indicators and was found to have a dynamic range that varies between the cytosol and nucleus with measured values of 6.0 and 15.0, respectively. [36] Generally, shorter incubation times during the dye loading procedure have appeared to reduce localization of the dye in the nuclear compartment. Typical dye loading procedures utilize calcium indicators derivatized with an acetoxymethyl (AM) ester group, which can passively diffuse across the cell membrane, and once inside the cell, esterase cleave the AM group off. [39] In this manner, concentrations of the active form of indicators within the extracellular space are minimized.

Techniques for the analysis of calcium imaging data are still being improved and developed today. The typical processing pipeline includes image denoising, motion correction, cell identification, and quantification of emissions activity. Several software packages have been written for individual aspects of the processing pipeline. Denoising while not typically required can improve the signal to noise ratio of raw imaging data that is significant at later steps of analysis. Motion correction is often required in situations where drifting of the active field-of-view may occur or from subject motion. Cell identification is performed to ensure that the quantification of emissions activity can be performed over specific regions-of-interests. The most commonly used measure of relative fluorescence variation or $\Delta F/F_0$. Where deviations in baseline $\Delta F$ are normalized relative to baseline fluorescence $F_0$. For the purposes of investigations of signal activity, a custom, GUI-based software tool referred to as Fluorescence Emissions Signal Analyzer (FESA) was developed. FESA allows complete analysis of arbitrary emissions signal activity of cell culture samples. While de-noising and motion correction are not addressed by FESA, several features are included to automate cell identification and subsequent segmentation as well as the quantification and parametrization of transient signal activity.

## 1.4. Biophotonics

Pulsed laser irradiation focused at high numerical apertures has been utilized in cellular biology to induce damage at both cellular and sub-cellular levels for over 40 years. [40,41] This technique provides the ability to reproducibly deposit energy with high spatial precision and offer a non-contact means of inducing cell damage and cellular manipulation. The first studies examining the use of photons to inactivate cells or cellular organelles were conducted by Tschachotin in 1912 using an incoherent UV light source.[40,41] A quartz microscope objective was used for these experiments to focus the 280 nm emission of a magnesium spark to a 5-μm diameter spot size on a cell. The use of incoherent UV light sources for cell manipulations was accelerated by the development of UV transmitting quartz objectives, providing the ability to focus the UV light to a sub-micrometer beam diameter by the 1950s. Further development of UV transmitting quartz objectives accelerated the use of incoherent UV light sources for use in the manipulation of cells. Despite improvements, conventional light sources offered low intensities, which required long exposure times to achieve the desired effect. In 1960, the invention of the ruby laser provided a high-intensity, collimated, monochromatic light source that reduced effective exposure times to the microsecond range. [41,42] Early experiments on mitochondrial inactivation utilize a ruby laser with pulse durations of ~500 μs and a 5-μm diameter spot size. [43,44] Shortly after, Berns and co-workers applied the newly developed pulsed wave argon ion laser to study cell repair, development, and organelle function.[45-47] The improved quality and shorter wavelength available using the argon laser allowed for smaller laser microbeam diameters than the multi-mode ruby lasers.[41] Long-pulsed irradiation is still utilized for cell-membrane permeabilization, however, a drawback of quasi-CW irradiation is that the energy deposition is based on linear absorption and generally required the staining of target structures with dyes. [41] By 1962, reductions in pulse duration followed the advent of Q-switched 3 nanosecond lasers by utilizing the ability to drive non-linear (multiphoton) processes.[48-51] Non-linear optical processes provide highly-localized energy deposition at targeted sites and allows precise cellular microsurgery without the use of exogenous dyes.[41] Among these processes is multi-photon absorption and optical or laser-induced breakdown that results in laser-induced plasma formation. The complete cycle of phenomena following laser-induced breakdown including the violent growth and collapse of a microbubble was first described by Felix and Ellis with experiments utilizing Q-switched pulses of 50 ns in duration from a neodymium glass laser.[51,52] In the 1970s aspects of bubble formation were highlighted by Lauterborn and Bolle who investigated the dynamics of the breakdown bubble by high speed photography and later, high speed holography. [53] The bubble is presumably first caused by vaporization around impurities due to absorption of laser light and, subsequent, compression and rebound that leads to the enlargement of the nuclei or by compression and rebound of pre-existing gaseous nuclei. [53] Secondary bubbles are also observed and results from compression and rebound of pre-existing nuclei since, no laser beam is present. [50] Laser-induced shockwaves (LISs) are shockwave fronts resulting from the explosive growth of a bubble induced by energy deposition at focal spots of lasers with sub-microsecond pulse-widths. The energy contained in a LIS is usually twice as large as the bubble energy. [53] The pressure pulses emitted during optical breakdown general have the same amplitude as those produced during the collapse of the emerging cavitation bubble. [53,54] Acoustic transients observed after bubble generation and collapse have similar amplitude, duration, and profile. [53,54] The average energy loss of a cavitation bubble during the first collapse is 84% thus, most of the energy is expended throughout the first cycle of growth and collapse. [54] By the 1980s, medical applications for shockwave generation and bubble dynamics were emerging mainly for intraocular microsurgery and lithotripsy of kidney stones. [50] Subsequent decades have seen a wealth of investigations on laser-induced breakdown in liquids with expanding applications in ablation of biological tissue, laser lithotripsy, photodisruption, laser-induced cell lysis, micro- and nanosurgery, and gene transfection.[51]

A primary motivation of this dissertation is to demonstrate a method for measuring shear forces imparted upon in vitro cell cultures. In order to accomplish this 1) a fluorescent microscope system was developed to accurately image laser-induced bubble cavitation events, 2) raw imaging data was re-interpreted as measurements of bubble size, 3) calculations of shear forces were performed from experimental data. Previous studies have characterized the use of laser-induced shockwaves[54,55] in vitro with applications in drug-delivery. In this dissertation, I explore the application of low-magnification objectives and the capacity of laser-induced shockwaves to model TBI in vitro.

## 1.5. In Vitro Models of Traumatic Brain Injury

Several in vitro models exist that attempt to characterize different aspects of TBI. However, here I will focus on current in vitro models for bTBI and how they compare with LISs. Blast injury has been categorized into four phases: primary bTBI is due to the shockwave, secondary bTBI from shrapnel penetration, tertiary bTBI from head contact and acceleration forces when the body is moved by “blast wind” or a forced super-heated airflow, and quaternary includes any remaining factors not included by the early phases such as extracranial injuries.[57] The mechanical complexity of bTBI makes it very difficult to replicate it in its entirety. While it is rare to experience only the primary blast phase of this injury, inclusion of the representative, first three phases, makes experiments more difficult to reproduce and to repeat. Blast impacts are usually quantified using peak overpressure created by the pressure wave, as well as its duration. [57]

Among several in vitro TBI models, apparatuses have been developed to apply blast-like impacts to cell cultures. One model developed by Panzer and colleagues utilizes a shock tube capable of generating a peak pressure of up to 650 kPa with a positivity duty-cycle between 0.3 and 3 msec. [57] A chamber located at one end of the shock tube separated by a PET membrane is gradually filled with pressurized gas until the membrane ruptures, which leads to the propagation of a shock wave through the shock tube. Another design proposed by Ravin and colleagues makes use of an air gun to generate a wave of pressurized gas, which is then directed onto a cell culture well. [57] In a recent review[57] of in vitro TBI models, only three studies[58-61] were found that implemented a blast model. Vogel and colleagues investigated phosphodiesterase -4 inhibition by roflumilast as a therapeutic strategy for reducing long-term potentiation deficits in blast exposed rat brain cells. [57,58] Roflumilast is a phosphodiesterase inhibitor that is typically prescribed to people experiences severe chronic obstructive pulmonary disease and has been found to decrease swelling in lungs by targeting inflammation. In these investigations, a therapeutic window was found of least 6 hours, but less than 23 h with a minimal therapeutic concentration of 1nM of roflumilast. [57] Arun and colleagues examined the effects of blast injury on hybrid mouse neuroblastoma and rat glioblastoma cells, and human SH-SY5Y neuroblastoma cells. [57,59] Post-blast injury, metabolic impairment was reflected by reduced levels of ATP and while upregulation of lactate dehydrogenase (LDH) suggested compromised plasma membrane. [57,59] The upregulation of reactive oxygen species (ROS) was also found post-blast injury that indicated increased oxidative stress or reduced antioxidant protection. [57,59] Studies by Ravin and colleagues using dissociated cultures derived from rat and embryonic CNS cortex tissue and the air gun model, indicated significantly increased levels of calcium activity and expressions of a reactive astrocyte marker, GFAP, and a protease, matrix metallopeptidase 9 (MMP-9) 24 hours after blast stimulation. [57,59] Interestingly, they found human astrocytes more responsive to injury than rat-derived astrocytes. Vogel and colleagues applied a shockwave with a peak pressure of 336 kPa, which was closest to the estimate lethal range of 414-552 kPa or 60-80 psi. [57,61] Interestingly, Arun and colleagues applied only 145 kPa or 21 psi, which is about a quarter of the lethal range.[57] Additional studies found that measures of neuronal function were significantly altered at exposures of 336 kPa with positive duty-cycles of 0.84 ms or 86.5 kPa*ms.[62] Thus, functional changes occur below the threshold for cell death. Interestingly, a study by Ravin and colleagues indicated that neurons under pressure without concomitant shear forces, peaking between 0.3 to 0.7 at the cell surface, could tolerate overpressures as high as 220 psi.[63] While these discrepancies result from differences in study aims and apparatus design, more consistent approaches would allow for more accurate characterization of cellular behaviors. Because of the current, untreatable condition of TBI, there is great motivation for high-throughput methods in order to assess the effectiveness of potential therapeutic candidates. The ideal in vitro model captures transient changes and allows for subsequent access to later timepoints to capture long-term functional changes. In addition, future models should account for the structural complexities of the brain since, current in vitro models do not.

### 1.5.1. Laser-Induced Shockwaves

Laser-induced shockwaves (LISs) are shockwave fronts resulting from the explosive growth of a bubble induced by energy deposition at focal spots of lasers with sub-microsecond pulse-widths. LISs can induce sudden changes in intracellular levels of calcium.[64] Transient receptor potential channels in the plasma membrane can regulate calcium entry and, it is thought that the protein is activated either in response to shear stress directly or via G-protein coupled receptor. Previous studies have demonstrated that shear stress will lead to an increase in intracellular calcium, consisting of both $[Ca^{2+}]_I$ from influx and endoplasmic reticulum release.[65] Interestingly, disruptions in intracellular calcium store-mediated signaling and altered calcium-signaling in population dynamics are observed in wild-type neurons following traumatic brain injury.[66,67]

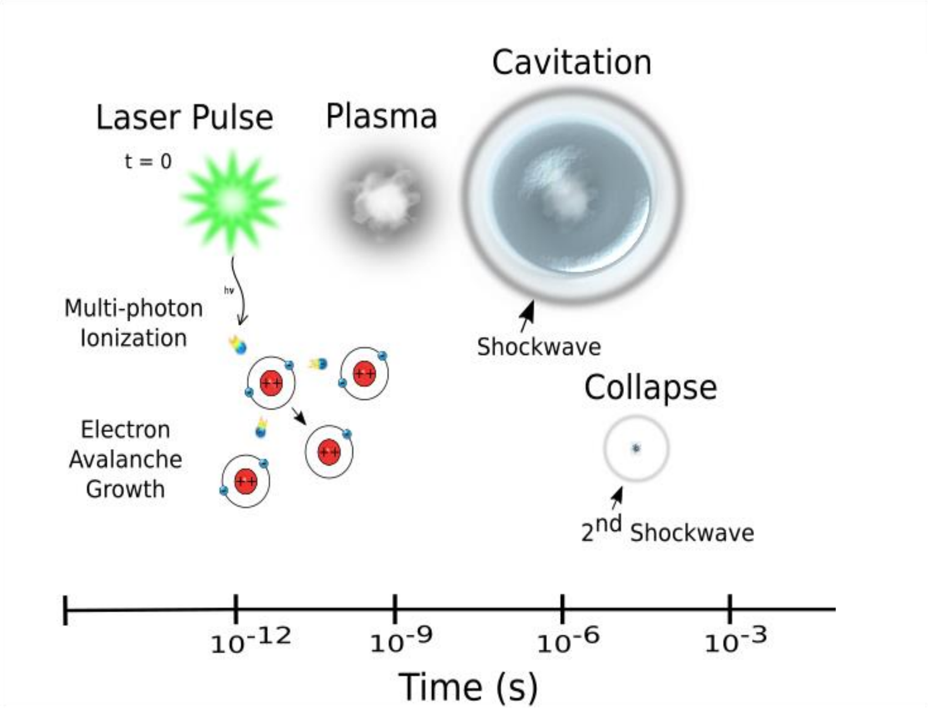

Figure 1.4 - Sequence of events following high-energy laser pulse and subsequently generated laser-induced shockwave with order of magnitude time scale.

Key events leading to the generation of a shockwave front following a laser pulse is detailed in **Figure 1.4**. Conditions leading to multi-photon ionization and subsequent electron avalanche growth are stochastic in nature, however, at energy levels exceeding a threshold for a given system the probability of forming plasma asymptotically, approaches one-hundred percent. From **Figure 1.4**, it is evident that while the full period of bubble growth and collapse may approach tens of microseconds, critical events early in bubble dynamics occur at sub-nanosecond timescales. The distinct advantage of shear force generation using LISs is the consistency and precision that the optical tool provides. Shear forces generated by a resultant shockwave front varies with regards to the bubble dynamics preceding it and the power of the pump laser being used. Consequentially, one can vary the magnitudes of shear stresses generated by LISs by varying either pump laser power levels and N.A. of the objective. Additionally, the epicenter of the LIS or the focal point at which pump energy is deposited can be moved relative to regions of interest.

## CHAPTER REFERENCES

1. E. Carafoli and J. Krebs, “Why calcium? How calcium became the best communicator,” *J. Biol. Chem.*, vol. 291, no. 40, pp. 20849–20857, 2016.

2. X. Cai, X. Wang, S. Patel, and D.E. Clapham, “Insights into the early evolution of animal calcium signaling machinery: a unicellular point of view.” *Cell Calcium, vol.* 57, pp. 166–173, 2015.

3. H. Plattner and A. Verkhratsky, “The ancient roots of calcium signaling evolutionary tree,” *Cell Calcium, vol.* 57, pp. 123–132, 2015.

4. M. Brini, T. Calì, D. Ottolini, and E. Carafoli, “Intracellular calcium homeostasis and signaling,” *Metallomics and the Cell*, *Metal Ions in Life Sciences,* vol. 12, pp. 119–168, 2013.

5. A. C. Newton, M. D. Bootman, and J. Scott, “Second messengers,” *Cold Spring Harb. Perspect. Biol.*, vol. 8, no. 8, 2016.

6. M. Brini, T. Calì, D. Ottolini, and E. Carafoli, “Neuronal calcium signaling: Function and dysfunction,” *Cell. Mol. Life Sci.*, vol. 71, no. 15, pp. 2787–2814, 2014.

7. P. James, M. Maeda, R. Fischer, A.K. Verma, J. Krebs, J.T. Penniston, E. Carafoli, “Identification and primary structure of a calmodulin binding domain of the Ca2+ pump of human erythrocytes,” *J. Biol. Chem.*, vol. 263, no. 6, pp. 2905–2910, 1988.

8. G. E. Hardingham and H. Bading, “Synaptic versus extrasynaptic NMDA receptor signalling: Implications for neurodegenerative disorders,” *Nat. Rev. Neurosci.*, vol. 11, no. 10, pp. 682–696, 2010.

9. O. Isacson, “On neuronal health,” *Trends Neurosci*., vol. 16, pp. 306–308. 1998.

10. S. Papadia, P. Stevenson, N.R. Hardingham, H. Bading, G.E. Hardingham, “Nuclear Ca2+ and the cAMP response element-binding protein family mediate a late phase of activity-dependent neuroprotection,” *J. Neurosci.*, vol. 25, pp. 4279–4287, 2005.

11. A. Bonni, A. Brunet, A. E. West, S. R. Datta, M.A. Takasu, and M.E. Greenberg, "Cell survival promoted by the Ras-MAPK signaling pathway by transcription dependent and -independent mechanisms," *Science*, vol. 286: pp. 1358–1362, 1999.

12. B. Mayr and M. Montminy, "Transcriptional regulation by the phosphorylation-dependent factor CREB," *Nat. Rev. Mol. Cell Biol.,* vol. 2, pp. 599–609, 2001.

13. B.E. Lonze, A. Riccio, S. Cohen, and D.D. Ginty, "Apoptosis, axonal growth defects, and degeneration of peripheral neurons in mice lacking CREB," *Neuron*, vol. 34, pp. 371–385, 2002.

14. T. Mantamadiotis, T. Lemberger, S.C. Bleckmann, H. Kern, O. Kretz, A.M. Villalba, F. Tronche, C. Kellendonk, D. Gau, J. Kapfhammer, C. Otto, W. Schmid, and G. Schütz, "Disruption of CREB function in brain leads to neurodegeneration," *Nature Genetics*, vol. 31, pp. 47–54, 2002.

15. W.A. Carlezon Jr., R.S. Duman, E.J. Nestler, "The many faces of CREB," *Trends Neurosci.*, vol. 28, pp. 436–445, 2005.

16. H. Thoenen, Y.A. Barde, A.M. Davies, and J.E. Johnson. "Neurotrophic factors and neuronal death," *Ciba Found Symp.*, vol. 126, pp. 82–95, 1987.

17. H.H. Hansen, T. Briem, M. Dzietko, M. Sifringer, A. Voss, W. Rzeski, B. Zdzisinka, F. Thor, R. Heumann, A. Stepulak, P. Bittigau, C. Ikonomidou, "Mechanisms leading to disseminated apoptosis following NMDA receptor blockade in the developing rat brain," *Neurobiol Dis.*, vol. 16, pp. 440–453, 2004.

18. J.W. Putney Jr., "A model for receptor-regulated calcium entry," *Cell Calcium*, vol. 7, no. 1, pp. 1–12, 1986.

19. D. Chin and A.R. Means, "Calmodulin: a prototypical calcium sensor," *Trends Cell Biol*., vol. 10, no. 8, pp. 322–328, 2000.

20. M.P. Mattson, "Calcium and neurodegeneration." *Aging Cell*, vol. 6, pp. 337-350, 2007.

21. G. Gibson, C. Cotman, G. Lynch, and J. Blass, "Calcium Hypothesis of Alzheimer's disease and brain aging: A framework for integrating new evidence into a comprehensive theory of pathogenesis," *Alzheimer's Dement.*, vol. 13, no. 2, pp. 178-182.e17, 2017.

22. E. Roze, C. Bonnet, S. Betuing, and J. Caboche, "Huntington's Disease," *Disease of DNA Repair*. pp.45-52, 2010.

23. L.A. Raymond, "Striatal synaptic dysfunction and altered calcium regulation in Huntington disease," *Biochemical and Biophysical Research Communications*, 2016.

24. M. Giacomello, R. Hudec, and R. Lopreiato, “Neuronal Ca2+ dyshomeostasis in Huntington disease,” *Prion*, vol. 7, no. 1, pp.76-84, 2013.

25. M. Suzuki et al., “Biochemical and Biophysical Research Communications Calcium leak through ryanodine receptor is involved in neuronal death induced by mutant huntingtin,” *Biochemical and Biophysical Research Communications*, vol. 429, no.1-2, pp.18–23, 2012.

26. T.S. Tang, E. Slow, V. Lupu, I.G. Stavrovskaya, M. Sugimori, R. Lliáns, B.S. Kristal, M.R. Hayden, and L. Bezprozvanny, “Disturbed $Ca^{2+}$ signaling and apoptosis of medium spiny neurons in Huntington’s disease,” *PNAS*, vol. 102, no. 7, pp. 2602-2607, 2005.

27. S. Marco, A. Murillo, I. Pérez-Otaño, “GluN3A promotes NMDA spiking by enhancing synaptic transmission in Huntington’s disease models,” *Neurobiology of Disease*, vol. 93, pp. 47-56, 2016.

28. G.E. Hardingham and H. Bading, “Synaptic versus extrasynaptic NMDA receptor signalling: implications for neurodegenerative disorders” *Nature*, vol. 11, pp. 682-696, 2010.

29. G. Liot, D. Zala, P. Pala, G. Mottet, M. Piel, and F. Saudou, “Mutant Huntingtin Alters Retrograde Transport of TrkB Receptors in Striatal Dendrites,” *J. of Neuroscience*, vol. 33, no. 15, pp. 6298–6309, 2013.

30. P. H. Reddy and U. P. Shirendeb, “Mutant huntingtin, abnormal mitochondrial dynamics, defective axonal transport of mitochondria, and selective synaptic degeneration in Huntington’s disease,” *Biochim. Biophys. Acta - Mol. Basis Dis.*, vol. 1822, no. 2, pp. 101–110, 2012.

31. X. Zhao, X. Chen, E. Han, Y. Hu, P. Paik, Z. Ding, J. Overman, A.L. Lau, S.H. Shahmoradian, W. Chiu, L.M. Thompson, C. Wu, and W.C. Mobley, “TriC subunits enhance BDNF axonal transport and rescue striatal atrophy in Huntington’s disease,” *Proc. Natl. Acad. Sci.*, vol. 113, no. 38, pp. E5655–E5664, 2016.

32. N. B. Chauhan, “Chronic neurodegenerative consequences of traumatic brain injury,” *Restor. Neurol. Neurosci.*, vol. 32, no. 2, pp. 337–365, 2014.

33. M. Tymianski, and C. H. Tator, “Normal and Abnormal Calcium Homeostasis in Neurons: A Basis for Pathophysiology of Traumatic and Ischemic Central Nervous System Injury,” *Neurosurgery*, vol. 38, no. 6, pp. 1176-1195, June 1996.

34. C. Grienberger and A. Konnerth, “Imaging Calcium in Neurons,” *Neuron*, vol. 73, no. 5, pp. 862–885, 2012.

35. R.Y. Tsien, “New calcium indicators and buffers with high selectivity against magnesium and protons: design, synthesis, and properties of prototype structures,” *Biochemistry*, vol. 19, pp. 2396–2404, 1980.

36. D. Thomas, S. C. Tovey, T. J. Collins, M. D. Bootman, M. J. Berridge, and P. Lipp, “A comparison of fluorescent Ca2+ indicator properties and their use in measuring elementary and global Ca2+ signals,” *Cell Calcium*, vol. 28, no. 4, pp. 213–223, 2000.

37. K. R. Gee, K. A. Brown, W. U. Chen, D. Gray, and I. Johnson, “Chemical and physiological characterization of fluo-4 Ca 2 + - indicator dyes,” vol. 27, pp. 97–106, 2000.

38. M. Gleichmann and M.P. Mattson, “Neuronal calcium homeostasis and dysregulation,” *Antioxidants & redox signaling*, vol. *14*, no. 7, pp. 1261–1273, 2011.

39. Takahashi, P. Camacho, J. D. Lechleiter, and B. Herman, “Measurement of intracellular calcium,” *Physiol. Rev.*, vol. 79, no. 4, pp. 1089–1125, 1999.

40. M.W. Berns, “A History of Laser Scissors (Microbeams),” *Methods in Cell Biology,* vol. 82, pp. 3-58, 2007.

41. A. Vogel, J. Noack, G. Huttman, G. Paltauf, “Mechanisms of femtosecond laser nanosurgery of cells and tissues,” *Applied Physics B - Lasers and Optics*, vol. 81, pp. 1015-1047, 2005.

42. Bessis M, Gires F, Mayer G, Nomarski G: Irradiation des organites cellulaires a l'aide d'un laser a rubis. C.R. Acad.Sci 225:1010-1012, 1962.

43. R. Amy and R. Storb, “Selective mitochondrial damage by a ruby laser microbeam: An electron microsocpic study,” *Science*, vol. 150, pp. 756-757, 1965.

44. R. Storb, R. Amy, R.K. Wertz, and M. Bessis, “An electron microscope study of vitally stained single cells irradiated with a ruby laser microbeam,” *Journal of Cell Biology*, vol. 31, pp. 11-29, 1966.

45. M.W. Berns, “Partial cell irradiation with a tunable organic-dye laser,” *Nature*, vol. 240, pp. 483-485, 1972.

46. M.W. Berns, R. Olson, and D. Rounds, “Argon laser micro-irradiation of nucleoli,” *Journal of Cell Biology*, vol. 43, no. 3, pp. 621-626, 1969.

47. M.W. Berns, R. Olson, D. Rounds, “In vitro production of chromosomal lesions with an argon laser microbeam,” *Nature*, vol. 221, pp. 74-75, 1969.

48. M.W. Berns, “A possible two-photon effect in vitro using a focused laser beam,” *Biophysical Journal*, vol. 16, pp. 973-977, 1976.

49. M.W. Berns, J. Aist, J. Edwards, K. Strahs, J. Girton, P. McNeill, et al., “Laser microsurgery in cell and developmental biology,” *Science*, vol. 213, pp. 505-513, 1981.

50. P. Calmettes and M. Berns, “Laser-induced multiphoton processes in living cells,” *PNAS -Biological Sciences,* vol. 80, pp. 7197-7199, 1983.

51. A. Vogel, J. Noack, G. Huttman, and G. Paltauf, “Mechanisms of femtosecond laser nanosurgery of cells and tissues,” *Applied Physics B - Lasers and Optics*, vol. 81, pp. 1015-1047, 2005.

52. M.P. Felix and A.T. Ellis, ”Laser-induced liquid breakdown – a step-by-step account,” *Appl.Phys. Lett.*, vol. 19, pp. 484–486, 1971.

53. W. Lauterborn and A. Vogel, *Bubble dynamics and shock waves*. 2013.

54. A. Vogel and W. Lauterborn, “Acoustic transient generation by laser-produced cavitation bubbles near solid boundaries,” *The Journal of the Acoustical Society of America*, vol. 84, no. 2. pp. 719--731, 1988.

55. K. R. Rau, A Guerra III, A. Vogel, and V. Venugopalan, “Investigation of laser-induced cell lysis using time-resolved imaging Investigation of laser-induced cell lysis using time-resolved imaging,” vol. 2940, pp. 10–13, 2004.

56. A. N. Hellman, “Biophysical response to pulsed laser microbeam-induced cell lysis and molecular delivery,” vol. 35, no. 1, pp. 24–35, 2008.

57. Y. H. Wu, S. Rosset, T. R. Lee, M. Dragunow, T. Park, and V. Shim, “In Vitro Models of Traumatic Brain Injury: A Systematic Review,” *J. Neurotrauma*, vol. 38, no. 17, pp. 2336–2372, 2021.

58. E.W. Vogel 3rd, F.N. Morales, D.F. Meaney, C.R. Bass, and B. Morrison 3rd, “Phosphodiesterase-4 inhibition restored hippocampal long term potentiation after primary blast,” *Exp. Neurol.*, vol. 293, pp. 91–100, 2017.

59. P. Arun, J. Spadaro, J. John, R.B. Gharavi, T.B. Bentley, and M.P. Nambiar, “Studies on blast traumatic brain injury using in-vitro model with shock tube,” *Neuroreport*, vol. 22, no. 8, pp. 379–384, 2011.

60. R. Ravin, P.S. Blank, B. Busse, N. Ravin,S. Vira, L. Bezrukov, H. Waters, H. Guerrero-Cazares, A. Quinones-Hinojosa, P.R. Lee, R.D. Fields, S.M. Bezrukov, and J. Zimmerberg, ”Blast shockwaves propagate Ca2+ activity via purinergic astrocyte networks in human central nervous system cells,” *Sci. Rep.*, vol. 6, 2016.

61. Committee on Gulf War and Health: Long-Term Effects of Blast Exposures; Board on the Health of Select Populations; Institute of Medicine. Gulf War and Health, Volume 9: Long-Term Effects of Blast Exposures. Washington (DC): National Academies Press (US); 2014 Apr 14.

62. N. E. Zander, T. Piehler, M. E. Boggs, R. Banton, and R. Benjamin, “In vitro studies of primary explosive blast loading on neurons,” *J. Neurosci. Res.*, vol. 93, no. 9, pp. 1353–1363, 2015.

63. R. Ravin, P.S. Blank, A. Steinkamp, S.M. Rappaport, N. Ravin, L. Bezrukov, H. Guerrero-Cazares, A. Quinones-Hinojosa, S.M. Bezrukov, and J. Zimmerberg, “Shear forces during blast, not abrupt changes in pressure alone, generate calcium activity in human brain cells,” *PLoS One*, vol. 7, no. 6, 2012.

64. A. Selfridge, D. Preece, V. Gomez-Godinez, L.Z. Shi, and M.W. Berns, “A model for traumatic brain injury using laser induced shock waves," *Proceedings of the SPIE*, vol. 9548, id. 95480P, pp. 11, 2015.

65. V. Gomez-Godinez, D. Preece, L. Shi, N. Khatibzadeh, D. Rosale, Y. Pan, L. Lei, Y. Wang, and M.W. Berns, “Laser-induced shockwave paired with FRET: A method to study cell signaling," *Microscopy Research and Technique,”* vol. 78, no. 3, pp.195-199, 2015.

66. J.T. Weber, B.A. Rzigalinski, and E.F. Ellis, “Calcium responses to caffeine and muscarinic receptor agonists are altered in traumatically injured neurons,” *Journal of Neurotrauma*, vol. *19*, no. 11, pp.1433–1443, 2002.

67. V. Gomez-Godinez, V. Morar, C. Carmona, Y. Gu, K. Sung, L.Z. Shit, C. Wu, D. Preece, and M.W. Berns, “Laser-induced Shockwave (LIS) to Study Neuronal Ca2+ Response,” Front. Bioeng. Biotechnol., February 2021.

# Chapter 2: Neurons

## 2.1. Huntington's Disease

### 2.1.1. Overview

Huntington's disease (HD) is a dominantly inherited neurodegenerative disorder that currently has no disease-modifying treatment. While the prevalence of HD is about 4-8 per 100,000 population, it can reach up to 700 in some parts of the world.[1] Age onset of HD is between 35 and 50 years but can range from 2 to 85 years. [1] Life expectancy after HD onset is about 15-20 years and possibly shorter for juvenile HD, in which onset occurs before 30 years of age and accounts for about 15% of all cases.[1]

In this chapter, I briefly discuss the BACHD[2] mouse, a Huntington's disease model mouse used throughout these studies. Attention will be given to the overall process of producing primary, mammalian neuronal cultures for imaging using real-time, fluorescence microscopy techniques. Lastly, methods utilized for ensuring consistently viable neuronal cultures and practical considerations are studied and discussed including a detailed study on evaporation and its mitigation.

## 2.2. BACHD Rodent Model

### 2.2.1. Related Studies on Phenotype

Models of HD are designed to recreate many HD-relevant phenotypes. The BACHD[2] mouse, which uses bacterial artificial chromosome (BAC) technology to express full length mHTT (97 CAG repeats), shows progressive deficits in motor, cognitive, and behavioral function; there is atrophy of striatum and cortex. [2,3] mHTT is found in cytosol in somas and processes; aggregates are found in cortex and striatum.[4] Decreased synaptic function, which was progressive, was evident in medium spiny neurons (MSNs), primarily found in the striatum. Cortico-striatal synapses were decreased. Deficits in motor function and behavior were also progressive. Pathologically, degenerating MSNs were seen at 12 months.[2] All phenotypes were prevented when mHTT was deleted in both cortex and striatum.[3] Interestingly, MSNs from 6-month-old BACHD mice relative cumulative amplitude distributions revealed that small-amplitude events had higher probability in cells from BACHD compared with cells from WT mice. BACHD and wild type mice will be used in all studies discussed and a colony has been established at UCSD.

## 2.3. Mouse Colony

### 2.3.1. Methods

The rodent colony established at UCSD was routinely maintained at least twice a week. Breeder pairs were established such that one male was paired with at least one female for three to five days and one of the breeders is wildtype mouse while the other is a BACHD transgenic mouse. After at least two days, breeder pairs are checked for vaginal plug formation as an indication of conception that aid in establishing more accurate embryonic dates. If no plugs are found after several days, females are separated and monitored for signs of pregnancy until after 21 days. Breeder pairings were set up with dissections planned among a range of a few days so that embryos were harvested between embryonic dates 16 to 18 days (E16-18).

Excess breeder pairs were established for the continuity of the mouse colony. New litters were weaned from mothers at 28 days after birth. New pups have their tails clipped and ears punched upon weaning for genotyping and future identification, respectively. With surgical scissors and a glass bead sterilizer used in between tail sample collections, tails are clipped about 1mm from the tip and collected into sterile 5mL tubes with hinged lids that are labelled with both gender and identification numbers. Immediately after weaning a litter, tail samples are dissolved within respective tubes with the addition of 300 µL of a 50 mM solution of NaOH and, with caps closed, incubated for at least 1 hour at 90ºC. This ensures the dissolution of tissue and the release of DNA into the solution. After incubation, tubes are left on ice or at room temperature for at least 5 minutes. Then, an addition of 60 µL of 0.5 M Tris-HCL at pH 8.0 is made to neutralize the sample. Finally, samples are centrifuged at 13k RPM for 2 minutes before use or storage at -20 ºC. Samples are then ready for polymerase chain reaction (PCR) thermal cycling and, subsequent, genotyping, which are described in greater detail in **Appendix B.i-ii.**

### 2.3.2. Statistics and Observations

Several data, see **Appendix A.i.a-d**, and observations were collected and made throughout management of the rodent colony. Particular attention was made to successful breeding pairs by tracking the number of pregnancies occurring from several combinations of mice at adult breeding age, which is between 1.5 to 6 months. In general, the pregnancy rate for breeding pairs was 35.86%. The rate of pregnancy appears to drop significantly for breeding pairs with male BACHD mice after 3.5 months. While the average rate of pregnancy for breeding pairs with female wild type mice appears to match the average pregnancy rate of 35.86%, the average rate of pregnancy for female, BACHD mice is 14% lower. A similar decline in pregnancy rate is also seen in males of both genotypes.

On at least three occasions, breeder pairs containing a female, BACHD and male, wildtype combination were found to have engaged in aggression. The male in this situation was commonly found with deep lacerations in the tail and scarring near genitals. Often both male and female breeding partners were found with minor scratches on their tail. Overall, these observations suggest that mice with the BACHD genotype were more likely to exhibit aggression towards partners of the opposite sex during pairing. These observations coupled with the relatively lower pregnancy rates seen in female BACHD mice suggest that the increase in aggression may result in lower pregnancy rates. However, one cannot necessarily exclude any effects that the HD gene may have on reproductivity. Interestingly, increased aggression is a common symptom experienced by Huntington’s disease patients.[5]

## 2.4. Dissection

Practices and policies for animal care and use are adopted from the UCSD Institutional Animal Care and Use Committee (IACUC). The objective for the dissection of mice is the harvest of embryonic brain tissue in order to plate primary neuronal cortical cultures. This process can be divided into three steps, the first step being removal of embryos from the adult mouse then, the second being removal of whole brain tissue from embryos. The third and last step consists of sectioning whole brain tissue to remove the desired brain region for culture plating and future experimentation.

Firstly, the pregnant, adult mouse is placed in a closed container (unused, pipette tip box) with about 2-3mL of isoflurane distributed on shredded paper towels in a salt shaker. The mouse is set aside and held in the container for several minutes until movement is no longer observable. Cervical dislocation is performed to euthanize the pregnant mouse and immediately afterwards the abdomen is sterilized with alcohol. With surgical scissors and stainless steel tweezers, one removes the skin and cuts through remaining dermis to expose the area just beneath the intestines containing several embryos in utero. Fully intact embryos are harvested and placed on ice in a sterile, glass dish. The rest of the dissection takes place in a sterile, biosafety cabinet.

Intact embryos are individually exposed from surrounding tissue using tweezers and placed into individual wells of a plastic 12 well tissue culture dish containing Hank’s Buffer Saline Solution (HBSS). Whole brains and tail samples are harvested from each embryo using surgical tools and placed into, respective, 5 mL test tubes on ice. The whole brain sample is rinsed in 70% ethanol and HBSS before being placed into a 5 mL test tube containing Hibernate E, Low Fluorescence (Hib-E) (HELF, Brainbits LLC, Springfield, IL, USA). Whole brains can be immediately sectioned or stored for several hours under these conditions and have even been successfully shipped overnight without significant compromise to viability.

Dissection of each embryonic brain was performed by hand using surgical tools and a dissection microscope. The whole brain was sectioned in order to harvest cortical regions of the brain. These cortical regions were removed from the whole brain sample and placed into separate test tubes containing Hib-E or grouped by genotype if known.

Suspended samples of cortical brain tissue is ready for further processing in order to isolate and to plate primary cortical neurons.

## 2.5. Cell Plating

### 2.5.1. Plating Density

In these studies, the plating density refers to the number of cells per area on a glass coverslip. The plating density was determined by two factors. Firstly, past studies on synapse formation in relation to neuron density show over a two-fold increase in synapse/neuron for neuron densities of <500 neurons/mm$^2$ in comparison to cultures with 500 – 4500 neurons/ mm$^2$.[6] Secondly, to sample high amounts of emissions activity data there is an incentive to saturate the field of view (FOV) with neurons, however, doing so may make it harder to identify individual cell bodies. Therefore, as a compromise between saturating the FOV and increasing relative synapse formation within a culture the plating density of 500 neurons/mm$^2$ is used throughout these studies. Great attention and detail is given to the cleanliness of glass substrates used for plating in order to ensure homogenous distribution of neurons during culture seeding. Sonication of glass substrates is performed in a similarly manner as described by the Salmon Lab.[7] After thorough cleaning, dry glass substrates are coated with poly-D-lysine dissolved in borax buffer solution. The protocol for glass substrate preparation is described in further detail in **Appendix B.iii**. Prior to thorough cleaning of glass coverslips a separate protocol was employed which soaked coverslips in 30% HCl acid overnight under a rotating stage with gentle rotations. The acid soak was followed by several rinses of double distilled-H20. Then, coverslips were rinsed with 70% ethanol and flame sterilized,

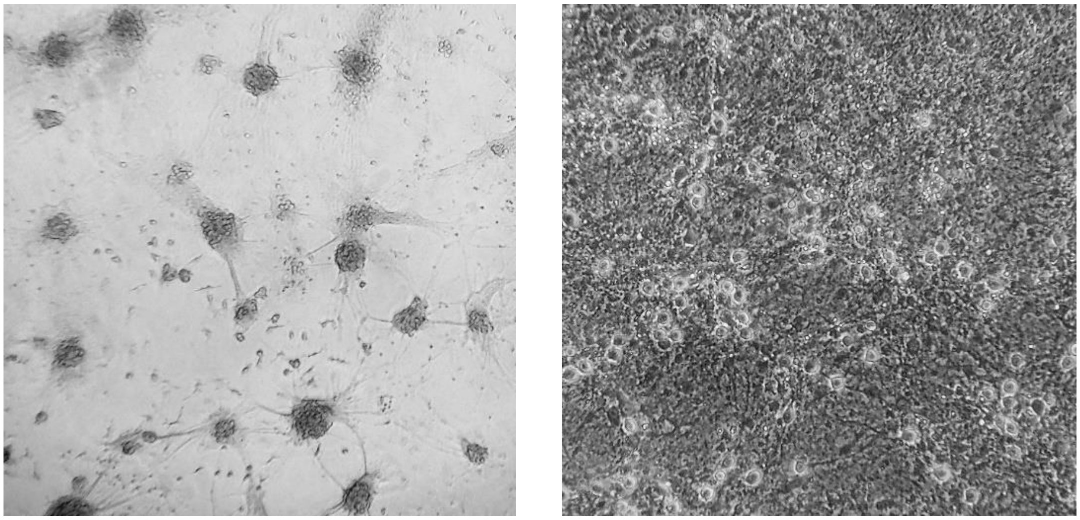

Figure 2.1 – Wild type cortical neurons at 21 days in vitro imaged using 4x/0.13 objective. Seeded on flame sterilized coverslips cleaned with (left) without ultrasonication and seeded on identical coverslips cleaned (right) with ultrasonication protocol.

however, this protocol is compared with the cleaning protocol used throughout this study. While cultures from the same tissue were plated at the same cell densities, the distribution of neurons varied depending on the cleaning protocol used as shown in **Figure 2.1**.

### 2.5.2. Viability

Producing consistently, viable primary cortical cultures was crucial for the interpretation of experimental results. Therefore, cell culture viability was measured upon seeding of primary cultures using trypsin blue and later gauged during experimentation with the use of fluorescent dyes. While plating of primary neuronal cultures will be discussed see **Appendix B.iv** for a more detailed description. During the culture seeding process, whole brain tissue is broken down both enzymatically with trypsin and mechanically by use of a suction bulb and fire-blown tip, glass pipette. Both techniques are utilized in order to breakdown brain tissue and underlying extracellular matrix, which otherwise prevents the release of individual cells into homogenous suspension.

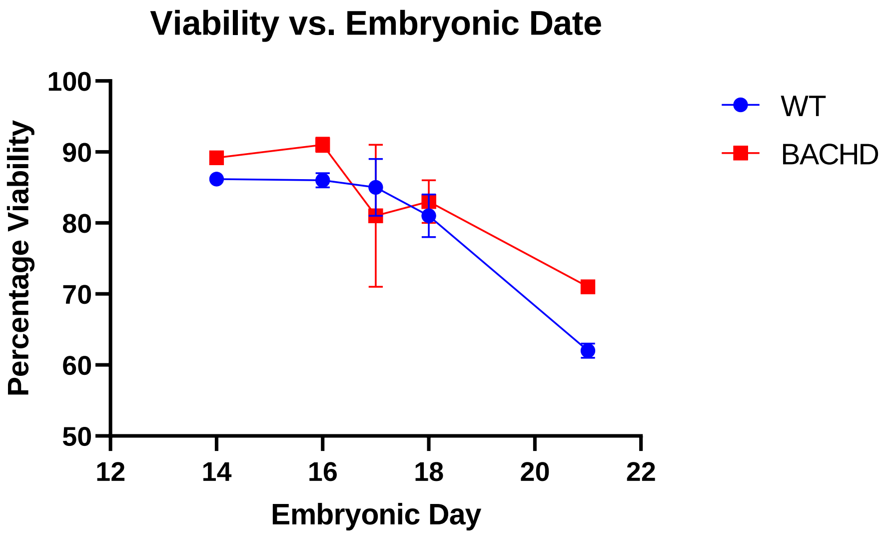

Figure 2.2 – Average percentage viability of cortical, primary dissociated neuronal culture suspension prior to culture seeding. Values are averages of percentages measured on various experimental dates. Errorbars indicate standard error of the mean.

Prior to seeding primary cortical neuron cultures, the effectiveness of homogenization and culture viability is measured using 0.4% trypan blue solution (15250061, ThermoFisher Scientific) staining. An aliquot of some known dilution of cell suspension stock is further diluted with trypan blue at twice the expected working concentration. This aliquot is then incubated in hand for at least 1 minute before being dispersed in 10 µL onto a hemacytometer while minding its glass coverslip. Trypan blue is a large molecule dye that is not known to enter a cell unless it is necrotic since, necrotic cells have compromised membrane integrity. Both total number of individual cells and dye-stained cells were visually counted under a microscope within the counting area of the hemacytometer. Counted sums of cells for each quadrant were averaged to obtain a values used to dilute and to seed cultures at a desired density. This process was performed for each genotype of prepared, cell suspension. Values of viability observed by cell counting are shown in **Figure 2.2** and an observed decline is apparent by embryonic date 21 or rather post-natal date zero, just after birth. Interestingly, viability appears to be higher for BACHD cortical neurons at E14 and E16. While the population size for E14 includes a single experimental date, both E16 and E18 contain comparable population sizes with the latter values of average percentage variability varying much less between genotypes. Nevertheless, the percentage viability for targeted embryonic dates E16-18, does not vary significantly between genotypes as shown in box plots of values in **Figure 2.3**. Viable cell plating densities used to seed cultures were calculated from total yields using average percentage viability values calculated on date of plating. Yields for average, normalized cell densities are shown in **Figure 2.4**. Average cell suspension yields for genotypes and both cortical and striatal brain regions are given in **Figure 2.4**.

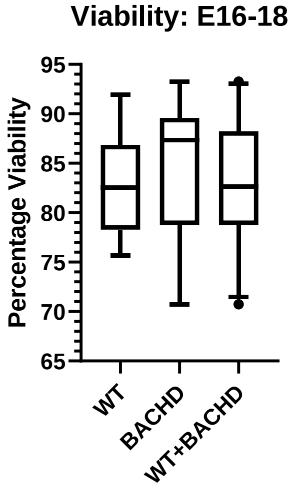

Figure 2.3 – Box plots indicating median at central band, interquartile range bounded by box, and errorbars indicating data bounded by the 5th and 95th percentiles. Percentage viability values are for cultures within embryonic dates 16 – 18 (E16-18).

While previous studies[2] link BACHD mice with smaller striatum relative to wildtype, differences are not observed. These difference are likely not observed because the reduced size of striatum probably results from chronic deficits seen later in the lifetime of a BACHD mouse. Moreover, current protocols allow for too much variance relative to that needed to resolve any meaningful differences in mass from cell density yields.

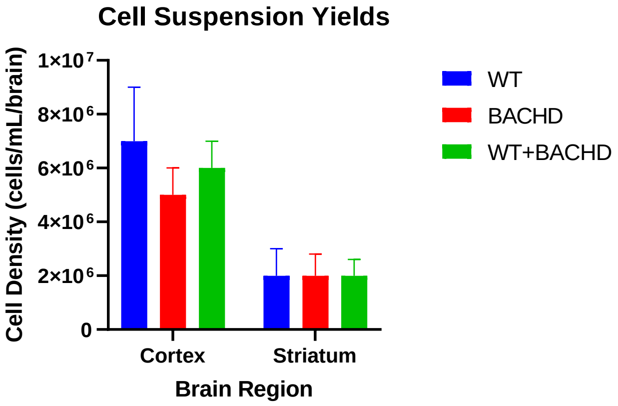

Figure 2.4 – Total yields of cell suspension given in normalized cell density. Values are found for individual genotypes and different brain regions.

Future improvements in precision may result from measuring brain tissue mass by region prior to the preparation of culture seeding as opposed to assigning nominal unit values for normalization of cell density measurements. Regarding the error introduced from weighing, if one were to approximate the density of brain tissue to that of water (1 mg/mm$^3$ or 1 g/mL) then, a spherical approximation of the average embryonic mouse brain having a radius of 5 mm would have a volume of roughly 500 mm$^3$. Given the sensitivity of bench top scales of about 0.1 mg and the expected weight of 0.5 mg per brain, it would take at least 2 brains per weighing to achieve a precision of 10%, which assumes the total brain mass is weighed and not a percentage accounting for different brain regions. In our case, we can assume

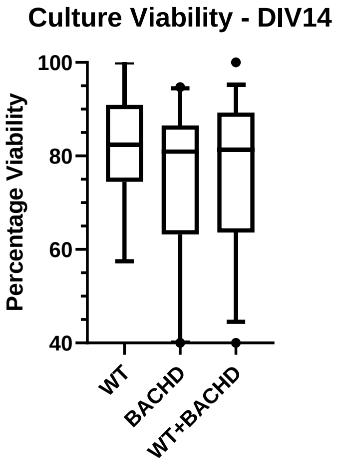

Figure 2.5 - Box plots with median at central band, interquartile ranges bounded by box, and error bars indicating data bounded by the 5th and 95th percentiles. The outliers are shown as individual points. Percentage viability is measured by normalizing number of cells with colocalizing stains of Hoechst and Fluo 4 by the total number of cells with only Hoechst stains.

from an average of ten pups a litter and 25% chance of obtaining a BACHD embryo that leaves an approximate precision of 7% for 1.5 mg accounting for the mass of three BACHD embryonic brains. The striatum of a mouse brain comprises approximately 5-6% of brain volume[8] while in comparison the cortical volume comprises approximately 42% of brain volume.[9] Therefore, the expected percentage of mass for striatum relative to 1.5 mg of total brain mass is at most 0.09 mg or 90 µg, which suggests that the in order to attain at least 10% precision needed on a scale to obtain a result is at least 9 µg. Current values for cell suspension yields in **Figure 2.4** suggest a cell density ratio of 3:1 for cortical cells and striatal cells. As compared to a volume ratio of 7:1 for cortical and striatal volumes, this suggests that there are large unaccounted for volumes of cortical mass during tissue harvest and there may be contributions from the inherent differences in cell density of each intact brain region accounting for different densities at the time of suspension. In any case, these unexpected ratio values suggest that normalization by whole brain units is a major source of error. Current values for normalized cell density have uncertainties averaging 28% and 57% for cortex and striatum derived cell suspensions, respectively. Thus, reducing the experimental error by measuring the mass of brain tissue has the potential to reduce the current uncertainty by nearly six-fold. However, it remains unclear whether one might discover differences this early during embryonic brain development and whether the suggested improvements in accuracy can resolve those potential differences.

Viability during fluorescent microscopy experiments was assessed using the emissions data of a few fluorescent dyes. Prior to imaging, cell cultures are incubated with two membrane permeable dyes Hoechst 33258 (40044, Biotium, Fremont, CA) and Fluo 4-AM (50018, Biotium, Fremont, CA) as described in a protocol in **Appendix B.v**. Hoechst is a supravital, nuclear stain that fluoresces once bound to the nucleus of a individual cells while Fluo4-AM requires cleavage of a conjugated ester group once in the cell. Fluo4-AM is also calcium-sensitive and necrotic cells with permeabilized membranes share a concentrations of ions similar to the extracellular media. Therefore, viable cells are defined as cells with Fluo4 emissions activity overlapping respective Hoechst stain nuclei and the total number of cells is the total number of stained nuclei. Percentage viability is determined by finding the ratio of viable to total cells within a field of view. A box plot of measurements of viability for cultures at in vitro day 14 (DIV14) are shown in **Figure 2.5**. At least two fields of view per microwell in a 12 well culture plate were imaged with 6 wells **or** half of the plate dedicated each genotype or wildtype and BACHD cortical neuron samples. The median viability of cell cultures at DIV 14 measured in **Figure 2.5** are comparable to values seen in **Figure 2.3**, with the exception of a greater population distribution in values for BACHD cultures. The greater variability seen in **Figure 2.5** may result from chronic neurodegeneration in vitro and greater susceptibility to stress in culture conditions.

## 2.6. Culture Maintenance

### 2.6.1. Practical Considerations

The focus of investigations on these cortical neuronal cultures is to observe intracellular calcium activity via the emissions activity of the calcium sensitive fluorescent dye, Fluo 4. Calcium activity is ubiquitous across the cell and sensitive to the physiological states of cells. Maintaining long-term healthy neuronal cultures prior to experimentation allows for the manifestation of phenotypes hallmark of chronic neurodegeneration. Thus, several considerations on factors for long-term neuronal culture maintenance are considered here.

### 2.6.2. Methods

Firstly, it was observed that over time cultures maintained within an incubator experienced varying degrees of evaporation and additional volumes of media were required. Therefore, it became of interest to understand evaporation and vapor pressure within an incubator. Typical cell culture incubators have a tray of sterile water sitting on the bottom of the unit in order to maintain a humid environment of 90-99% relative humidity at 37°C. Several tissue culture well plates were tested for evaporation under incubator conditions.

Individual tissue culture plates were filled with an initial volume of maintenance media and weighed before and after the addition of media.

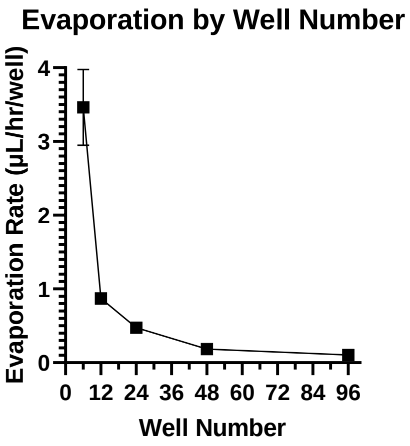

Figure 2.6 – Average evaporation rate per well for given number of microwells in plates. Shown with standard error of the mean with error bars.

Over the course of several days the tissue culture plates were weighed in the morning and evening. The average rate of evaporation is determined by calculating the average change in volume via measurements of mass. Here, the density of water is assumed to find changes in volume associated with changes in mass. Average values for evaporation using tissue culture plates with different well numbers are shown in **Figure 2.6**. It was also of interest to find whether there was variation between different regions of the tissue culture plate. Here, regions are defined by the number of adjacent wells for each well. Regions are graphically shown in **Figure 2.7** and are defined as corner region (red) for two adjacent wells, an edge region (green) with three adjacent wells, and a central region (blue) with four adjacent wells. During final weight measurements, each region was aspirated dry and, subsequent, re-weighing allowed for the determination of regional

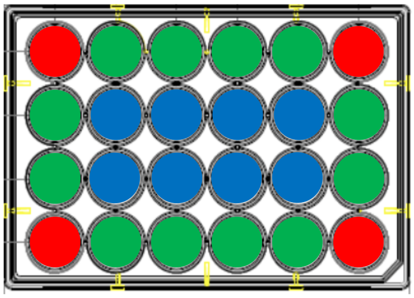

Figure 2.7 - 24 well microplate used for evaporation measurements color-coded by region: Corner (red), Edge (green), and Center (blue). Regions are defined by number of adjacent wells for each well.

contribution of weight to total weight. The difference between evaporative rates by regions for several tissue culture plates is shown in **Figure 2.8**.

Since evaporation leads to decrease in volumes of maintenance media then, it is likely that the osmolarity increases because of a decrease of volume. Osmolarity is generally defined as,

$$Osm = \sum_{i} \phi_{\mathrm{i}} n_i C_i \quad (2.1)$$

Table 2.1 - Comparison of osmolarity between commonly used cell culture media and osmotic pressure at T = 37℃ calculated from equation (1). Artificial cerebrospinal fluid (ACSF) and Dulbecco's Modified Eagle Medium (DMEM).

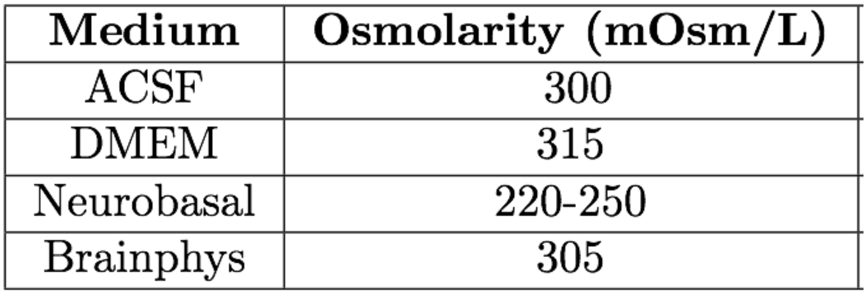

| **Medium** | **Osmolarity (mOsm/L)** |
|---|---|
| ACSF | 300 |
| DMEM | 315 |
| Neurobasal | 220-250 |
| Brainphys | 305 |

Where the osmotic coefficient describing degree of dissociation of the solute is given by $\phi_i$, the number of ions into which solute molecules dissociate is given by

$n_i$, and the molar concentration of the solute is given by $C_i$. From Equation (2.1), it is evident that $Osm\ \alpha\ V^{-1}$ where $V^{-1}$ is the volume of the solution. Decreases in volume result in non-linear increases in osmolarity, assuming there is no change in $\phi_i$ or $n_i$. Typical values of osmolarity for commercially available media are shown in **Table 2.1**. Using the relationship between volume and osmolarity as well as average evaporation rate data for a 24-well tissue culture plate, the percentage change in osmolarity (%Δ*Osm*) is shown for a 24 well plate in **Figure 2.9** under conditions of no media changes and two different fractions of 48-hour interval media replacement. In media replacements, either half or two-thirds of media is removed from the current volume that is affected by evaporation; cell culture maintenance protocols require cell culture maintenance or some media replacement every 48 to 72 hours. From

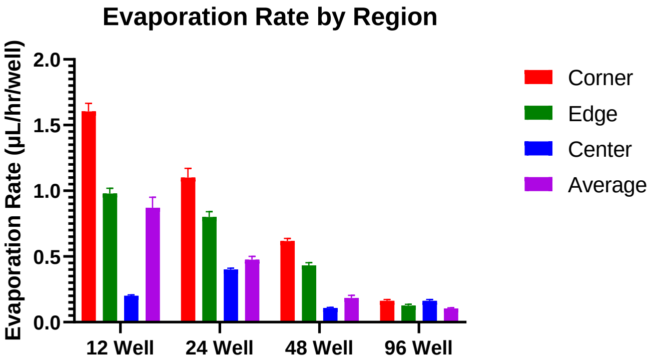

Figure 2.8 – Average evaporative rate by region for several microwell plates containing different number of wells. The standard error of the mean is including with error bars. The average evaporative rate measured for each plate is included for comparison.

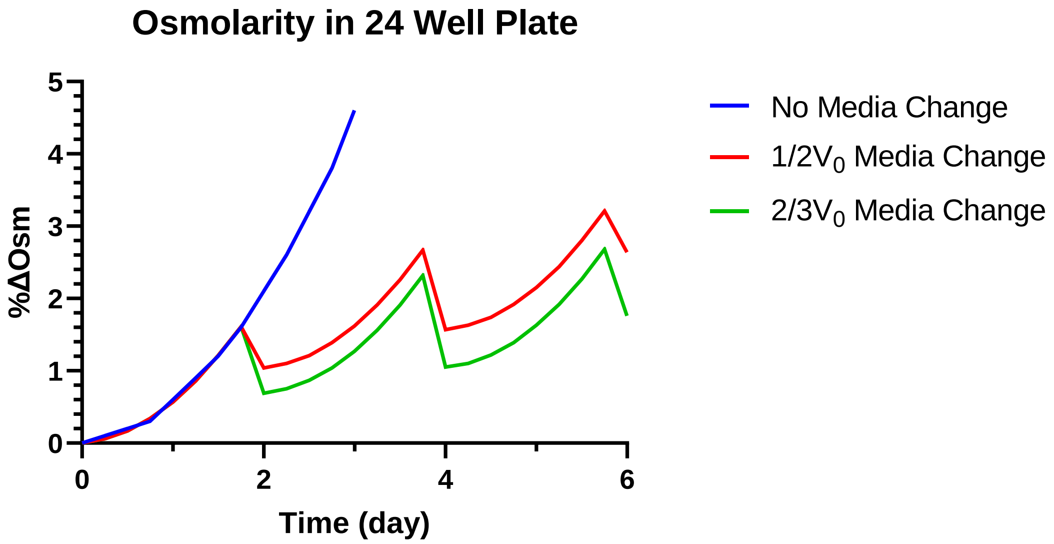

Figure 2.9 – Approximate change in osmolarity resulting from observed average evaporation in 24 microwell plate. Conditions involving media replacements using fractions of initial volume are shown.

**Figure 2.9**, within two days the osmolarity appears to increase by 2%, however, media replacement brings the change in osmolarity below 2% for at least the first two half media replacements and first three two-thirds media replacements. After ten days with recurring media replacements, the relative increase in osmolarity is 3.6% and 5.4% for half and two-thirds media replacement conditions, respectively. Synaptic formation is thought to occur at about 10 days in vitro following neuronal culture plating therefore, it is worth noting that with half media changes the osmolarity approaches values under the condition of no media replacements seen at about 3 days of incubation. While the percentage change of osmolarity here is modelled using evaporation, there may be other biological mechanisms at play that aid in lowering the overall osmolarity of a solution to promote viability of the culture.

Several cultures were plated for the purposes of investigating the observable effects of osmolarity. Long-term cultures were prepared and incubated with two separate conditions on the same 24 microwell plate. Half media replacements were performed on all the wells of the microwell plate, however, one set of 12 wells had expected evaporative volumes replaced with sterile water while the other set of 12 wells had that volume replaced by media. The goal was to attempt to maintain the osmolarity of culture media with additions of water as opposed to maintenance media. The qualitative results can be seen in **Figure 2.10**, where images are

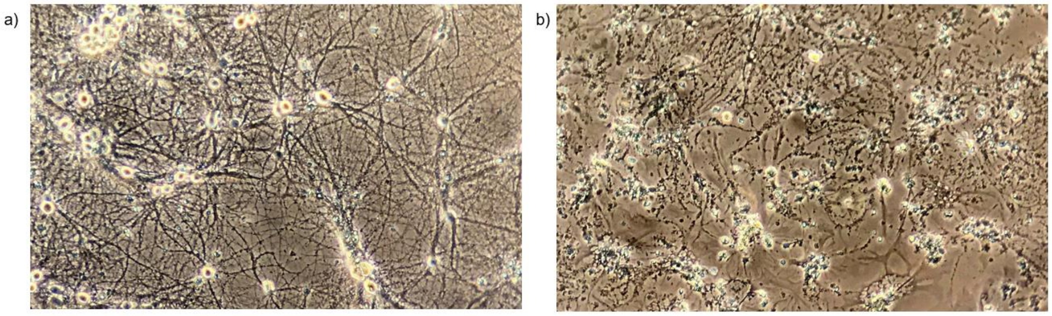

Figure 2.10 - Wildtype cortical neurons at 22 DIVs phase contrast images captured using the Olympus CK-2 microscope with a 10x objective. Both are examples of corner region wells on the same 24 well plate with ½ media replacements 48-72 hrs, however, a) had an addition of $H_2O$ equivalent to calculated evaporated volume while b) had an addition of media equivalent to calculated evaporated volume at time of replacement.

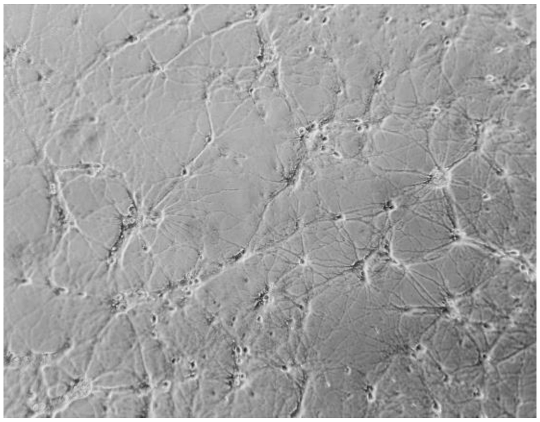

Figure 2.11 – Wild type cortical neurons at 21 DIVs imaged using 10x/0.25 objective. Culture maintained with minimal media changes.

presented of two cultures at 22 days in vitro, under similar conditions. Furthermore, a condition of minimal media changes was also tested in which a 24 microwell plate was maintained by adding empirically determined values of evaporated water every 48-72 hours. A sample FOV of the cultures maintained using minimal media changes is shown in **Figure 2.11**.

To further our understanding, a generalized model for evaporation during cell incubation is formulated and is fitted with experimental data. Consider a model for the mass of evaporated water from the surface of water without any external wind,[10]

$$m_{evap} = \Theta A(x_s - x) \quad (2.2)$$

The mass of evaporated water, $m_{evap}$, depends on the exposed surface area, $A$, the maximum humidity ratio of saturated air, $x_s$, and the humidity ratio of air, $x$. Here, $\Theta = 25$ and represents an empirically determined constant. The humidity ratio can be expressed as the partial pressure of vapor in the air to the partial pressure of the dry air. Based on the ideal gas law, the humidity ratio can be expressed as,

$$x = c_0 \frac{P_w}{(P_{atm} - P_w)} \quad (2.3)$$

Where the constant $c_0 = \frac{M_w}{M_a} = 0.60494$ is a ratio of the molecular weight of water, $M_w$, and average molecular weight of air with %5 $CO_2$, $M_a$, the composition of air assumed is shown in **Table 2.2**. The partial pressure of water vapor and the atmospheric pressure is given by $P_w$ and $P_{atm}$, respectively. In order to find the maximum humidity ratio of saturated air, **Equation (2.3)** must be solved for a partial pressure of water vapor equal to the saturation pressure of water vapor.

Table 2.2 – Composition of dry air with constituent names and percentage composition of air. The average molecular weight of air is determined by taking a weighted average of the molecular weights of each constituent. The average for this table is 29.789 g/mol.

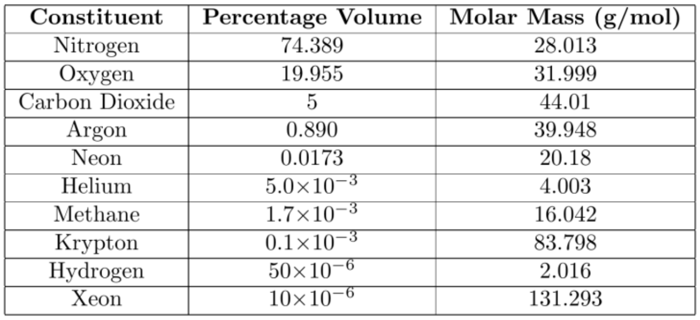

| **Constituent** | **Percentage Volume** | **Molar Mass (g/mol)** |
|---|---|---|
| Nitrogen | 74.389 | 28.013 |
| Oxygen | 19.955 | 31.999 |
| Carbon Dioxide | 5 | 44.01 |
| Argon | 0.890 | 39.948 |
| Neon | 0.0173 | 20.18 |
| Helium | $5.0\times10^{-3}$ | 4.003 |
| Methane | $1.7\times10^{-3}$ | 16.042 |
| Krypton | $0.1\times10^{-3}$ | 83.798 |
| Hydrogen | $50\times10^{-6}$ | 2.016 |
| Xeon | $10\times10^{-6}$ | 131.293 |

Generally, saturation pressure of water vapor is temperature-dependent, however, assuming a fixed incubation temperature of 37ºC the saturation pressure of water vapor is $P_{ws} = 6.258$ kPa thus, the maximum humidity ratio at 37ºC is $x_s = 0.0409$. In general, plates and dishes containing cells are covered with a lid thus, the full surface area of a well is not typically exposed to the inside of the incubator. Therefore, the effective surface area is assumed to be the plate lid area or the area found when multiplying the perimeter of the plate by the gap measured from the top of the plate to the interior of the lid. The plate lid area limits the evaporation rate amongst wells in the plate so assuming the contribution of evaporation is distributed across all wells equally then the effective area for each well is the plate lid area divided by the number of wells per plate as shown in **Table 2.3**. Since, the incubator

Table 2.3 – Effective areas exposed to inside of incubator for each microwell plate with 6- 96 wells and two circular dishes with diameters of 150 mm and 100 mm. The effective area is determined by taking the perimeter of the plate and multiplying it by the gap introduced by the lid, which was measured to be 0.63 ±0.1 mm. The microwell plates had a lid with dimensions of 127 mm X 85.1 mm. The same gap was assumed for the circular dishes however, the perimeter was calculated using their diameter.

| **Plate** | **Eff. Area ($mm^2$/Well)** |
|---|---|
| ø150 mm | 297 |
| ø100 mm | 198 |
| 6 Well | 44.6 |
| 12 Well | 22.3 |
| 24 Well | 11.2 |
| 48 Well | 5.6 |
| 96 Well | 2.8 |

is expected to fluctuate between 90-99% relative humidity the average values of evaporation between the expected range of humidity is calculated using **Equation (2.2)** and plotted with experimentally observed values in **Figure 2.12** plotted as red squares. The theoretical values for evaporative rates calculated using **Equation (2.2)** shown in **Figure 2.12** plotted as blue circles seems to agree with values of evaporation found for 6 well plates and both 150 mm and 100 mm culture dishes. The standard deviations shown in the error bars in **Figure 2.12** illustrate the degree of variation in the average theoretical evaporative rates that result from mild fluctuations in relative humidity within the incubator, however, this does not account for the observed differences between the experimental values. These results are not surprising when considering that the effective exposed areas shown in **Table 2.3**

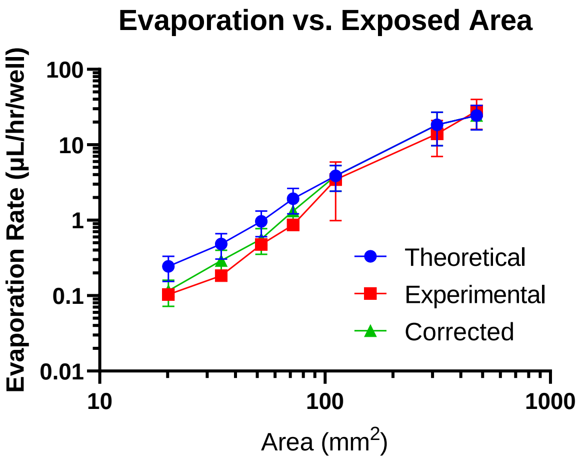

Figure 2.12 – Log-log plot of average evaporation rate plotted against exposed surface area with theoretical values (circle,blue) calculated from Equation (2.2) and experimental values (square,red). The corrected values (triangle, green) include a correction during calculation accounting for non-uniform evaporative rates across regions of tissue culture plate. The errorbars indicate the standard deviation.

used in **Equation (2.2)** were calculated by assuming each well contributes equally to the average evaporative rate. From data in **Figure 2.8**, the evaporative rate varies across different regions of microwell plates, however, 6 well plates do not have well defined regions since every well is adjacent to two others. By normalizing the evaporative rates in each region by the maximum rate observed in corner wells, these normalized ratios are sorted by region and shown in **Figure 2.13**. A new effective area is calculated from the areas, $A_n$, shown in **Table 2.2** for 12, 24, 48, and 96 well plates using a new effective number of wells and normalized ratio for each region, $N_{eff} = (N_{corner} + N_{edge}/r_{edge} + N_{center}/r_{center})$. The values $N_{corner}$, $N_{edge}$, and $N_{center}$ are the number of corner, edge, and center wells on a given plate, respectively. The ratio values $r_{edge}$ and $r_{center}$ are found experimentally and shown in **Figure 2.13.** The new effective area,

$$A'_n = A_n * \frac{N}{N_{eff}} \quad (2.4)$$

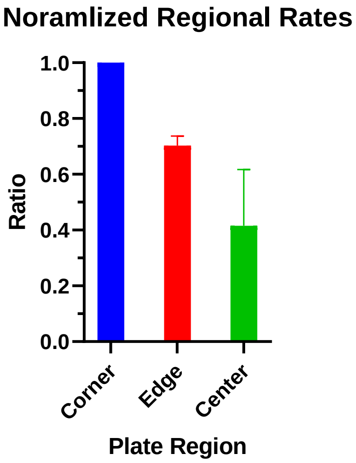

Figure 2.13 – Bar plot of ratios of average evaporation rates found for several microwell plates and normalized by the maximum evaporative rate found in the corner region. Errorbars indicate standard error of the mean.

The theoretical values of evaporative rates are re-calculated with the new effective areas for 12, 24, 48, and 96 well plates and plotted as green triangles in **Figure 2.12** using original areas shown in **Table 2.3**. In general, one would find the effective areas for 12, 24, 48, and 96 well plates by dividing the plate lid area directly by $N_{eff}$.

Further studies were performed in order to assess different methods of mitigating evaporation during incubation and whether any observable effects can be made. One laboratory has successfully utilized Polydimethylsiloxane (PDMS) molded covers for extended viability of their cultures.[11] Here, we characterize a protocol for general fabrication of desired geometries of PDMS lids and their effectiveness at mitigating evaporation. A 3D-printed mold produced using Ninja Flex filament is shown in **Figure 2.14a** and

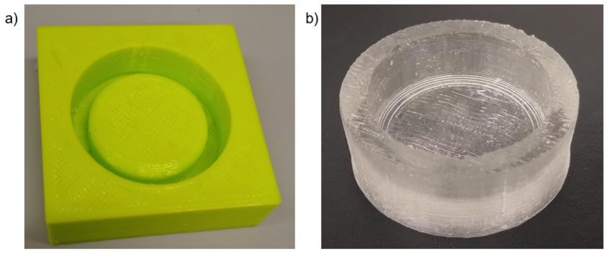

Figure 2.14 – a) 3D-printed NinjaFlex mold used to fabricate b) PDMS lid for use on cell culture dish.

is the basis for PDMS lid fabrication **Figure 2.14b**. This mold was designed using SOLIDWORKS and configured for 3D-printing. Having tested other filaments in use for 3D-printing, the Ninja Flex filament produces molds that have a relatively grater elasticity, which is an added benefit of when removing casted lids. In order to prevent adhesion of the uncured, PDMS to the 3D-printed mold, silanization is performed on the mold using chlorotrimethylsilane (CMS) in a sealed desiccation chamber under a slight vacuum. A similar protocol is used for glassware here.[12] The full details of the protocols used in fabrication of the PDMS lid are provided in **Appendix B.vi**.

While PDMS lid fabrication is theoretically scalable, it was of interest to test a similar solution utilizing semi-permeable, hydrophobic membranes that are commercially available such as the Breathe-Easy plate sealing films is tested (VWR, No. 102097-058). These membranes allow for the gas-exchange needed to maintain physiological pH in cell culture media while incubating, while preventing excess evaporation as well. Previous studies[11] using a thin membrane composed of fluorinated ethylene-propylene (FEP, Teflon®) have demonstrated long-term neuronal culture viability with weekly feedings. The Breath-Easy plate sealing film is readily applied by exposing the adhesive side and sealing with a silicone roller. The lid is still placed on top of the plate-sealing film, however, care is taken to remove any excess film so that the lid rests flush on the plate. The plate-sealing film is removed and replaced during routine replacement of the media  while under a biosafety culture hood.

## 2.7. Discussion

Measures were taken to ensure and to confirm viable neuronal cultures from careful management of the rodent colony to culture seeding and subsequent maintenance. At each step of neuron culture preparation all relevant factors were optimized for culture longevity. These factors included preparation of glass substrate, plating density, and culture maintenance.

The qualitative results in **Figure 2.10** are images of two cultures at 22 days in vitro with the only difference being the media replacement protocol. It is worth noting the data in **Figure 2.10** are for cell cultures in the corner regions of a 24 well plate, which are subject to relatively higher rates of evaporation than the other regions of the plate. The cell soma seen in **Figure 2.10a** are rounder and larger in comparison to those seen in **Figure 2.10b**. Moreover, there is a greater abundance of neural processes seen in **Figure 2.10a** than those seen in **Figure 2.10b** where instead, debris of necrotic neural processes is evident. Both the larger shape and size as well as the abundance of neural processes are clear indicators of the better health of the primary neuronal cultures imaged in **Figure 2.10a** when compared to the health of the culture seen in **Figure 2.10b**. Similar results were seen throughout the 24 well tissue culture plate.

A generalized model for evaporation for media contained in an incubator is validated using **Equation (2.2)** in **Figure 2.12.** These results confirm several assumptions relative to the incubator conditions used. Firstly, the exposed surface area is the perimeter of the microwell plate or dish and its product with the measured gap between the top interior of the lid and top of the plate. Secondly, the effective area for each well in a 12, 24, 48, and 96 microwell plate is found by dividing the plate lid area by $N_{eff}$ or the effective additional number of wells for each region needed to match the total evaporation observed in the corner wells. Thirdly, fluctuation between 90-99% relative humidity is the primary contribution to variations in the theoretical evaporation rate thus, reductions in relative humidity during at most 30 second intervals of opening and closing the incubator door are insignificant when spaced apart at least by 48-hour intervals. Therefore, with minimal assumptions this generalized model of evaporation is valid for a large range of areas found in several culture plates and dishes.

The qualitative data for the effects of osmolarity on cell culture viability suggests that changes in osmolarity have a large impact on the viability of long-term, cortical neuronal cultures. Therefore, considerations should be taken of the effects of passive evaporation on culture media osmolarity. Thus, throughout cell culture incubation, every 48-72 hours half media replacements were performed; that is half of the culture media calculated following expected evaporation is removed and replaced with half the original volume of media plus an additional volume of water to account for the evaporated volume. Robust cultures were observed at 29 days in vitro with regularity using this technique. Qualitative data is used to assess the viability of neuronal cultures because the differences are very evident after several weeks of incubation. Future investigations

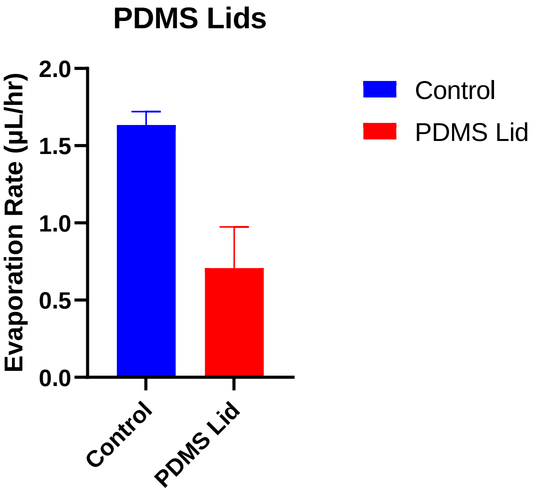

Figure 2.15 – Average evaporative rates for 35mm cell culture dish with controls using normal, associated lids and another using a PDMS lids.

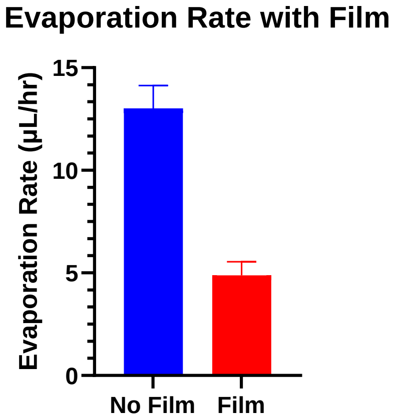

Figure 2.16 – Comparison of average evaporative rates observed for 24 microwell plate with and without the addition of Breath-Easy plate sealing film

should monitor quantitatively the health of cultures by measurement of the number of synapses formed.

Testing the PDMS fabricated lid with similar dishes using commercially provided lids yielded results for average evaporative rates shown in **Figure 2.15**. The results indicate that use of the PDMS lid nearly halves the effective evaporation rate. While this protocol  is applied only for a 35mm diameter cell culture dish, it can potentially be used for arbitrary geometries limited by the resolution of a 3D-printer. In comparison, the average evaporation rates for 24 microwell plates tested together with and without Breathe-Easy plate sealing film are shown in **Figure 2.16**. The plate sealing film reduces observed evaporation rates to nearly 30% of that observed in 24 microwell plates not using the film.

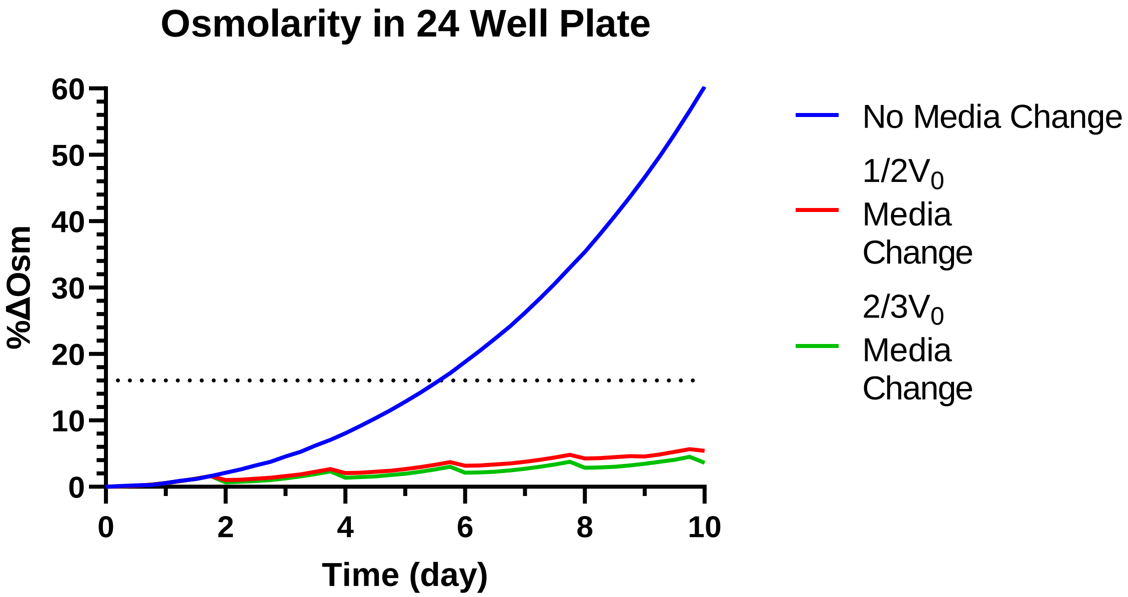

Figure 2.17 - Approximate change in osmolarity resulting from observed average evaporation in 24 microwell plate. Conditions involving media replacements using fractions of initial volume are shown. The dotted line indicates a threshold for a toxic rise in osmolarity at an approximately 16% increase.

From these studies, it is unclear how sensitive cortical neuronal cultures are to changes in osmolarity and whether there are perceived differences between the rate of change in osmolarity. Previous studies have indicated a rise of >50 mOsm is lethal to neuronal cultures[13], which would be about 116% of physiological osmolarity or 305 mOsm. Thus, according to the modelled changes in osmolarity shown in **Figure 2.9** but extended to DIV 10 in **Figure 2.17,** this threshold is reached just before DIV 6. Also seen in **Figure 2.17** is that the threshold for a toxic increase in osmolarity is unmet for both conditions of media replacements even by DIV 10 and it assumes a linear rise over spans of weeks. Additional studies that include direct measurements of osmolarity may provide further insight as to the tolerance of cortical neuronal cultures to shifts in osmolarity. In any case, culture maintenance appears optimized by minimizing effective rates of evaporation that a culture might experience throughout incubation. Incorporating hydrophobic membranes such as PDMS or plate-sealing films, significantly reduces the typical evaporation rates a cell culture might otherwise experience. Routine media replacement every 48-72 hours prevents the build-up of any unwanted metabolic by-products as well as excess change in osmolarity. Additionally, since regions of microwell plates experience varying evaporation rates one might benefit from leaving exterior wells unused and filled with water while isolating cell samples of interest in central region wells that experience relatively less evaporation.

The focus of investigations on these primary neuronal culture is the comparison of spontaneous calcium activity in wild type as compared to BACHD neurons. Huntington’s disease is a chronic neurodegenerative disorder that manifests symptoms over long periods of time. Thus, differences between the control and disease model are more readily resolved in cultures maintained for longer periods of time. Moreover, the ubiquitous nature of calcium activity in the cell necessitates the study of consistently, viable primary neuron cultures. Therefore, attentive maintenance of neuronal cell cultures allows for accurate collection of calcium emissions activity data and comparison of wild type and disease model cells.

## 2.8. Acknowledgements

Chapter 2, in part, is co-authored by Janna Sage and Sicily Panattil. Janna Sage contributed a significant portion of evaporative rate measurements. Sicily Panattil contributed greatly to the design and to the fabrication of a 3D printed mold used to investigate evaporation mitigation studies with a PDMS based lid. The dissertation author was the primary author of this chapter.

## CHAPTER REFERENCES

1. E. Roze, C. Bonnet, S. Betuing, and J. Caboche, “Huntington’s Disease,” *Disease of DNA Repair*. pp.45-52, 2010.

2. M. Gray, D.I. Shirasaki, C. Cepeda, V.M. André, B. Wilbrun, X. Lu, J. Tao, I. Yamazaki, S. Li, Y.E. Sun, X. Li, M.S. Levine, and X.W. Yang, “Full-Length Human Mutant Huntingtin with a Stable Polyglutamine Repeat Can Elicit Progressive and Selective Neuropathogenesis in BACHD Mice,” In *Neurobiol. Dis.*vol. 28, pp.6182–6195, 2008.

3. X. Zhao, X. Chen, E. Han, Y. Hu, P. Paik, Z. Ding, J. Overman, A.L. Lau, S.H. Shahmoradian, W. Chiu, L.M. Thompson, C. Wu, and W.C. Mobley, “TriC subunits enhance BDNF axonal transport and rescue striatal atrophy in Huntington’s disease,” *Proc. Natl. Acad. Sci.*, vol. 113, no. 38, pp. E5655–E5664, 2016.

4. C. Landles and G. P. Bates, “Huntingtin and the molecular pathogenesis of Huntington’s disease. Fourth in molecular medicine review series,” *EMBO Rep.*, vol. 5, no. 10, pp. 958–963, 2004.

5. C.A. Fisher, K. Sewell, A. Brown, A. Churchyard, “Aggression in Huntington's disease: a systematic review of rates of aggression and treatment methods,” *J Huntingtons Dis.*, vol.3, no.4, pp.319-332, 2014.

6. D. K. Cullen, M. E. Gilroy, H. R. Irons & M. C. Laplaca, “Synapse-to-neuron ratio is inversely related to neuronal density in mature neuronal cultures,” *Brain Res*., vol. 1359, pp.44-55.

7. C.M Waterman-Storer, “Microtubule/Organelle Motility Assays,” *Current Protocols in Cell Biology*, vol. 00, pp.13.1.1-13.1.21.,1998.

8. G. D. Rosen and R. W. Williams, “Complex trait analysis of the mouse striatum: independent QTLs modulate volume and neuron number,” *BMC neuroscience*, vol. 2, no. 5, 2001.

9. S. Herculano-Houzel, “The human brain in numbers: a linearly scaled-up primate brain,” *Frontiers in human neuroscience*, vol. *3*, no. 31, 2009.

10. Engineering ToolBox, “Evaporation from a Water Surface,” [online], 2004, Available at: https://www.engineeringtoolbox.com/evaporation-water-surface-d_690.html [Accessed 4 Feb. 2021].

11. A. Blau, T. Neumann, C. Ziegler, amd F. Benfenati, “Replica-moulded polydimethylsiloxane culture vessel lids attenuate osmotic drift in long-term cell cultures,” *J. Biosci.,* vol. 34**,** pp.59–69, 2009.

12. B. Seed, “Silanizing glassware,” *Current Protocols in Immunology*, vol. 21, pp.A.3K.1 – A.3K.2., 1997.

13. S. M. Potter and T. B. Demarse, “A new approach to neural cell culture for long-term studies,” *J. of Neuroscience Methods,* vol. 110, pp. 17–24, 2001.

# Chapter 3: Calcium Imaging Studies on Primary Cortical Neurons

## 3.1. Overview

Huntington's disease (HD) is a dominantly inherited neurodegenerative disorder that currently has no disease-modifying treatment. Mutant Huntingtin protein (mHTT) features an expanded stretch of glutamine residues (polyQ) near the N-terminus; the mutant protein induces widespread changes in neurons that affect axonal trafficking and signaling, synaptic function, gene expression, mitochondrial function, calcium homeostasis, and proteostasis. Changes in calcium homeostasis are believed to contribute to pathogenesis by negatively impacting neuronal function and survival.[1] Calcium plays a defining role in many aspects of neuronal signaling, including those linked to synaptic plasticity. Neurons gain access to calcium from the extracellular fluid as well as from internal membrane-bound stores present in endoplasmic reticulum (ER). Calcium entry into the neuronal cytosol from both sources is induced by activation of specific ligand-receptor systems as well as neuronal activity. While several disease models have been employed to study calcium dysregulation, here the spontaneous calcium activity for BACHD is characterized across several days of incubation. In addition, a custom, GUI-based software tool used for analysis of fluorescence emissions data referred to as Fluorescence Emissions Signal Analyzer or FESA is described.

### 3.1.1. Related Studies on Calcium Dysregulation

Homeostatic maintenance of calcium is essential for normal neuronal signaling; moreover, effectively modulating calcium levels protects neurons in the setting of increased neuronal excitation and calcium entry. It is well established that calcium homeostasis differs between wild-type neurons and those that model HD.[1-8] For example, increased basal levels of intracellular calcium are present and mitochondria isolated from cells obtained from HD patients are more sensitive to calcium loading.[2] One clue to abnormal regulation comes from studies of the Ryanodine Receptor (RyR), which is in the ER. RyR dysfunction, as reflected in R6/2 HD mouse models, is posited to cause excessive calcium leak from ER into the cytosol with consequent reduced calcium in intracellular membrane stores.[3] Increased cytosolic calcium could dysregulate the activity of calcium binding proteins, including kinases; decreased intracellular stores could blunt responses to signaling events. Another clue is that mHTT sensitizes the inositol tri-phosphate receptor (IP3R), also present in the ER membrane, to IP3; this enhances calcium release in response to activation of metabotropic glutamate receptors.[1,4] Finally, there is evidence that in HD there is a relative increase in the ratio of extrasynaptic N-methyl-D-aspartate receptors (exNMDARs) to synaptic NMDARs (sNMDARs); an increased ratio of extrasynaptic to synaptic receptors has been linked to inhibition of cell survival and plasticity.[5,6] Studies of NMDAR activation point to increased duration of the calcium response, but not its peak, in HD models.

There is compelling evidence for mHTT-induced mitochondrial dysfunction and calcium dysregulation. In human tissues and HD models deficits in energy metabolism were attributed to mitochondrial dysfunction.[8] Mitochondrial transport and morphology were also impacted. Trafficking defects preceded changes in neuronal function in HD models in vitro and in vivo[8]. Reduced trafficking may be linked to changes in morphology of mitochondria[7,9]. mHTT down-regulated mitochondrial biogenesis, in HD brain and models, via reduced expression of the peroxisome proliferator-activated receptor gamma coactivator 1 alpha (PGC1a) $Ca^{2+}$ buffering in mitochondria is reduced in cells expressing mHTT; the mechanism(s) is uncertain, but cells expressing mHTT show reduced mitochondrial membrane potential that depolarize at lower $[Ca^{2+}]$[10]. $Ca^{2+}$ dysregulation also results from non-mitochondrial sources; mHTT, but not wHTT, interacts directly with the Inositol 1,4,5-trisphophate receptor type 1 ($InsP_3R1$) with dysregulation of calcium flux from the ER.[1,3] Store operated calcium entry (SOCE) may also be affected.[1]

## 3.2. Fluorescence Microscopy

For fluorescence studies, while a majority of experiments were performed using a Leica DMI6000B (Leica Microsystems Wetzlar GmbH, Wetzlar, Germany) with an external acrylic, cell incubation chamber a few experiments were also performed using a Zeiss Axiovert 200M (Carl Zeiss, Thornwood, NY) with an Ibidi stage top incubation system (10720, ibidi GmbH, Gräfelfing, Germany). Experiments using the latter microscope were transferred to an incubation chamber in another lab at last 24 hours prior to the start of experimentation. All samples were imaged under similar conditions unless otherwise stated. Two primary fluorescent probes are used throughout these studies Fluo 4-AM with excitation wavelength of 494 nm and emission wavelength of 516 nm (50018, Biotium, Fremont, CA) and Hoechst 33258 (40044, Biotium, Fremont, CA) with excitation wavelength of 352 nm and emissions wavelength of 461 nm. Fluo 4 is a calcium-sensitive fluorescent indicator that produces a significant increase in emissions intensity when bound to calcium. Hoechst 33258 is a supravital, nuclear fluorescent stain that only fluoresces when bound to DNA. In both microscope configurations, a DAPI filter cube with an excitation filter with bandpass 360/40 nm, a dichroic mirror with cut-off wavelength of 400 nm, and emissions filter of 470/40 nm was used for imaging with Hoechst 33258. Additionally, a FITC filter cube with an excitation filter with bandpass 480/40 nm, a mirror dichroic with cut-off wavelength of 505 nm, and an emissions filter with bandpass 527/30 nm was used for imaging Fluo 4.

Illumination intensities were selected by optimizing for signal to noise ratio[11] (SNR) using analytical tools in ImageJ while also minimizing the effects of photobleaching during the imaging of samples under a range of select irradiances. Power measurements of the excitation source intensity was performed at 494 nm using an optical power meter (1918-C, Newport, Altamonte Springs, FL 32714) and silicon based sensor (918D, Newport, Altamonte Springs, FL 32714). Several fields of view were analyzed for photobleaching rate of decay where the intensity is given by $I = I_0 \, \mathrm{e}^{-kt} + const$ where the initial intensity, $I_0$, decays exponentially as a function of time by decay rate, $k$. The decay rates for selected irradiances are plotted as a function $1/k$ alongside normalized values measured for SNR in **Figure 3.1**.

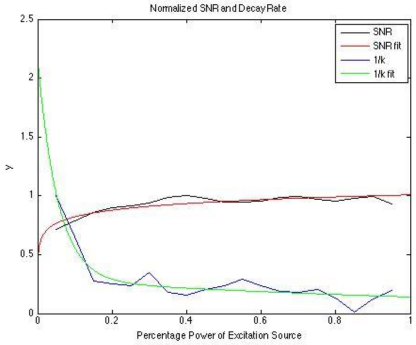

Figure 3.1 – Fitted data for normalized SNR and 1/k for decay constant, k, acquired by varying the intensity of the excitation source used to induce fluorescence of Fluo 4 in samples.

Irradiance measurements in **Figure 3.1** are shown as a percentage of a maximum power of 114.25 mW/cm$^2$. As shown in **Figure 3.1** the fit of normalized SNR data of the sample intersects with a fit of $1/k$ at 7% or 6.82 mW/cm$^2$. Therefore, the irradiance for fluorescent microscopy experiments is maintained at 6.82 mW/cm$^2$ using a combination of neutral density filters and/or mechanical shutters acting as attenuators for all fluorescent-based imaging experiments. All calcium-imaging experiments were imaged at a framerate of 10 Hz or greater, however, additional exposures at 1 Hz were acquired for the purposes of region of interest (ROI) segmentation.

## 3.3. Emissions Intensity Signal Analysis

All analysis of imaging data is performed on a custom, open-source, GUI-based software using MATLAB (ver. R2020b) referenced as the Fluorescence Emissions Signal Analyzer or FESA.[12] FESA is a one-stop, GUI-based software workbench for processing raw imaging data that provides automated segmentation of ROIs, both extraction of emissions signal activity and transient peak parameters, and high-throughput capabilities. Users can load several consolidated *.tif* imaging files or TIFF stacks (*.ome*) as well as folders containing series of individual *.tif* images. Users can define channels for grouped sets of imaging data for image processing. All work performed using FESA can be saved locally and accessed at later dates. A detailed manual for usage of FESA is available on GitHub[12] where it can be downloaded for free.

### 3.3.1. Region of Interest Segmentation

By default the first image of a TIFF stack or series is used for ROI segmentation unless otherwise selected. Two methods of segmentation can be used the first being gradient-based segmentation, which computes a gradient magnitude image that reflects local changes in pixel intensity in both horizontal and vertical directions. Then, an adjustable, binary threshold of the gradient magnitude image is used to obtain the segmented results. The second method of segmentation queries the user to draw lines marking desired foreground and background regions. After both selections are made, an iterative graph-based segmentation is performed based on the linkage of super-pixels. While the process of generating ROIs is automated, the user can manually filter and add ROIs which may or may not have been included in error. The final collection of ROIs is saved locally and used throughout additional functionalities of FESA. Typical results can be used to generate plots of emissions intensity activity for select ROIs as shown in **Figure 3.2**.

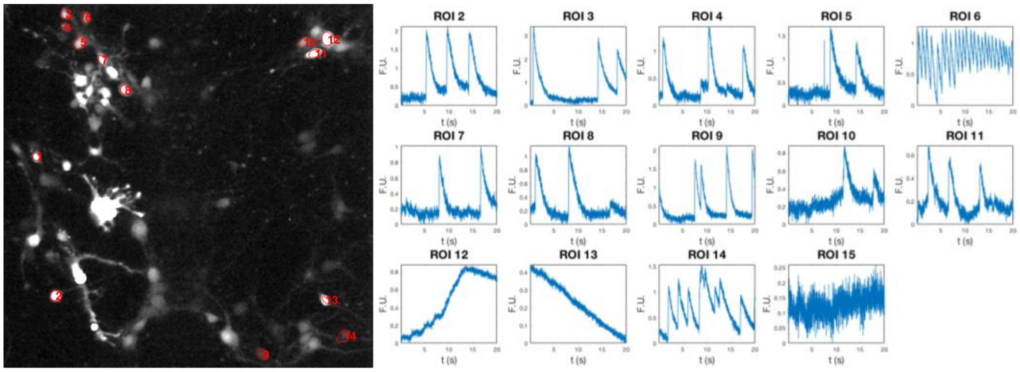

Figure 3.2 - Z-projection of average intensity data (left) of emissions intensity data from cortical neurons at 7 DIVs and corresponding time-acquisition of Fluo 4 emissions intensity (right) acquired at 10 Hz. The emissions intensity data is graphically represented for corresponding ROIs in plots to the right.

In addition to generating ROIs from imaging data, FESA can analyze pairs of ROIs and find overlapping ROIs. Pairs of ROIs can be used to generate new ROIs that exclude or include sub-regions of ROIs that overlap between pairs of ROIs. For example, in this study ROIs found for Hoechst fluorescence emissions data is used to exclude nuclear regions from overlapping ROIs from Fluo 4 emissions data and vice versa. The result is an approximation for sub-cellular calcium activity within the cytosol and nucleus that is used later to localize differences in intracellular calcium activity.

### 3.3.2. Peak Parameter Extraction

Raw emission data is extracted as mean pixel intensities within ROIs from *.tif* images using FESA and the workflow described in **Figure 3.3**. The results of analysis identify individual transient peaks in data and formulate a baseline fit in order to reinterpret raw data as $\frac{\Delta F}{F_0}$. Then follows extraction of defined peak parameters from individual transient peaks detected in emissions intensity data. Peak parameter values extracted during analysis include amplitude, FWHM, $A_{FWHM}$, $A_B$, and frequency. To characterize calcium buffering capacity, values for areas underneath the FWHM for each transient peak ($A_{FWHM}$) and values for areas underneath the baseline fit ($A_B$). In order to compare values across experiments, $A_B$ is normalized by acquisition time and is representative of average area under the baseline per unit time. Here, $A_{FWHM}$ represents the accumulation of calcium for a given transient peak while $A_B$ is representative of the basal intracellular accumulation of calcium in the cell. The amplitude is a peaks maximum value measured relative to the baseline value just before a peak. The full-width at half-maximum (FWHM) is calculated for each peak along with the period between peaks to then calculate frequency. Therefore, values for frequency are only calculated when there are at least two or more peaks present in a data set. In addition, the both the mean and peak values are measured for rise and fall rates of transient peaks detected in signal data. The mean rise rate is calculated by taking the mean of positive values along the first half of the FWHM,

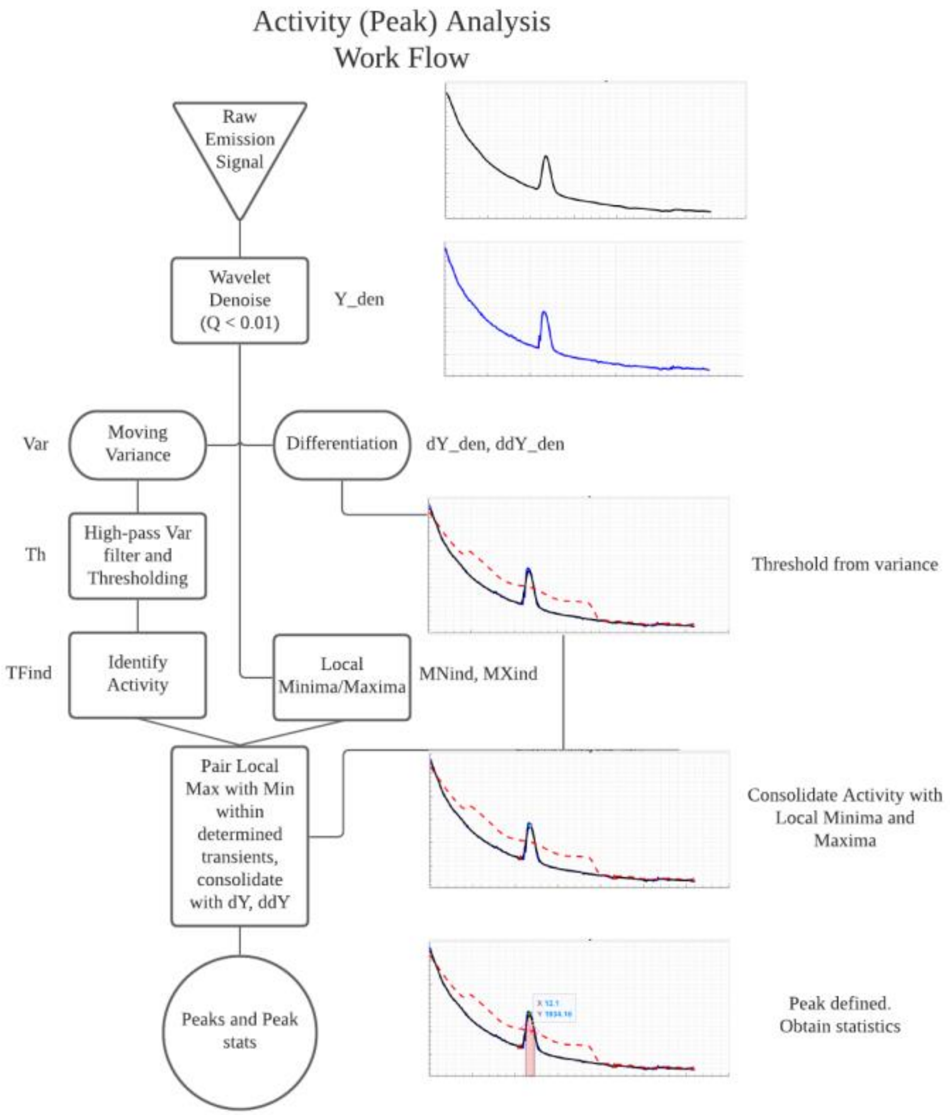

Figure 3.3 – Diagram of work flow for activity or peak analysis performed on raw, Fluo 4 emissions intensity data.

while the peak rise rate is the maximum along this domain. The mean fall rate is calculated by taking the mean of negative values along the second half of the FWHM, while the peak fall rate is the minimum along this domain.

A general wavelet denoise function *wdenoise()* using the reverse biorthogonal 5.5 wavelet (ribio5.5) is first applied to the raw signal. Wavelet denoising deconvolves the raw signal into multiple functions (levels) and applies thresholding of the functions' coefficients to decrease the contribution of certain frequencies to the signal. This allows the application to magnify the expected signal. Here the application specifies that the thresholding be applied so that the expected False Discovery Rate (FDR) does not exceed 1%. Call the resulting signal Y_den (denoised).

The denoised signal Y_den is then smoothed with a Gaussian-weighted moving average filter generating Y_smth. The window of rolling average is determined as the product of minimum expected duration of transient signal (peak) in seconds with the acquisition rate in Hz. The first and second-order derivatives dY and ddY, respectively, used throughout analysis is computed from the denoised signal, Y_den. The moving variance of the denoised signal Y_den and its first and second order derivatives dY and ddY are computed. The window used is the product of expected duration of transient/peak (T) and acquisition rate (f). The variance of denoised signal and its derivatives are referred to as Var Y , Var dY , and Var ddY, respectively.

Intervals in the emissions intensity data and its derivatives that contain peaks or transient activity are assumed to have higher variance values compared to intervals without transient activity. Therefore, we are interested in finding a threshold for variance in signal data that distinguishes intervals with and without activity. To obtain the threshold, the variance (Var Y) is subjected to a 1D continuous wavelet transform using the function *cwt()*. A continuous wavelet transform retains information of when in time events occur in the frequency-spectrum with respect to time-domain signals. The term wavelet refers to a small wave that is an oscillatory function of finite length and of two variables scale and translation. The scale parameter can be thought of as a measure of resolution for frequency where low values correspond to a more detailed view of the frequency-spectrum. The translation parameter is used to translate the window of the wavelet across a signal. While not a requirement, most basis functions of wavelets are orthonormal. A wavelet of set scale is multiplied by the signal and integrated over all time at some time with set translation. One row of the time scale is completed once the wavelet is shifted across the entire time-domain signal a set value of scale. This process is repeated for every value of scale. In other words, a set of frequencies (scale of analysis wavelets) is generated such that for an input of an n by 1 vector of moving variance (real numbers), the output of *cwt()* is an n by m 2D matrix, where n is the size of set of frequencies ordered from low to high and m is the length of the moving variance vector. As depicted in **Figure 3.4**, a high-pass filter is iteratively applied to the output set of frequencies by eliminating values for frequency that are below a cut-off value.

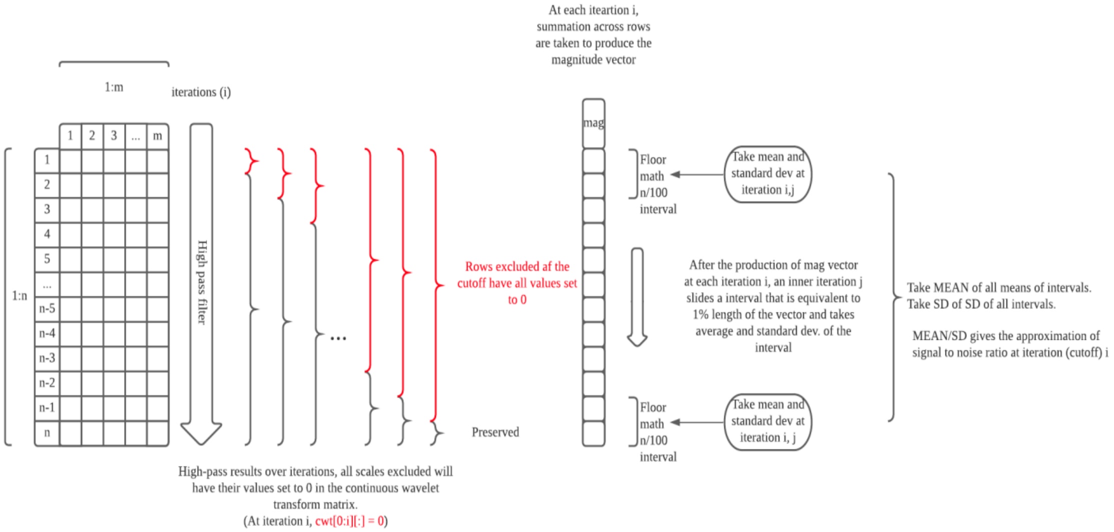

Figure 3.4 – Diagram for high-pass filter of moving variance data for denoised, Fluo 4 emissions intensity data.

At each iteration with a cut-off applied, values of each row are summed to produce a

1 by n magnitude vector referred to as mag. Each i-th row of the continuous transform is representative of the contribution of i-th frequency to each segment of the moving variance and summing up each row yields the net contribution of frequency i-th to the entire variance vector. Subsequently, a moving average and moving standard deviation are found for the mag vector using a window 1% the length of mag. The mean (MEAN) or $\mu_{mag}$ and the standard deviation (SD) or $\sigma_{mag}$ are used to approximate a signal to noise ratio (SNR) for each cut-off frequency as $\frac{\mu_{mag}}{\sigma_{mag}}$. The optimal frequency cut-off is determined as the last cut-off value that results in a greater than 1% improvement from the previous SNR value or $(SNR_i - SNR_{i-1})/SNR_{i-1} >$ 1%. The variance threshold is defined and calculated as,

$$Threshold = \frac{\mu_{mag} + 2.58\sigma_{mag}}{\mu_{SNR} + 2.58\sigma_{SNR}}$$

Where the mean values for mag and SNR vectors, $\mu_{mag}$ and $\mu_{SNR}$, respectively, and standard deviation values for mag and SNR vectors, $\sigma_{mag}$ and $\sigma_{SNR}$, are found for the optimal cut-off frequency. The value of 2.58 is used to find the multiple of standard deviation that would include 99% of an assumed normal distribution. SNR can be interpreted as the average magnitude of a signal over the standard deviation of a signal. Thus, the threshold value represents an upper-boundary or deviation from baseline that would include noise. With the optimal cutoff determined, the input variance is reconstructed using the cut-off frequency value. **Figure 3.5** illustrates the resulting moving variance for denoised data before and after high-pass filtering.

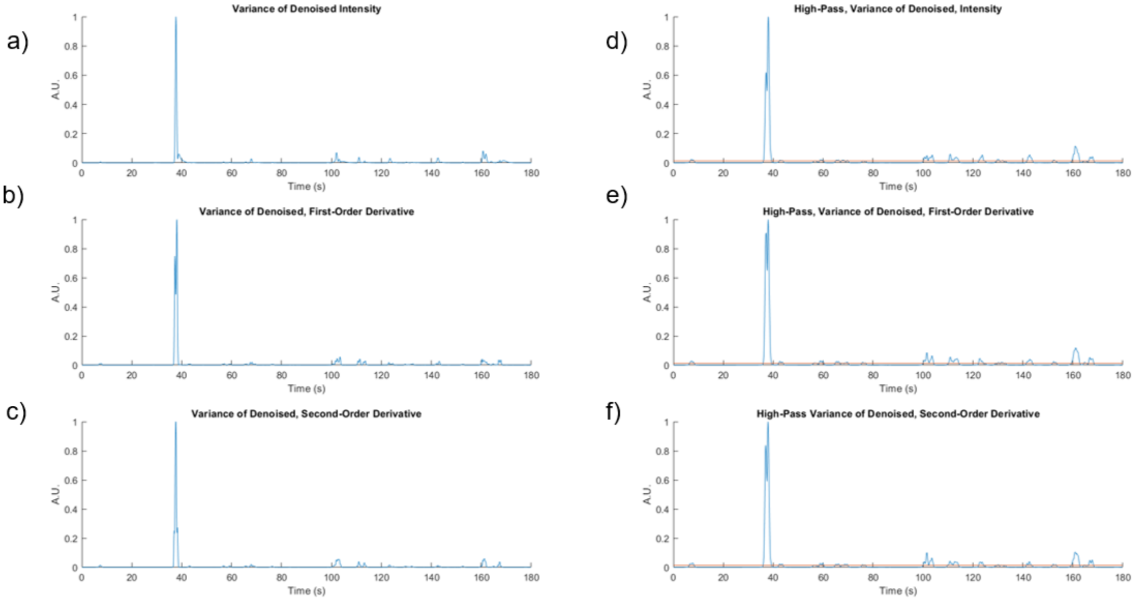

Figure 3.5 – Normalized moving variance for denoised emissions intensity data both first and second order derivatives (a-c). High-Pass filter of variance data (a-c) shown with threshold value (orange) for signal considered above noise (d-f).

Using the high-pass filtered variance data, a process of isolating transient peaks starts with first finding domain values that indicate changes in linearity of the data. Change points are found along denoised emissions data as well as derivatives and considered valid if contained to regions that have variance values exceeding the calculated threshold. The changes points found for select emissions data is shown in **Figure 3.6.** These domain values are grouped and used as intervals for finding local minima and maxima that are used to identify individual, transient peaks. Subsequent

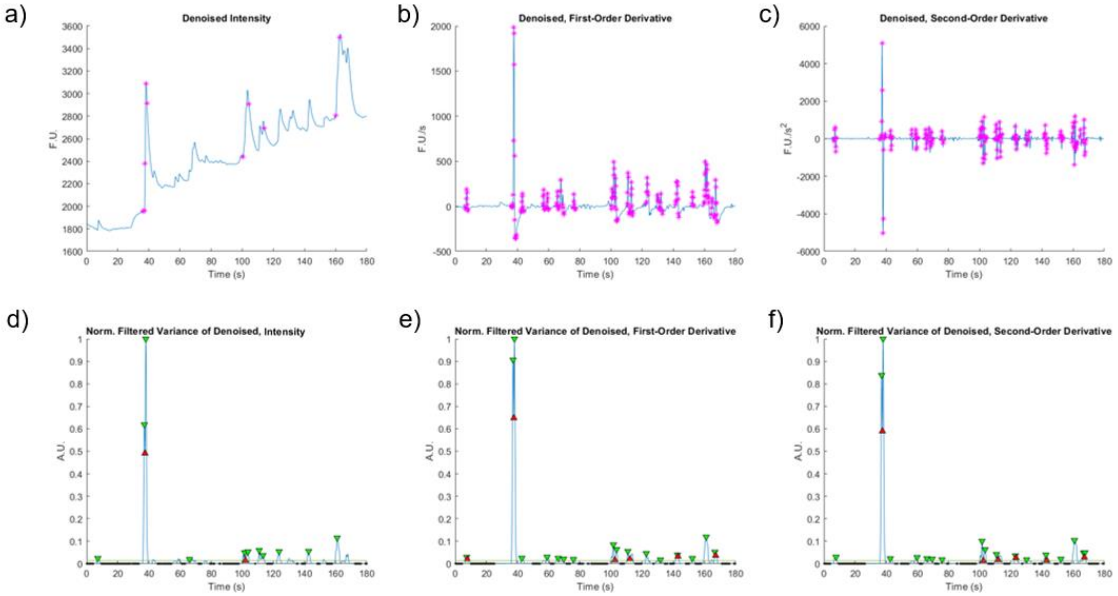

Figure 3.6 – Denoised emissions intensity data with both first and second order derivatives (a-c), with change points indicated by magenta asterisks (*). Change points are datapoints that exceed threshold values for changes in linearity of both variance and emissions intensity data. The normalized filtered variances for data (a-c) is shown, respectively in plots (d-f) with local maxima (green,downward triangels) and local minima (red, upward trangles) is labelled as well.

analysis of first and second-order derivative data for specified intervals of interest or used for further identification and isolation of individual, transient peaks. Additional domain values that are found to contain regions of variance below the threshold are used to formulate a baseline $F_0$ for the emissions intensity data based on Fourier series fit. The result of signal analysis is shown in **Figure 3.7** where **Figure 3.7.a)** depicts the change in fluorescence $\Delta F = F - F_0$ relative to the formulated baseline signal $F_0$ and **Figure 3.7.b)** depicts intensity data. Both plots in **Figure 3.7** include denoised data (black), peak threshold (dashed, red) and the labelling of local maxima and minima, as well as intervals of full-width at half-maximum for each detected peak. In order to more accurately compare changes in signal intensity relative to baseline across multiple experiments, statistical analysis is performed following signal analysis of $\frac{\Delta F}{F_0}$.

Table 3.1 – Experiments for specified days of incubation in vitro (DIV) with experimental dates. Wells and trials are shown for wild type samples (WT) and for BACHD in parenthesis. The average number of neurons per trial found with transient activity is shown for wild type, ($N_{WT}$) BACHD ($N_{BACHD}$), and combined ($N_{tot}$) samples alongside respective standard deviations.

| DIV | Date | Wells/WT(BACHD) | Trials/WT(BACHD) | $N_{WT}$ | $N_{BACHD}$ | $N_{tot}$ |
|---|---|---|---|---|---|---|
| 6 | 2/13/2020 | 5 | 7(5) | 4 ± 3 | 5 ± 3 | 5 ± 3 |
| | 2/28/2020 | 5(6) | 4 | 4 ± 1 | 7 ± 4 | 5 ± 3 |
| 7 | *7/17/2018 | 4 | 4 | 21 ± 3 | 10 ± 5 | 15 ± 7 |
| | 11/27/2019 | 3(4) | 4 | 42 ± 8 | 29 ± 22 | 35 ± 17 |
| | 1/27/2019 | 4(3) | 11(8) | 11 ± 7 | 23 ± 9 | 18 ± 9 |
| | 2/14/2020 | 2 | 5 | 24 ± 10 | 32 ± 15 | 28 ± 13 |
| 8 | 1/30/2020 | 6 | 15 | 13 ± 8 | 27 ± 14 | 21 ± 13 |
| 9 | 11/29/2019 | 6 | 6 | 17 ± 16 | 12 ± 9 | 17 ± 12 |
| | 12/12/2019 | 6 | 12 | 9 ± 4 | 8 ± 5 | 8 ± 5 |
| | 3/2/2019 | 5(6) | 9 | 5 ± 3 | 6 ± 3 | 5 ± 3 |
| 10 | *6/1/2018 | 1 | 5 | 35 ± 9 | 14 ± 9 | 24 ± 13 |
| 12 | *6/3/2018 | 1 | 9 | 11 ± 3 | 17 ± 4 | 14 ± 5 |
| 13 | 12/16/2019 | 3 | 3 | 35 ± 20 | 24 ± 6 | 29 ± 15 |
| | 2/20/2020 | 3 | 4 | 6 ± 4 | 7 ± 5 | 6 ± 4 |
| 14 | 5/23/2019 | 3 | 3 | 13 ± 11 | 13 ± 4 | 13 ± 7 |
| | 12/4/2019 | 3 | 4 | 9 ± 3 | 12 ± 3 | 10 ± 3 |
| | 12/17/2019 | 1 | 5 | 25 ± 14 | 25 ± 17 | 25 ± 14 |
| 19 | 4/16/2019 | 1 | 5(6) | 5 ± 1 | 12 ± 5 | 8 ± 5 |
| | 11/4/2019 | 3(2) | 4 | 11 ± 6 | 27 ± 11 | 19 ± 12 |

### 3.3.3. Statistical Analysis

Data acquired from the analysis of emissions intensity data were compared between wildtype and BACHD genotypes as well as monitored across various days in vitro (DIVs). Experiments with respect to DIV and experimental date are listed in **Table 3.1** with respective trial and population sizes. Parameter values of amplitude, full-width at half-maximum (FWHM), area under the FWHM ($A_{FWHM}$), area under baseline ($A_B$), and frequency are found for individual, transient peaks in emissions intensity data. Then, these parameter values are averaged for a given region of interest or cell. Subsequently, average values for a given trial or field of view are averaged to find a trial

average.

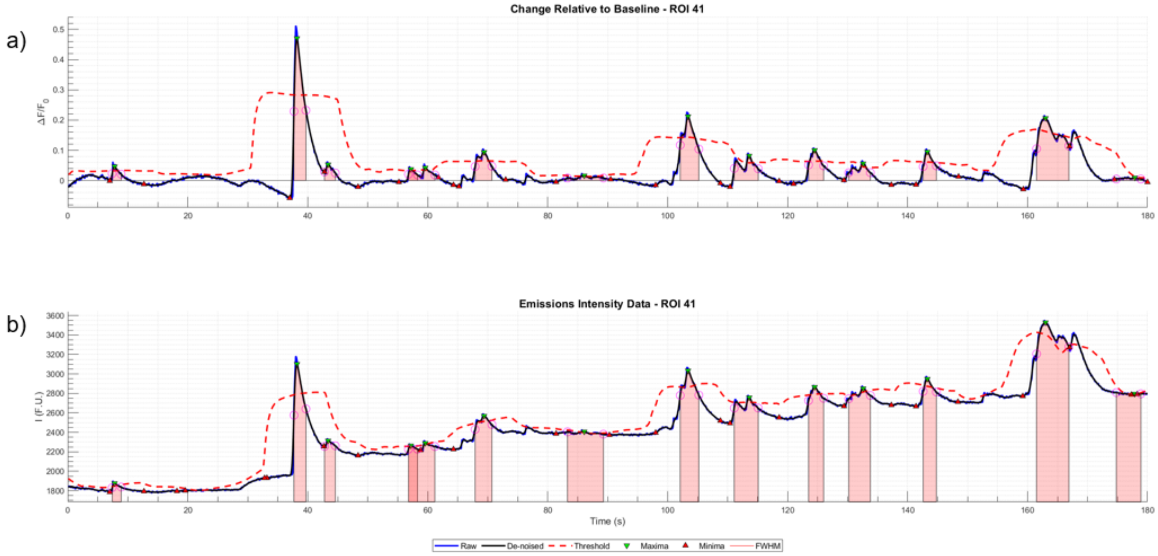

Figure 3.7 – Results of signal parameter extraction for region of interest (ROI) or single cortical neuronal soma. The relative change in fluorescence relative to the baseline, $\frac{\Delta F}{F_0}$, is shown in plot (a) while the raw emissions intensity data is shown below in plot (b). Both (a-b) include raw data (blue), denoised data (black), and the peak threshold (dashed, red). The local maxima (green, downwards triangle) and minima (red, upwards triangle) are labelled. The area under the curve is shown for intervals of full-width at half-maximum (FWHM) found for each detected peak.

These trial averages are compared at different DIVs for each genotype. Sets of data for DIVs were grouped by 6 DIVs, 7 DIVs, 8-9 DIVs, 10-12 DIVs, 13-14 DIVs, and 19 DIVs. When normalizing BACHD trial averages, wildtype averages measured on the same experimental date are used. Averages are found for replicates on a given experimental date for wild type parameters, then the BACHD values are normalized by that average to find ratio data. The ratio data found is considered non-parametric. To determine the statistical significance of normalized values a one-sample Wilcoxon signed-rank test is performed to test whether the population set comes from a symmetric population with a specified median of 1.0 or the expected value for wild type parameters. Asterisks are included above individual data points to denote the statistical significance following a Wilcoxon signed-rank test according to measured p-values, P where (*) P<0.05, (**) P<0.005, (***) P<0.001, and (****) P<0.0001. Data sets without statistical significance are labelled (ns).

## 3.4. Results

### 3.4.1. Spontaneous Calcium Activity in BACHD Cortical Neurons

Spontaneous calcium activity is defined as the emission intensity activity of Fluo 4 contained within the cell body of primary cortical neuron. The average for trials across 6-19 DIVs is shown in **Figure 3.8**. The average values for trials are shown with respective horizontal error bars indicating standard deviation for sets of DIVs used for that data point and vertical error bars indicating the standard error of the mean. The averages for each parameter across all DIVs is shown in **Figure 3.8** as dashed lines where red and blue are, BACHD and wildtype averages, respectively.

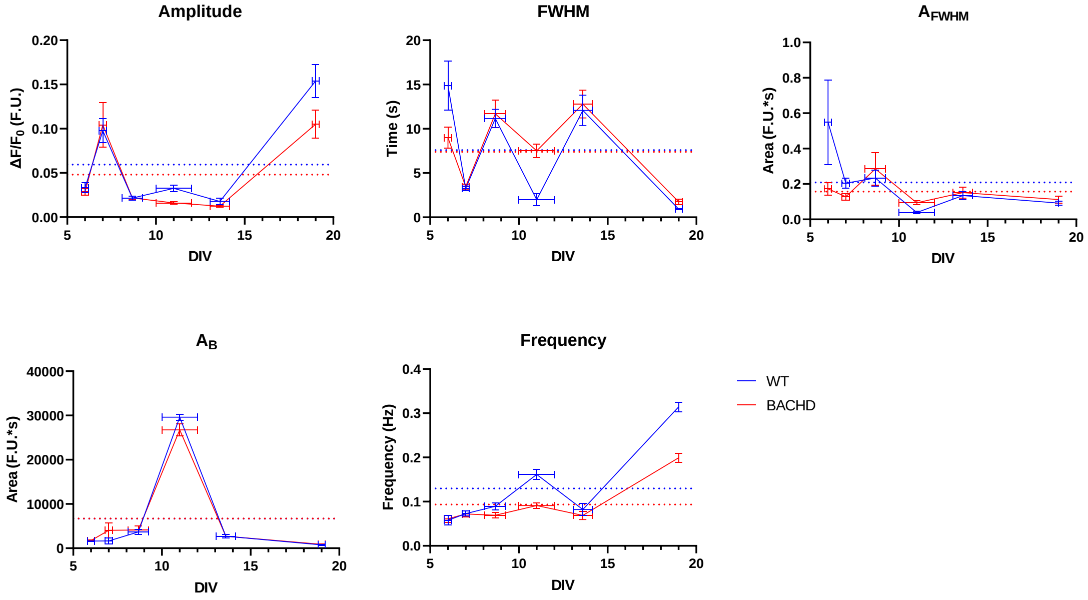

Figure 3.8 – Average parameter values plotted against day in vitro (DIV) of incubation. Data is grouped by wildtype (WT, blue, circle) and BACHD (red, square). Dashed lines represent averages across all DIVs for WT (blue) and BACHD (red). Averages were for several trials across multiple wells and experimental dates. The trial number or sample population size for 6, 7, 8.7, 11, 13.6, and 19 DIVs where N = [11,21,45,14,16,9].

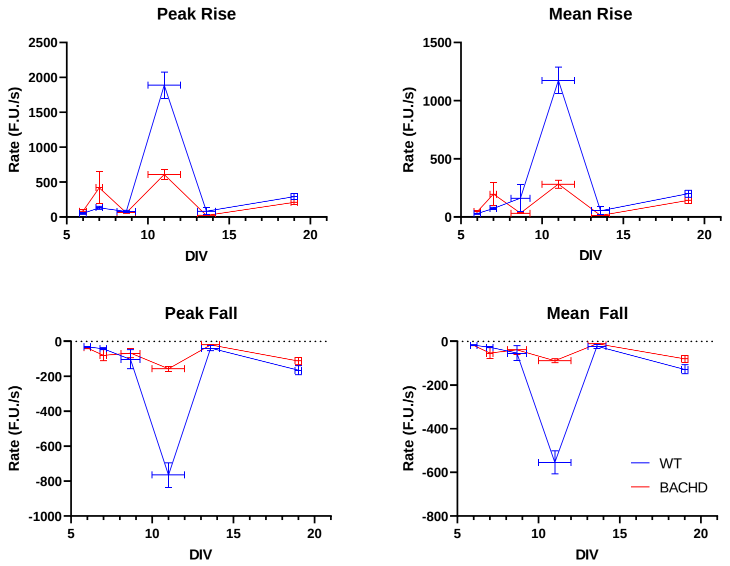

Figure 3.9 – Average mean and peak values for rates plotted against day in vitro (DIV) of incubation. Data is grouped by wildtype (WT, blue, circle) and BACHD (red, square). Dashed lines represent averages across all DIVs for WT (blue) and BACHD (red). Averages were for several trials across multiple wells and experimental dates. The trial number or sample population size for 6, 7, 8.7, 11, 13.6, and 19 DIVs where N = [11,21,45,14,19,9].

The average values for mean and peak rates are shown for sets of DIVs in **Figure 3.9.** In general, the differences between average parameter values of wild type and BACHD genotypes appear most significant at or after 10-12 DIVs. Synaptic formation is thought to occur at about 10 DIVs so, this group of DIVs would be most representative of changes in intracellular calcium activity resulting from a sudden increase in synaptic activity. A trend of lower, average amplitude values for BACHD neurons appears at DIVs 10-12 and is sustained throughout the data set with the greatest discrepancy between wildtype values appearing at DIV 19. On average, BACHD neurons exhibit lower values for frequencies, amplitudes, and FWHM values that result in lower values for $A_{FWHM}$. The area under the baseline, $A_B$, in **Figure 3.8**

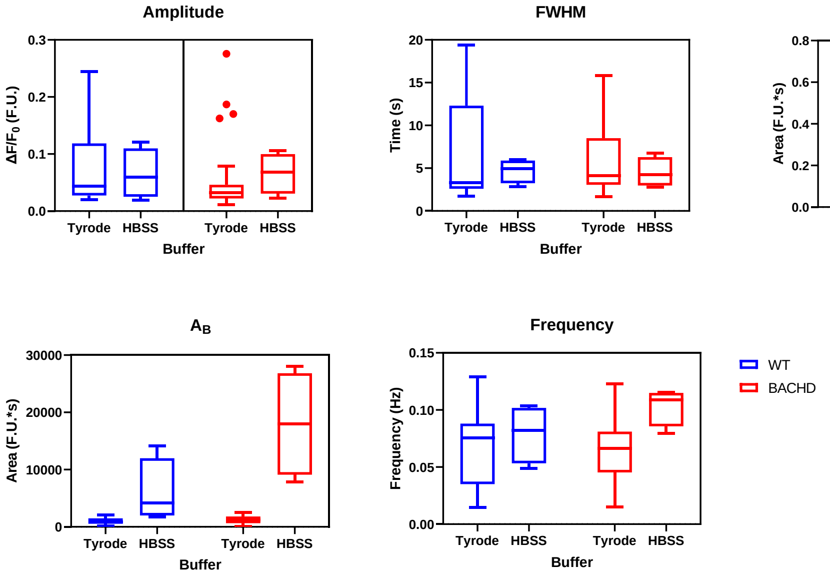

Figure 3.10 – Tukey whisker-box plots for parameter values at DIV 7 for each genotype under varying buffer conditions. Population sizes for Tyrode and HBSS conditions are 27 and 4, respectively.

does not show obvious differences. Interestingly, the absolute value of both rates increases with increasing $A_B$, which is suggestive of its link to calcium influx.

All DIVs except those representing DIVs 11-12 had data acquired using a dye loading protocol using Tyrode's solution while DIVs 11-12 use Hank's buffered saline solution (HBSS) with calcium and continued in use throughout image acquisition. Experiments comparing parameters measured between the two buffer conditions at DIV 7 is shown in **Figure 3.10.** The Tukey whisker box plots in **Figure 3.10** show great similarities in the range of parameter values found for both genotypes in either buffer condition. In addition, WT and BACHD values observed in varied buffer conditions are normalized by wild type values and compared in **Figure 3.11.** There are not any significant differences between average values or normalized values when testing for buffer condition. Thus, the average values for trials during DIVs 11-12 are compared with other values.

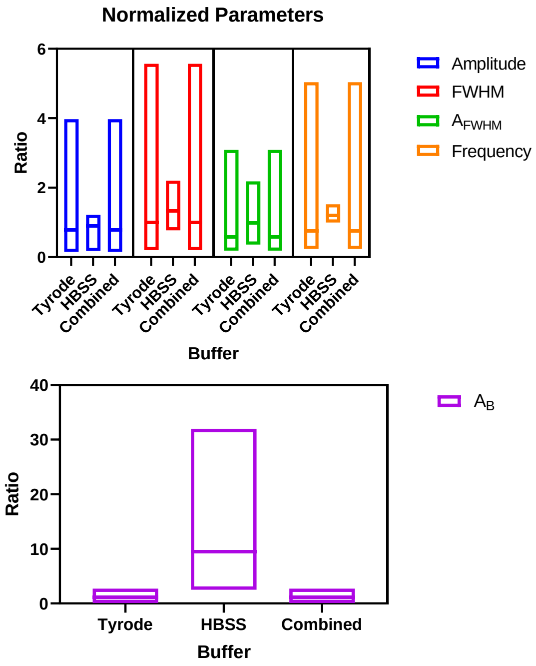

Figure 3.11 – Box plot of normalized BACHD parameter values. Values are normalized by wild type control values. Line in box plot shows median. Interquartile ranges are given by edges of boxes. Population sizes for Tyrode and HBSS conditions are 27and 4.

To further gauge statistical differences between observed values, BACHD parameter values are normalized by trial values observed on the same experimental date for wild type samples. The median for sets of normalized BACHD parameter values are shown in **Figure 3.12.** In **Figure 3.12**, a similar trend is seen for amplitude where the lowest amplitudes are seen at DIVs 6 and 7, DIVs 10-12, and DIVs 13-14, however, the amplitude returns to values observed by wild type samples by DIV 19. Interestingly, there is a relatively significant increase in the FWHM observed from DIVs 8-9 to DIVs 10-12 that result in relatively elevated values for $A_{FWHM}$. The values for $A_{FWHM}$ seen in BACHD start off relatively lower and gradually increase then, return to wildtype levels by DIVs 13-14. In general, the baseline area of emission activity, $A_B$, is elevated, which indicates higher basal levels of calcium in BACHD neurons. Interestingly, $A_B$ increases with a broader distribution from DIV 6 to DIV 7, which is thought to be the start of spontaneous calcium activity in vitro, and this increase is followed by a decline in amplitude on DIV 7. By DIVs 8-9, the value for $A_B$ appears lower than that observed for BACHD, however, the frequency declines in value by that range of DIVs as well. From DIV 7 to DIVs 8-9, the amplitude recovers to wild type values. The values for frequency are relatively lower than those observed in wildtype samples, with a sustained lower frequency found by DIVs 8-9. Median values for normalized rates are shown in **Figure 3.13** with error bars indicating the interquartile range. From **Figure 3.13**, all

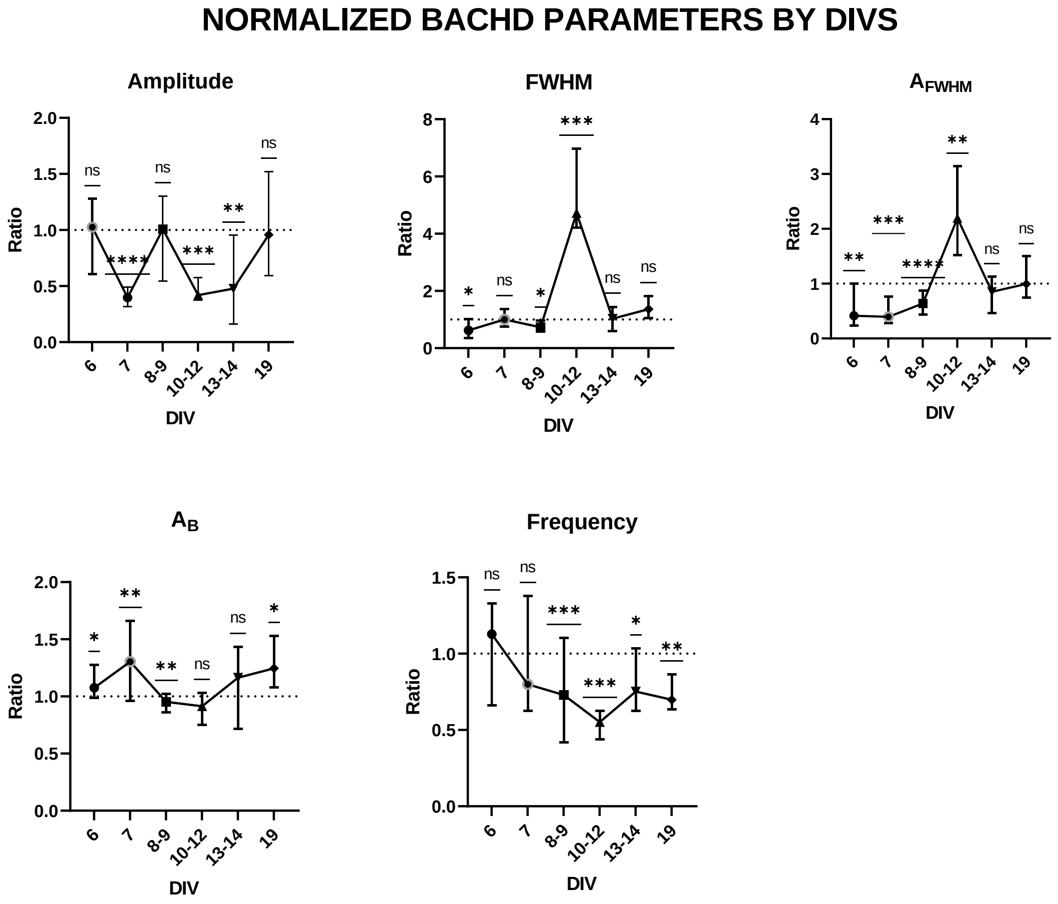

Figure 3.12 – Median BACHD parameter values normalized by average wild type values. Error bars indicate interquartile range and dashed line shows y = 1.0. Asterisks indicate statistical significance using one sample Wilcoxon test where (*) $P<0.05$, (**) $P<0.005$, (***) $P<0.001$, and (****) $P<0.0001$. Medians found for several trials across multiple wells and experimental dates. Populations are grouped by genotype where N = [15,16,37,13,20,9] for respective sets of DIVs with the exception of frequency on DIVs 8-9 where N = 39.

rate values appear relatively elevated on DIV 6 and follow a trend of decline up to DIVs 10-12. Interestingly, the rise and fall rates appear to follow similar trends.

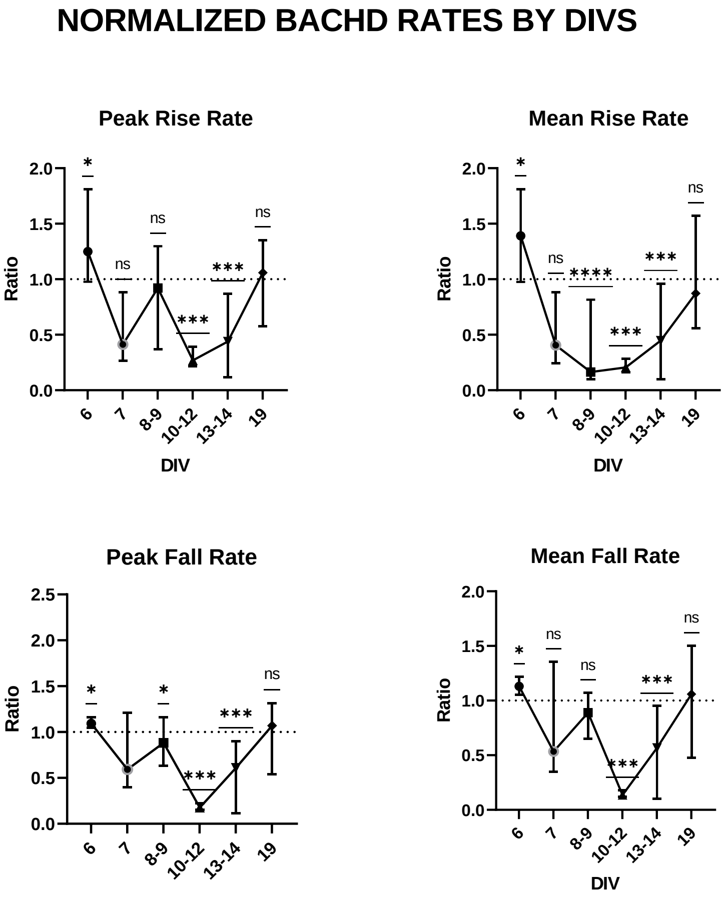

Figure 3.13 – Medians of BACHD rate values normalized by wild type values for DIV14 in respective subcellular regions. Data shown for wildtype (WT) and BACHD phenotypes in both the cytosol and nucleus. Dashed lines are shown for a value of 1.0. Error bars indicate the interquartile range. Asterisks indicate statistical significance using one sample Wilcoxon test where (*) $P<0.05$, (**) $P<0.005$, and (***) $P<0.001$. Populations are grouped by genotype where N = [13,17,38,13,22,9] for respective sets of DIVs.

### 3.4.2. Inhibition of Excitatory Activity in BACHD Cortical Neurons

Excitatory calcium activity was inhibited by the addition of 50 µM of D-AP5 and 10 µM NBQX. D-AP5 is a selective, competitive NMDA receptor antagonist that blocks induction of long term potentiation and NMDAR- media synaptic plasticity. NBQX is a selective competitive antagonist of AMPA receptors. The two inhibitors are incubated during the dye loading protocol and included in working concentrations within the imaging buffer throughout imaging. The inhibition condition for each genotype is denoted by (+) next to the genotype identifier otherwise the condition is no inhibition. **Figure 3.14** illustrates median values for parameters and rates on DIVs

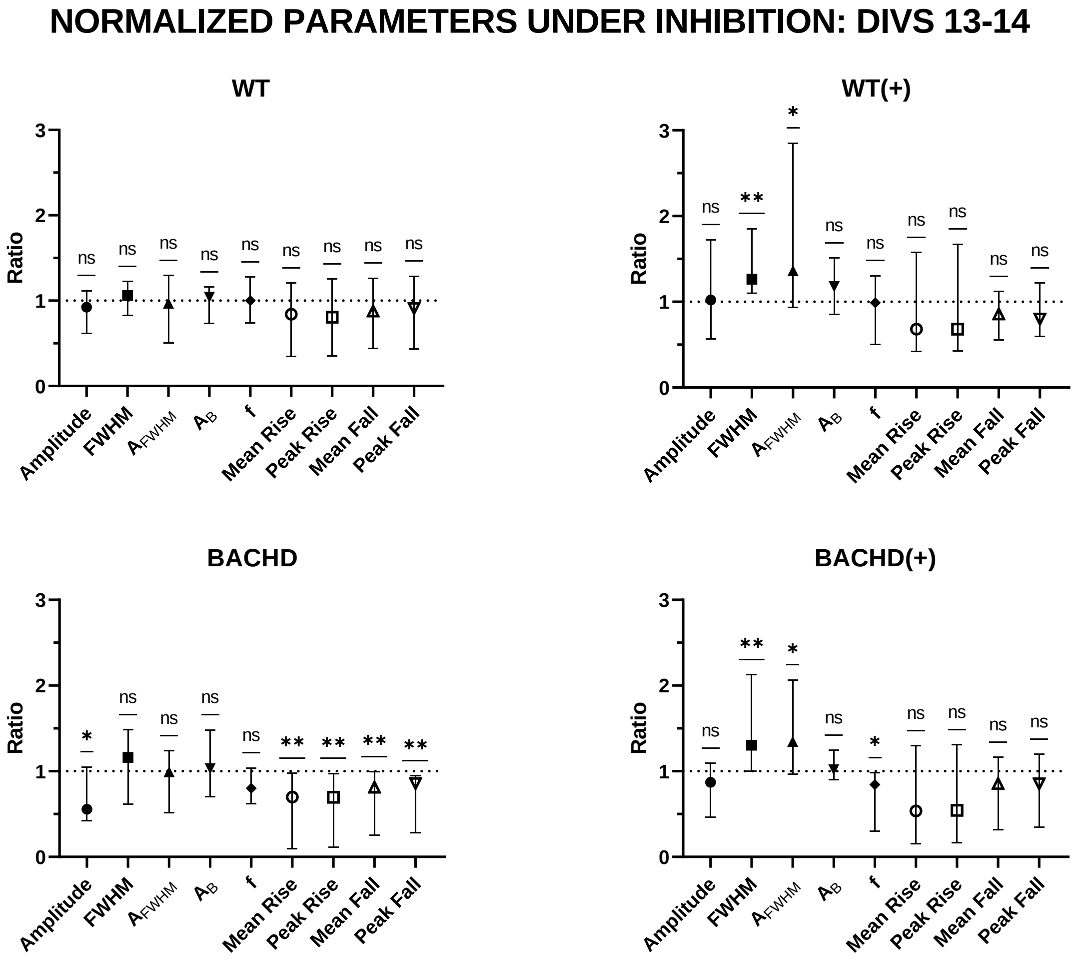

Figure 3.14 – Medians of parameter values under inhibition of 50 µM of D-AP5 and 10 µM NBQX normalized by negative control wild type values for DIVs 13-14 for respective subcellular regions. Data shown for wildtype (WT) and BACHD genotypes without inhibition (BACHD) both wildtype and BACHD genotypes with inhibition, WT(+) and BACHD(+), respectively. Dashed lines are shown for a value of 1.0. Error bars indicate interquartile mean with a band indicated median. Asterisks indicate statistical significance using one sample Wilcoxon test where (*) $P<0.5$ and (**) $P<0.005$. The trial number or sample size is N = [18,15, 18,15] for WT(-), WT(+), BACHD(-), and BACHD(+), respectively.

13-14 for non-inhibited wildtype (WT), inhibited wildtype (WT(+)), non-inhibited BACHD (BACHD), and inhibited BACHD (BACHD(+)) samples by normalized by parameter values for non-inhibited, control wild type samples. The results in **Figure 3.14** show a significant increase in values of FWHM and $A_{FWHM}$ observed in transient peaks for BACHD. In **Figure 3.14**, BACHD(+) values for amplitude recover to values observed for wild type. In addition, inhibition of excitatory activity rectifies differences

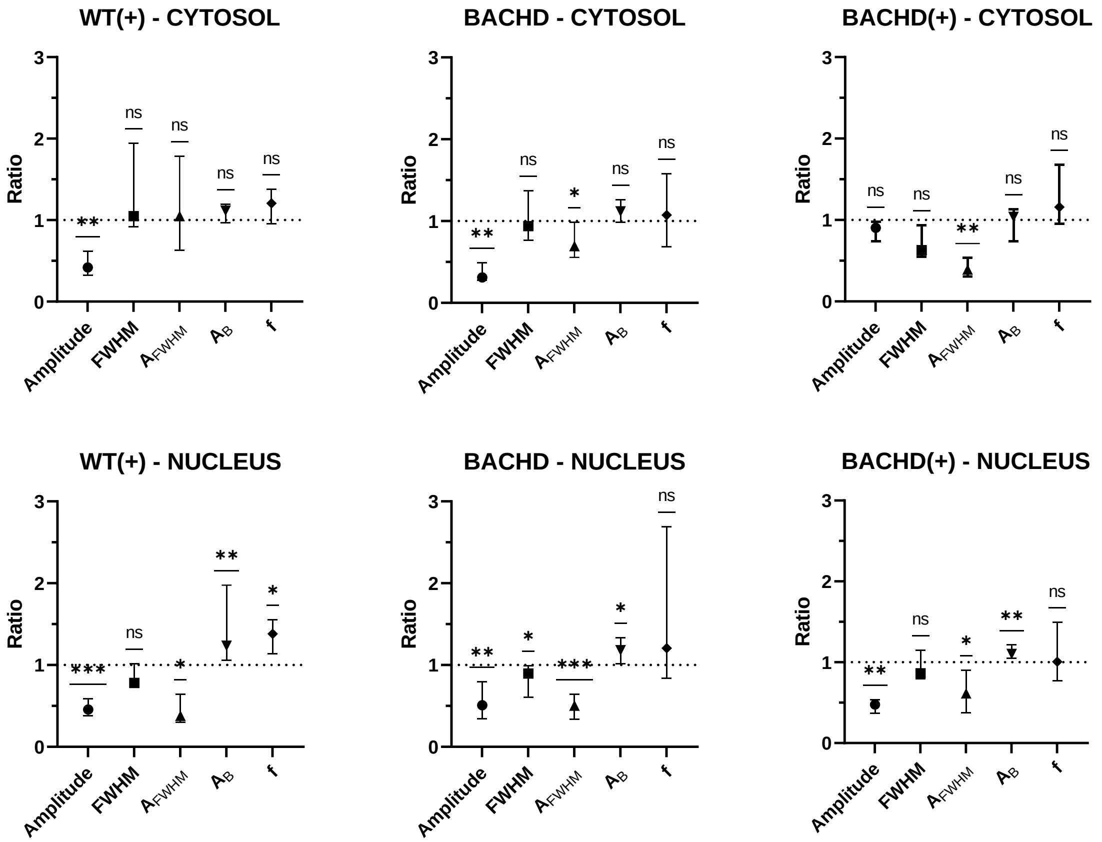

Figure 3.15 – Medians of parameter values normalized by wild type values for DIVS 13-14 in cytosol and nucleus. Data shown for wildtype (WT) and BACHD phenotypes under non-inhibited and inhibited conditions (+). Dashed lines are shown for a value of 1.0. Error bars indicate the interquartile range. Asterisks indicate statistical significance using one sample Wilcoxon test where (*) $P<0.05$, (**) $P<0.005$, and (***) $P<0.001$. The trial number or sample size for cytosol measurements is N = [8,9,10,8] for WT, WT(+), BACHD, and BACHD(+), respectively. For the nucleus measurements N= [7,12,11,9] for WT, WT(+), BACHD, and BACHD(+), respectively.

observed across all rate data while lowering values observed for frequency.

Normalized parameters are also shown by subcellular region for conditions of inhibition normalized by negative, wild type controls for the cytosol and nucleus in

**Figure 3.15**. The recovery in amplitude observed for BACHD(+) in **Figure 3.14** while observed in the cytosol is not observed in the nucleus. Furthermore, the median values for $A_B$ are elevated in the nucleus relative to the cytosol as compared to wild type values. This is somewhat expected since the depth of field during image acquisition could allow for scattered light from planes within the cytosolic region. This could slightly obscure results for the nucleus. Inhibition of excitatory activity appears to lower the intensity, duration, and rate values for both WT(+) and BACHD(+) in the nucleus as shown in **Figure 3.14 and Figure 3.15**. However, in general it seems that intracellular calcium activity does not vary dramatically in the nucleus as shown in **Figure 3.15**. Median values in **Figure 3.16** are normalized by positive, control parameter values found for wild type neurons under inhibition (WT(+)) order to highlight differences between the genotypes under inhibitory conditions. A Wilcoxon ranked-sign test demonstrates that all parameter values shown in **Figure 3.17**, except frequency, are not statistically different from values observed for wild type samples.

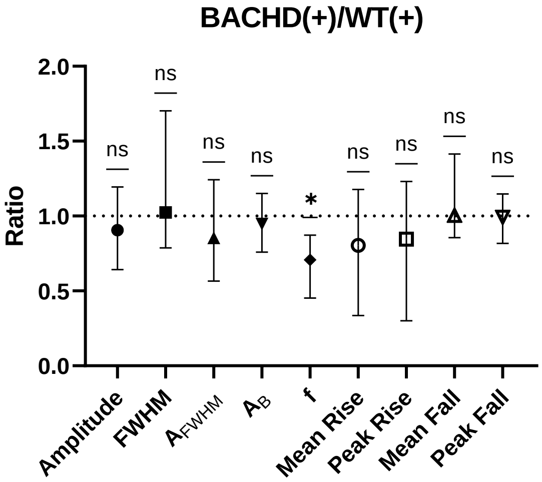

Figure 3.16 – Median of parameter and rate values under inhibition of 50 µM of D-AP5 and 10 µM NBQX normalized by positive, control wild type values for DIV13-14 for respective subcellular regions. Data shown for BACHD genotypes with inhibition. Dashed lines are shown for a value of 1.0. Error bars indicate interquartile range. Asterisks indicate statistical

## 3.5. Discussion

The spontaneous calcium activity of BACHD cortical neurons has yet to be fully characterized. The focus of this study is on the comparison of well-defined parameters associated with transient, peaks in calcium-dependent emissions intensity data. According to the results, spontaneous calcium activity in BACHD cortical neurons differ significantly from activity observed in wild type neurons. During 6 and 7 DIVs, increases in basal intracellular calcium accompany decreases in amplitude of observed transient peaks. By 8-9 DIVs, BACHD median parameter values return to observed wild type values of the average baseline area per unit time or $A_B$, however, while amplitude normalizes there are declines in relative values of frequency. It appears that BACHD cortical neurons reduce either the amplitude or the frequency of transient activity in response to elevated levels of intracellular calcium. On 8-9 and 10-12 DIVs, values of $A_B$ for BACHD decline below or recover to values observed for wild type. By 13-14

DIVs, there is a return to values observed by wild type samples except for median values of amplitude and frequency which are relatively lower. These changes in intracellular calcium are observed on DIV 7 and DIVs 10-12, which correspond to the onset of spontaneous activity and synaptic formation, respectively. Therefore, BACHD cortical neurons appear to gradually accumulate higher basal levels of intracellular calcium and are unable to mitigate cumulative contributions of intracellular calcium resulting from transient activity as compared to wild type samples. These differences seem exacerbated following the formation of synapses, which suggest that BACHD cortical neurons are less adaptable to the external, excitatory stimuli. In addition, there appears to be some delay in the ability for BACHD neurons to mitigate relative changes observed for the FWHM of transient activity, which translates as a lower effective buffering capacity for excess influx of calcium. The lower mean rise rates for calcium influx shown in **Figure 3.13** for 8-9, 10-12, and 13-14 DIVs coupled with lower relative values for amplitude and frequency suggest lower concentrations of intracellular calcium stores. Further evidence of this is provided from inhibition of excitatory activity, which rectifies most differences in the cytosol, but not in the nucleus. The cause of the depletion of intracellular calcium stores while unclear may result from sensitization of mechanisms supporting calcium-induced calcium release as evidenced by relatively higher values of FWHM and $A_{FWHM}$, or duration and calcium loads of transient activity in **Figure 3.14** for BACHD(+). The assumption being that neuronal intracellular calcium activity under excitatory inhibition is constrained to source transient activity from intracellular calcium stores. There appears to be a recovery in values by DIV 19 except for the sustained increase observed for basal intracellular calcium levels and reduced frequency. The sustained decrease in frequency and rising $A_B$ suggest that either there is an increase of influx of calcium from plasma membrane channels or an inability to sequester intracellular calcium stores from the cytosol. In any case, while activity appears to return to normalcy in BACHD samples the compromise of frequency and increase in basal calcium level are likely indicators of a metastable homeostatic equilibrium relative to wild type samples.

Overall, it seems that BACHD neurons recover from higher basal levels of intracellular calcium observed from DIV 6 to DIV 7 by some unclear mechanism. Recovery appears sustained until DIVs 10-12 when synaptic formation compels the BACHD neuron to return to lower amplitude values and sustain a narrower distribution of lower frequency values. The BACHD cortical neuron somewhat recovers by DIVs 13-14, however, this recovery is not sustained for frequency or $A_B$ by DIV 19. Thus, declines in frequency appear precede sustained elevations of basal intracellular calcium. Moreover, even though the values of frequency increase over time the relative difference from wild type values does not seem to change so the BACHD neuron begins to experience deficits over time. Inhibition of excitatory activity does not appear to correct this relative decline in frequency as compared to inhibited wild type samples in **Figure 3.16**. Moreover, it appears inhibition recapitulates trends observed in BACHD values for WT(+) samples in the nucleus. Early stages of HD are linked to striatal spiny neurons (SPNs), which are the first neurons to show dysfunction and loss, that suppress cortical excitation.[2] Sustained reductions in frequency of intracellular calcium activity may be suggestive of reduced responses to excitatory activity independent of inhibition from SPNs. Furthermore, inhibition of excitatory activity revealed lower frequencies of transient calcium events which is suggestive of lower levels of calcium-mediated intracellular activity.

Thus, parametrization and statistical analysis of Fluo 4 emission activity appears capable of resolving characteristic differences in the intracellular calcium activity of BACHD cortical neurons. Elevated basal levels of intracellular calcium is a hallmark of various chronic neurodegenerative disorders. However, further experiments are needed to fully characterize the cause of elevated basal levels of intracellular calcium encountered in BACHD cortical neurons. Further investigations are needed on the roles that the endoplasmic reticulum and the mitochondria may play regarding observed differences. The data here suggest that excitatory activity is linked to the onset of sustained elevations of basal intracellular calcium levels observed in BACHD cortical neurons, the mechanisms of which are unclear from calcium-imaging data alone. There are clear benefits to performing additional experiments at later DIVs to resolve differences between genotypes over time, which may further highlight sustained differences in parameters. It would be of significant interest to monitor gene expression in relation to changes in calcium-imaging data. Future experiments seeking to resolve differences in intracellular calcium may find more success at or after 13-14 DIVs where it BACHD neurons have reached a metastable calcium homeostasis in the absence of sustained environmental stress.

## 3.6. Acknowledgements

Chapter 3, in part, is co-authored with Weishan Li and Janna Sage. Figure 3.3 and Figure 3.4 were produced by Weishan Li. Weishan contributed greatly to the development of our GUI-based, Fluorescence Emissions Signal Analyzer (FESA) with

a particular focus on batching and ROI segmentation. Janna Sage aided in both the collection of calcium-imaging data, presented in the results throughout the chapter, and the routine maintenance of cultures used throughout these studies. The dissertation author was the primary author of this chapter.

## CHAPTER REFERENCES

1. L.A. Raymond, ”Striatal synaptic dysfunction and altered calcium regulation in Huntington disease,” *Biochemical and Biophysical Research Communications*, 2016.

2. M. Giacomello, R. Hudec, and R. Lopreiato, “Neuronal Ca2+ dyshomeostasis in Huntington disease,” *Prion*, vol. 7, no. 1, pp.76-84, 2013.

3. M. Suzuki, Y. Nagai, K. Wada, and T. Koike, “Biochemical and Biophysical Research Communications Calcium leak through ryanodine receptor is involved in neuronal death induced by mutant huntingtin,” *Biochemical and Biophysical Research Communications*, vol. 429, no.1-2, pp.18–23, 2012.

4. T.S. Tang, E. Slow, V. Lupu, I.G. Stavrovskaya, M. Sugimori, R. Lliáns, B.S. Kristal, M.R. Hayden, and L. Bezprozvanny, “Disturbed $Ca^{2+}$ signaling and apoptosis of medium spiny neurons in Huntington’s disease,” *PNAS*, vol. 102, no. 7, pp. 2602-2607, 2005.

5. Marco, S. et al., (2016). GluN3A promotes NMDA spiking by enhancing synaptic transmission in Huntington’s disease models. *Neurobiology of Disease*, 93, pp.47-56.

6. G. E. Hardingham and H. Bading, “Synaptic versus extrasynaptic NMDA receptor signalling: Implications for neurodegenerative disorders,” *Nat. Rev. Neurosci.*, vol. 11, no. 10, pp. 682–696, 2010.

7. G. Liot, D. Zala, P. Pala, G. Mottet, M. Piel, and F. Saudou, “Mutant Huntingtin Alters Retrograde Transport of TrkB Receptors in Striatal Dendrites,” *J. of Neuroscience*, vol. 33, no. 15, pp. 6298–6309, 2013.

8. P. H. Reddy and U. P. Shirendeb, “Mutant huntingtin, abnormal mitochondrial dynamics, defective axonal transport of mitochondria, and selective synaptic degeneration in Huntington’s disease,” *Biochim. Biophys. Acta – Mol. Basis Dis.*, vol. 1822, no. 2, pp. 101–110, 2012.

9. X. Zhao, X. Chen, E. Han, Y. Hu, P. Paik, Z. Ding, J. Overman, A.L. Lau, S.H. Shahmoradian, W. Chiu, L.M. Thompson, C. Wu, and W.C. Mobley, “TriC subunits

enhance BDNF axonal transport and rescue striatal atrophy in Huntington's disease," *Proc. Natl. Acad. Sci.*, vol. 113, no. 38, pp. E5655–E5664, 2016.

10. X. Zhang, J.Q. Wan, and X.P. Tong, "Potassium channel dysfunction in neurons and astrocytes in Huntington's disease," *CNS neuroscience & therapeutics*, vol. *24*, no. 4, pp. 311–318, 2018.

11. D. Sage and M. Unser, "Teaching Image-Processing Programming in Java," *IEEE Signal Processing Magazine*, vol. 20, no. 6, pp. 43-52, Nov. 2003.

12. C. Carmona and W. Li, "Fluorescence Emissions Signal Analyzer FESA." Github, February 10 2022, [Online]. Available: https://github.com/chris91191/Fluorescence-Emissions-Signal-Analyzer-FESA-/tree/main.

# Chapter 4: Modelling Traumatic Brain Injury Using Laser-Induced Shockwaves

## 4.1. Motivation

To further our understanding on the way that cells respond to shear stress, an optical system was developed that allows single cells to be studied in response to a sudden but short application of shear stress. This system can generate laser-induced shockwaves (LISs) at a specified time and location. A LIS can exert a shear stress between 0 - 50 kPa within a range that preserves cell viability and depends on the distance from the shockwave epicenter.[1] Our system includes a force measurement component that follows from the visualization of laser-induced bubble and shockwave dynamics. Ultimately, this system's capacity to quantitatively study shockwave dynamics permits the study of the spatiotemporal details occurring in cells responding to shockwave-induced shear stress. Thus, TBI can be further studied and subsequent results could reveal the molecular basis for neurodegeneration and potential therapeutic avenues for treatment.

## 4.2. Methods and Materials

### 4.2.1. Dye-Illuminated Imaging

For our studies, we utilize Robolase II (RBII): a fluorescence microscope system re-configured on an optical bench for simultaneous laser-induced shockwave generation and real-time cell imaging. The pump or ablation lasers used to generate shockwaves were either a Coherent Flare 532 nm, 100 Hz repetition rate system with a 2 ns pulse width and 450 $\mu$J pulse energy (Spectra-Physics, Mountain View, CA) or a Coherent FlareNx 1030 nm, pulse-gated with 1.4 ns pulse-width and 1 mJ energy.

Earlier studies utilized the Flare 532 nm laser in conjunction with a dye laser system that siphons power from the shockwave pump source in order to generate an illumination source that is concurrent with each shockwave event. Images obtained using the dye laser as an illumination source allowed for imaging of earlier shockwave dynamics, however, this system configuration depicted in **Figure 4.1** excludes the green channel of the visible light spectrum from data acquisitions during fluorescent microscopy experiments. For experiments conducted in the dye laser configuration, two-pulses are generated following the initialization of a

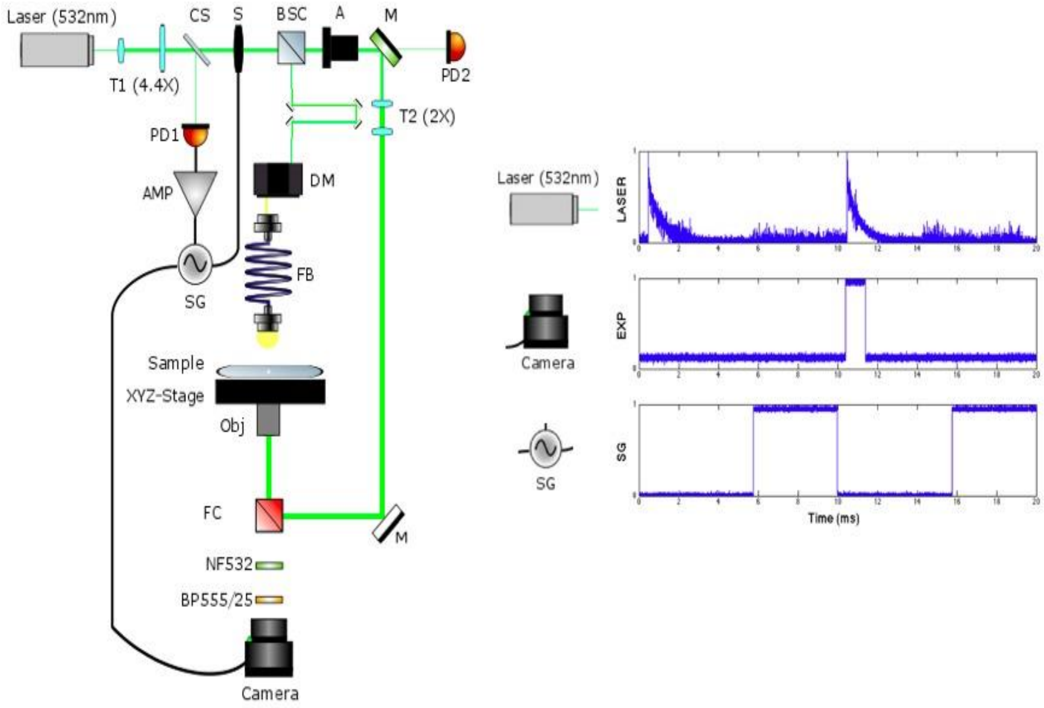

Figure 4.1 - System schematic (left) and timing schematic (right) for operation of Robolase II. The first laser pulse triggers the signal generator, which in turn triggers a camera exposure coincident with the second pulses

shockwave event by the 532 nm laser as depicted in **Figure 4.1**. While the second pulse is pumped into fluid media at the sample stage, the first is blocked by a shutter and detected by a photodiode in order to trigger a signal generator. The triggered signal generator produces a 5V square-wave pulse that opens a mechanical shutter (Vincent Assosciates, Rochester, NY) and, upon its fall, triggers an exposure on the Orca-Flash 4.0 V2 (C11440-22CU, Hamamatsu Photonics K.K., Japan). The imaging system is mounted on a Zeiss Axiovert 200M microscope (Carl Zeiss, Thornwood, NY). The source of illumination used to visualize bubble-cavitation events is produced via an optically-coupled dye laser module (DUO-210, Laser Innovations, Santa Paula, CA). The dye laser module utilizes 532 nm laser light as an excitation source for the fluorescent dye (Rhodamine 590, Exciton, Dayton, OH), which has a emissions peak measured at 557 nm. The dye used was chosen for its rapid decay rate[2] and high quantum-yield in order to maximize the intensity of light produced from short pulses of excitation light while minimizing the duration of the illumination pulse. The fluorescent dye is dissolved in methanol and relative

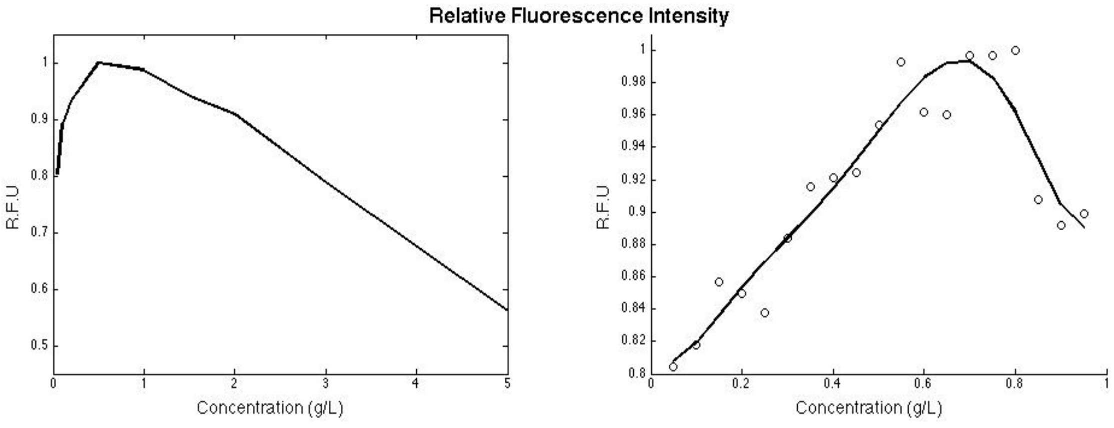

Figure 4.2 - Relative fluorescence intensity is measured at 557 nm and compared using normalized units (R.F.U) across varied concentrations of Rhodamine Cl prepared in methanol. R.F.U for concentrations ranging from 0.05 g/L to 5 g/L is plotted on the left. A scatter plot of R.F.U for concentrations ranging from 0.05 g/L to 0.95 g/L is shown to the right with a polynomial fitted trendline. Peak emissions intensity is measured at 0.8 g/L.

fluorescence intensities were measured at various concentrations in order to optimize emissions intensity. Relative fluorescence intensities at 557 nm for various dye concentrations are shown in **Figure 4.2**. The dye laser light is delivered from the output of the module through the microscope condenser to illuminate the sample of interest via a fiber optic bundle. Delays of the dye laser illumination source relative to the shockwave pump source is adjusted by varying the beam path length using a translatable mirror-rail system. The light produced by plasma formation, which precedes bubble cavitation, emits a broad spectrum of bright light that competes with our dye laser illumination source. Therefore, a bandpass filter (ET555/25, Chroma, Bellows Falls, VT) selected for the transmission of the dye laser light is utilized to minimize the contributions of light from plasma formation in the final image. In this manner, we acquire time-integrated images of laser-induced bubble cavitation coincident with our illumination source.

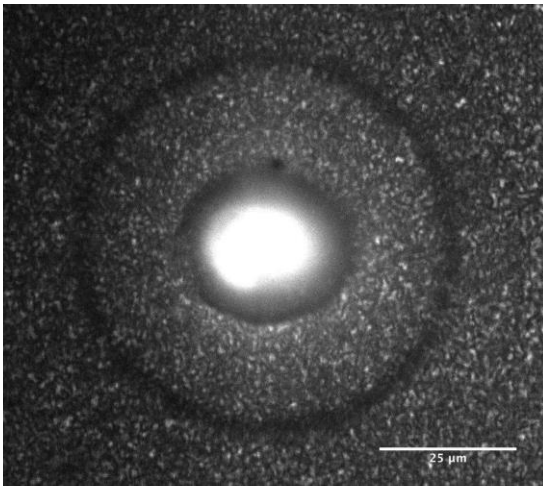

Figure 4.3 - Time-integrated, bright-field image of a laser-induced shockwave using a 63X/1.4 oil immersion objective on RBII.

The shockwave generation system in the dye laser configuration has been able to resolve nanosecond scale events that are characteristic of early LIS dynamics. The illumination intensity as measured at the dye laser module output indicates a conversion efficiency of 55%. The intensity measured at the sample stage reflects an effective conversion efficiency of 28.6% from a flux of 123.4 $\mu$W/cm2. The uncertainty between the coincidence of an initiated camera exposure and the shockwave generating pulse is 147 $\mu$s and is determined by measuring the uncertainty associated with the delay time between each aforementioned event across ten trials. In **Figure 4.3**, the time-integrated image captured using RBII reveals early plasma formation evident by the bright, central region and bubble cavitation indicated by the dark, circular ring surrounding the plasma. Approximately 30 $\mu$m radially outwards from the epicenter of the shockwave shown in **Figure 4.3** there is a dark ring which indicates the position of the wavefront of a shockwave generated by bubble cavitation.

### 4.2.2. High-Speed Imaging

Later studies utilized a high-speed camera (FASTCAM-1024PCI, Photron USA, INC., San Diego, CA) in order to capture the bubble dynamics which followed from laser-induced plasma generation. Software distributed with the FASTCAM by Photron USA, INC. was primarily utilized to acquire high-speed images using the FASTCAM and a computer workstation. The inclusion of the high-speed camera necessitated changes to RBII that are detailed in **Figure 4.4**. While the FASTCAM-1024PCI has a maximum framerate of 1,000 fps at its full resolution of 1024 x 1024 pixels, it can record at a maximum frame-rate of 109.5 kfps with a resolution of 128 x 16 pixels. Additionally, the FASTCAM-1024PCI has an electronic shutter with a minimum exposure time of approximately 1.5 µs. Under a magnification of 20X, recording at 109.5 kfps would result in a field of view of approximately 109 µm x 14 µm. In order to accurately model the resultant forces generated by LISs, it is necessary to capture the full expansion of a laser-induced bubble, however, maximum bubble sizes in this system approach several hundreds of microns.

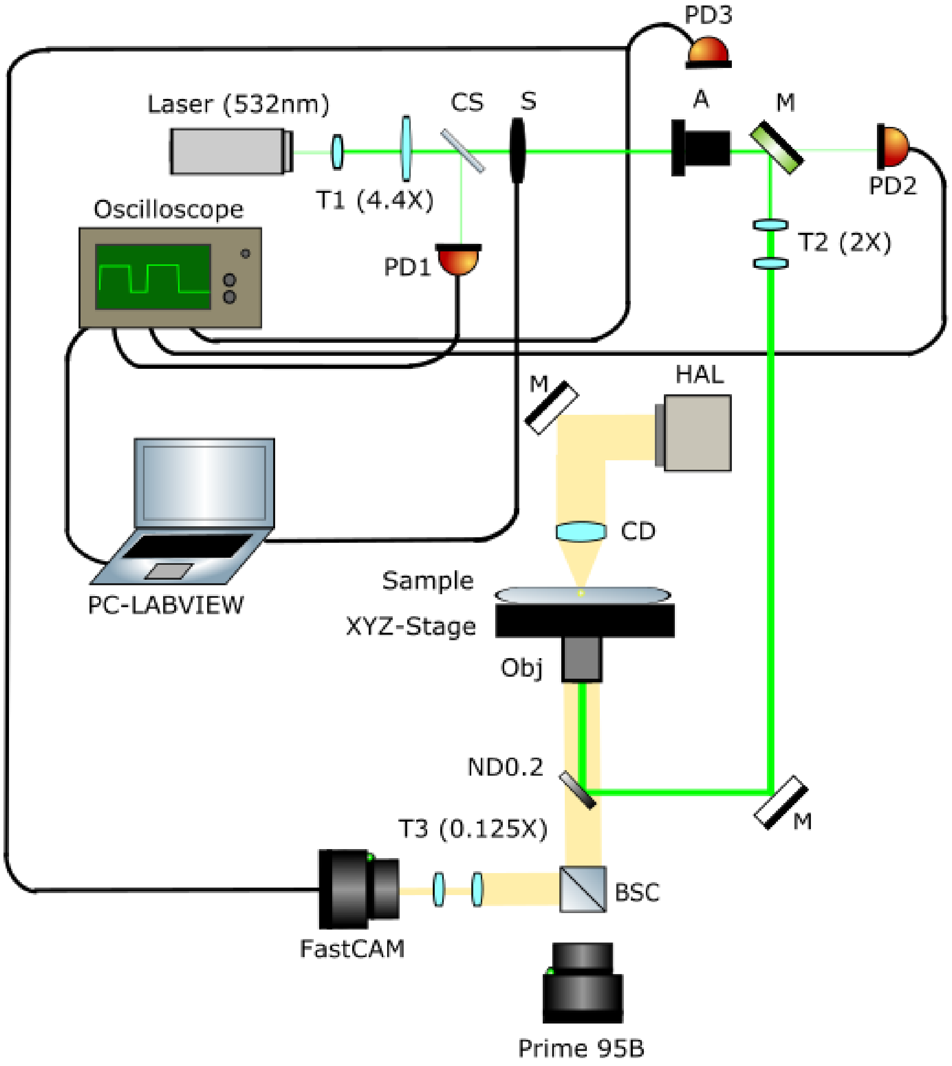

Figure 4.4 – Schematic of RBII following incorporation of FASTCAM-1024PCI, high-speed camera. Key changes include illumination of bubble dynamics via halogen lamp and demagnification of image on high-speed camera sensor.

Therefore, an optical train leading from the microscope to the high-speed camera was configured to de-magnify the image by 0.125X and to expand the field of view on the FASTCAM-1024PCI sensor. Characterization studies of laser-induced bubble cavitation are performed with both a 20X/0.75 Fluar, dry objective (Carl Zeiss, Thornwood, NY, item no. 440145-9901-000) and a 40X/1.4 EC Plan-Neofluar, oil objective (Carl Zeiss, Thornwood, NY, item no.420462-9900-000).

### 4.2.3. Image Analysis

Sequences of time-series frames acquired using the FASTCAM were analyzed with MATLAB(v.2020b) and ImageJ. Using ImageJ, the diameter of the bubble in individual images were manually measured. For bubbles that exceeded the field-of-view a fixed center coordinate was determined and used to measure radius. Measurements involving ImageJ were reserved for sets of images which had more accurate timing data available and smaller population sets that generated inconsistent results while using MATLAB.

For automated measurement, the image of a bubble on our sensor results from the refraction of light out of the image plane, it becomes more intuitive to calculate changes of image complements. The image complement transforms the image such that grayscale values of an image are reversed by replacing original pixel values with their respective differences from the maximum pixel depth. Afterwards, the difference between image complements of a pre-LIS frame and post-LIS frame is calculated and normalized. Following image subtraction and normalization, the image is then passed through an edge detection function, *edge(…)*, in MATLAB. The edge detection function utilizes the Canny method, which finds edges by looking for local maxima of the gradient of the image, while using two thresholds to find both weak and strong edges. The advantage of using the Canny method is that it is less likely to be fooled by noise that result from the low-resolution of the images being analyzed. Lastly, a set of binarized images are generated from the processed images and analyzed separately.

Following the processing of raw images, several measurements are performed on individual sets of time-series of the bubble expansion and collapse. Radii are calculated from the center on left and right sides of the center coordinate and averaged in order to determine an effective bubble radius for a single frame. In this method, binarized images are used to determine coordinates relative to a user-specified epicenter at which a value changes from 1 to 0. In practice, this method alone is prone to error because of refraction occurring during the expansion of a bubble that leads to an uneven intensity profile during analysis. A few methods are employed in order to mitigate errors resulting from imaging including analysis of the linear intensity profile that compares two maxima on opposing sides of the bubbles' central, vertical axis of symmetry. The result is used in conjunction with a Gaussian fitting in order to estimate the radii of bubbles by approximating the diameter as twice the full-width at half maximum (FWHM), which encompasses 95.5% of the normal distribution. Additional values, one and three times the FWHM, or multiples of the FWHM are used to generate errors about the measured value. Maximum bounds of the bubble for determined for an image by find maxima along the resulting linear intensity profile of the edge detection function, *edge(…)*. An example of analysis results are shown in **Figure 4.5**, which depicts a single, time-series acquisition of bubble expansion and collapse with respective times labelled and t=0 indicating the time a shockwave pump pulse reaches the focal plane. The resultant

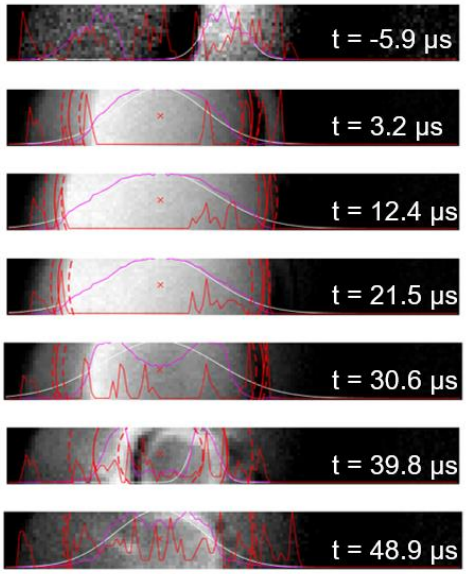

Figure 4.5 – Time-series of bubble expansion and collapse. The measured radius of a circle fitting a bubble (red, solid outline) with its respective center marked by X and the standard error of the mean are shown (red, dashed outline). The gaussian distribution labelled by a (white, solid line) is shown and compared with the intersection of intensity profiles from both sides of the vertical axes of symmetry through center coordinate (purple, solid line). The profile intensity resulting from the edge detection of each image is shown as well (red, solid line).

average of several measurements of bubble radius is depicted in **Figure 4.5** by outlining a circle (red, solid outline) of the measured radius with center (X) and, respective, standard error of the mean (red, dashed outline). Linear intensity profiles are also shown in **Figure 4.5** scaled to the image. The product of normalized, linear intensity profiles on opposing sides of the central, vertical axis of symmetry (purple, solid line) is shown for each image in **Figure 4.5**. In addition, the gaussian fit used to approximate bubble diameter (white, solid line) and the linear intensity profile found using the edge detection function (red, solid line) are also shown in **Figure 4.5**.

In a further attempt to improve the accuracy of bubble radii measurements, measurements of bubble radii for individual frames across several sets of acquisitions were compared and averaged for similar timepoints along the period of bubble growth and collapse. The result assumes that independent sets of time-series are alike with regards to the relative timing of the shockwave event and the start of camera acquisition. Considering that the period of bubble growth and collapse is expected to range in the tens of microseconds, it is clear that variations of microsecond could significantly impact the reliability of the early, explosive bubble growth. It then becomes desirable to understand the timing accuracy and the limitations impressed upon the system by hardware and or software to reduce systematic error.

## 4.3. Hardware and Timing Considerations

Despite the stochastic nature of generating laser-induced bubbles, one can reliably generate shockwave events when utilizing a pump pulse with power values at values greater at threshold value, which is defined by a 50% chance of catalyzing bubble growth. These threshold values vary between different laser systems and objectives and are, generally, determined empirically. By counting the number of shockwave events that occur over several sets of trials, we determine the probability that a shockwave event might occur for a given laser source, power level, and objective. The probability often takes on a sigmoidal curve shown on **Figure 4.6.** By choosing a laser power that remains well above threshold power values, one can generate shockwave events with high reliability. Relevant threshold values are shown in **Table 4.1**.

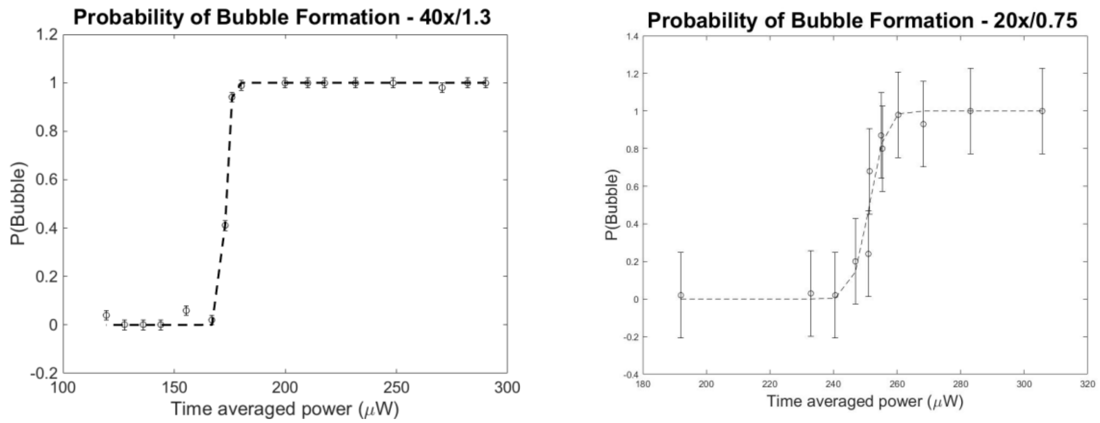

Figure 4.6 – Probability for bubble generation vs. time average power values for a 532 nm, ns-pulsed laser while using two different objectives (left and right). Threshold values are determined to be 176 µW for the 40x/1.3 objective and 251.34 µW for the 20x/0.75 objective.

Table 4.1 – Power threshold is defined as level at which shockwave generation has a 50% probability of success. *Calculated based on repetition rate of INDI-20 laser used in study.[1]

| **Magnification** | **N.A.** | **Pulse-width (ns)** | **Energy Threshold ($\mu$J)** | **Power Threshold ($\mu$W)** |
|---|---|---|---|---|
| 20x | 0.75 | 1.7 | 2.51 | 251.34 |
| 40x | 1.3 | 1.7 | 1.73 | 173.3 |
| 40x | 0.8 | 6 | 8 | *160 |

Initially, it was unclear whether the timing of events leading to the growth and collapse of a bubble would vary at power values above the threshold. Images captured using dye illumination have all acquisitions coupled to the timing of the shockwave pump pulse thus, variations in early bubble sizes as captured by dye illumination would be inherent to natural phenomena and not to any hardware. Measurements of early bubble dynamics resulting for different time averaged powers are shown in **Figure 4.7**. While there appears to be a linear relationship between time averaged power and measurements of bubble radii as well as plasma, the average, measured radius does not vary dramatically at this time point. Interestingly, the non-linear behavior of the shockwave radii represented by green and purple on **Figure 4.7** is suggestive evidence for the early, non-linear growth of the shockwave velocity since, minor changes in bubble size result in greater changes in measured shockwave radii. Using linear

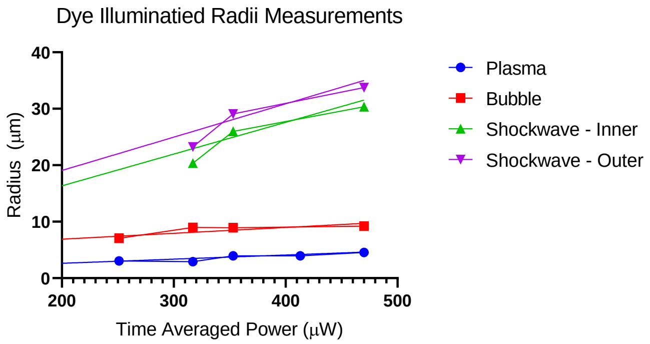

Figure 4.7 – Radii measurements for various time averaged powers using a 40x/1.3 Zeiss objective were taken at a fixed time point relative to shockwave pump laser arrival at the sample stage focal plane and coincident with dye illumination, $t_{dye}$ = 11.1 ± 0.1 ns. Each point is an average value of several trials. Plasma radius (blue-circle) is a measure along the central, bright, intense region seen during early bubble formation. Bubble size (red-square) is measured from center to edge of darkened region. The shockwave is visible as a darkened ring around the expanding bubble so, a radius is measured from the center to the inner ring (green-triangle) and again to the outer ring (purple, inverted-triangle).

regression of dye-illuminated radii measurements in **Figure 4.7** approximations of bubble size coincident with the time of dye-illumination or $t_{dye}$= 11.1 ± 0.1 ns are determined. The measurement for plasma radius is defined as the full-width half maximum of a Gaussian fit on its intensity profile and assumed to be the maximum plasma length since, the sensor is saturated during a single frame acquisition. Furthermore, for modelling purposes it became convenient to assume the maximum plasma length is equivalent to the initial bubble size.

For experiments utilizing the high-speed camera and the 532 nm laser source, the timing accuracy was limited by hardware used to trigger a laser event and, subsequently, an image acquisition. In this configuration an average delay, $t_{delay}$ = 2.2 μs, from the time a shockwave event is generated to the first frame acquisition using the FASTCAM is measured with a standard deviation of about 400 ns. However, the FASTCAM awaits a trigger it continuously acquires images using an independent clock at a maximum framerate of 109.5 kHz. Since, the shutter speed is set to 1/657,000 s the effective exposure time of the sensor is approximately 1.52 µs. There appears to be enough variation that some pairs of time-series appear offset in time regarding the anticipated growth and collapse of the visualized bubble. The generation of these time-series offsets are also sensitive to the timing of the acquisition trigger moreover, when the trigger arrives during an exposure before it is transmitted to ram there is a sensor reset that is approximately 3.7 µs. Several trials are inspected in order to avoid averaging bubble radii measurements from non-matching time-points observed in offsets. Assuming the same uncertainty for time-series sets that are offset by the sensor reset time, then when identified one can still utilize measurements from these images for fitting bubble dynamics data as well. Later trails utilizing a 20X/0.75 objective employed measurements of the delay of frame acquisitions relative to the shockwave pump pulse using an oscilloscope, TEK580 (Alphatek). At least two measurements of delay time were gathered during a shockwave generation event and later averaged, which produced values utilized in further analysis with standard errors of about 22ns. The bubble radii data for the 20X/0.75 objective at 1.03 times threshold energy is shown in **Figure 4.8** with corrections to temporal values found from measurements of delay.

## 4.4. Results

### 4.4.1. Modelling of Bubble Dynamics

The shear force generated by laser-induced shockwaves is characterized by the bubble dynamics and can be measured by modelling the explosive growth and collapse of bubbles. Measurements of the radii of expanding and contracting bubbles at specific timepoints relative to laser stimulation are averaged and fitted using the Rayleigh-Plesset equation for bubble expansion and collapse.

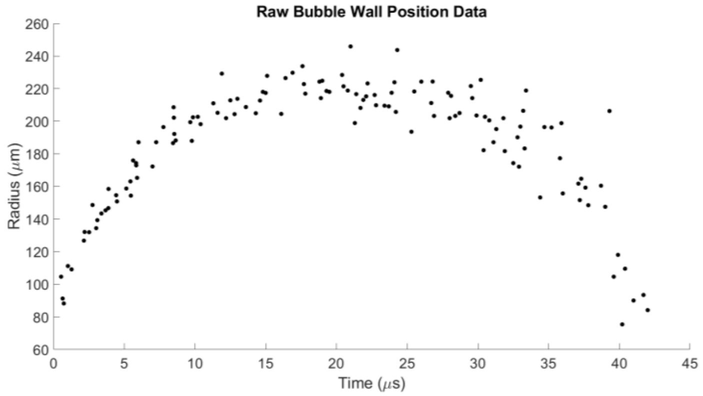

Figure 4.8 – Bubble radius measurements using 20X/0.75 objective with temporal values of respective bubble radii sizes corrected for using measured delay between initial frame acquisition and shockwave pump pulse trigger. Values with non-unique timepoints were averaged.

Measurements for bubble radii over time are shown for a 40X/1.3 objective at varied time average powers in **Figure 4.9a** and maximum bubble radii across a range of power levels are shown in **Figure 4.9b**. The measurements in **Figure 4.9a** is are average radii of several timepoints which share an average time delay that carries with it an uncertainty.

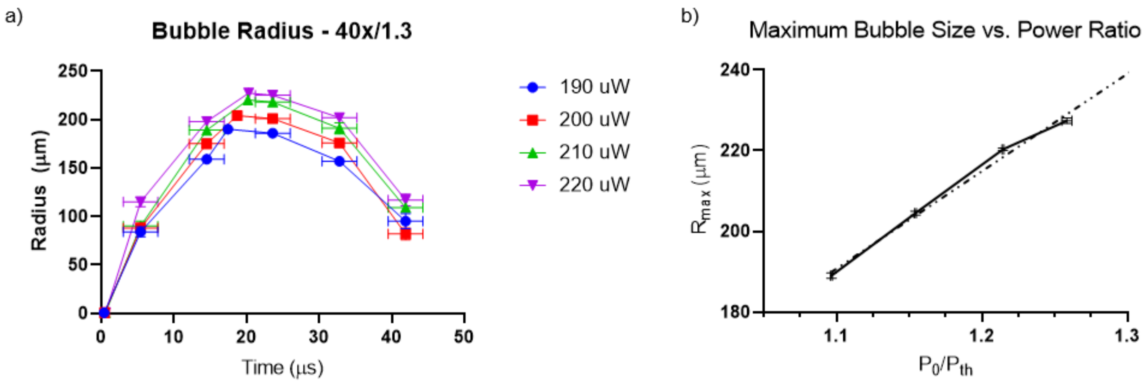

Figure 4.9 – a) Bubble radius measurements over time where t=0 is time of laser stimulation for different time averaged powers. b) Maximum bubble radius measurements fitted using linear regression across several ratios of incident, time averaged power over threshold power for plasma formation with 95% confidence intervals contained within the dotted lines.

In order to fully characterize the shear stress generated by LISs, it is important to accurately model the bubble dynamics. For our purposes, we will be utilizing the Rayleigh-Plesset equation for bubble growth and collapse:[3]

$$\frac{p_B(t) - p_\infty(t)}{\rho_L} = R\ddot{R} + \frac{3}{2}\dot{R}^2 + \frac{4\nu_L \dot{R}}{R} + \frac{2S}{\rho_L R} \qquad (4.0)$$

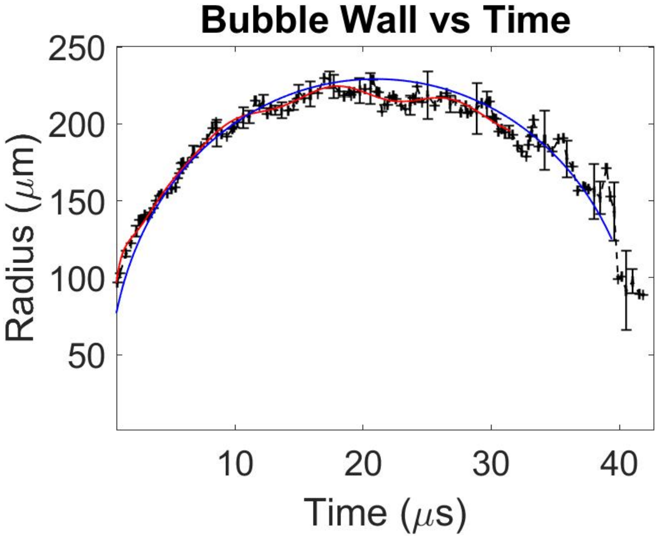

Figure 4.10 – Bubble wall radial position for bubble imaging data collected using 20X/0.75 objective and laser pulse energy of 1.03x plasma formation threshold (260uW). Black markers show moving average of experimentally acquired datapoints with a Fourier series fit (red). The Rayleigh-Plesset equation is fitted and shown over data (blue).

The above equation is modelled and fitted for bubble wall radial data in **Figure 4.10.** The bubble wall data shown in **Figure 4.10** was collected using a 20x/0.75 objective and our ns-pulsed, 532 nm source. The results for velocity of the bubble wall front from bubble data in **Figure 4.10** are shown in **Figure 4.11**. Here, constants are assumed for liquid density, dynamic viscosity, and surface tension are given by $\rho_L$= 993 kg/m$^3$, $\nu_L$= 1.002 µPa·s, and $S$= 0.0725 N/m, respectively. The pressure of gas in the expanding bubble and the ambient pressure in media substantially far away from the epicenter are given by $p_B(t)$ and $p_\infty(t)$, respectively. Given $p_\infty(t)$ this equation can be solved to find $R$ provided that $p_B(t)$ is known. Generally, $p_\infty(t)$ is constant but can represent some time-varying acoustic signal. Consideration of bubble contents are then necessary. Generally, it is assumed that a bubble contains some quantity of contaminant gas with partial pressure $p_{G_0}$ at reference size, $R_0$, and temperature, $T_\infty$. If there is no appreciable mass transfer of gas to or from the liquid then,

$$p_B(t) = p_v(T_B) + p_{G_0}\left(\frac{T_B}{T_\infty}\right)\left(\frac{R_0}{R}\right)^3 \qquad (4.1)$$

It still remains to determine $T_B(t)$, however, this is not always the case since, under some conditions the difference between the unknown $T_B$ and known $T_\infty$ is negligible. There are circumstances in which the temperature difference, $(T_{\boldsymbol{B}}(t) - T_\infty)$, is important and the effects governed by this difference dominate the bubble dynamics. The temperature difference would result in a different vapor pressure, $p_v(T_B)$, than would occur in the absence of such effects. Therefore, it becomes instructive to substitute Equation (4.1) into (4.0) and re-write the Rayleigh-Plesset equation in a more general form: [3]

$$\frac{p_v(T_\infty) - p_\infty(t)}{\rho_L} + \frac{p_v(T_B) - p_v(T_\infty)}{\rho_L} + \frac{p_{G_0}}{\rho_L}\left(\frac{T_B}{T_\infty}\right)\left(\frac{R_0}{R}\right)^3$$

$$= R\ddot{R} + \frac{3}{2}\dot{R}^2 + \frac{4\nu_L\dot{R}}{R} + \frac{2S}{\rho_L R} \qquad (4.2)$$

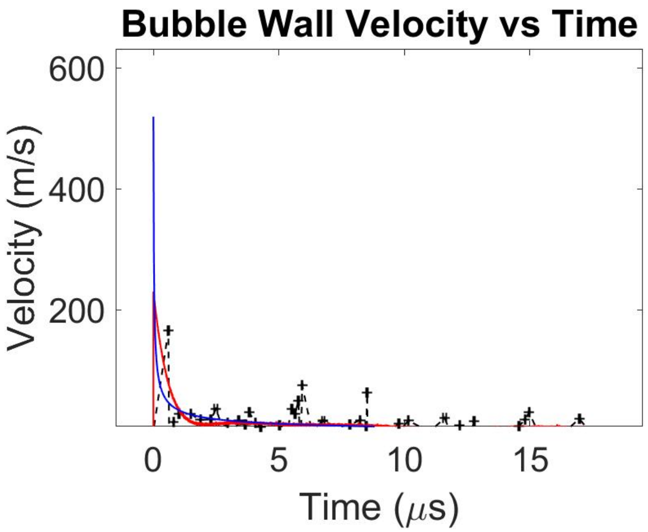

Figure 4.11 – Bubble wall front velocity for bubble imaging data collected using 20X/0.75 objective and laser pulse energy of 1.03x plasma formation threshold (260uW). Black markers and the red, fit line are values for velocity resulting from numerical differentiation of a moving average and a Fourier series fit (red) to bubble radial position data, respectively, from Figure 5.9. The results for velocity from the Rayleigh-Plesset equation is shown over data (blue).

The first term in Equation (4.2) is the instantaneous tension or driving term determined by conditions far from the bubble. The second term, will be referred to as the thermal term. The behavior of the gas in the bubble is assumed polytropic such that,

$$p_G = p_{G_0}\left(\frac{R_0}{R}\right)^{3k} \qquad (4.3)$$

In the case of laser-induced shockwaves, the window of time leading to plasma formation and subsequent bubble expansion is too small to allow for thermal diffusion.[4] The thermodynamic process is considered to be adiabatic and in our case $k = \gamma$, the adiabatic index for a diatomic gas. Furthermore, the temperature in the liquid is assumed uniform throughout bubble expansion and collapse thus, the thermal term in Equation (4.2) becomes negligible. With the above assumptions, the Rayleigh-Plesset equation becomes:[3]

$$\frac{p_v(T_\infty) - p_\infty(t)}{\rho_L} + \frac{p_{G_0}}{\rho_L}\left(\frac{R_0}{R}\right)^{3\gamma} = R\ddot{R} + \frac{3}{2}\dot{R}^2 + \frac{4\nu_L\dot{R}}{R} + \frac{2S}{\rho_L R} \quad (4.4)$$

For initial conditions, a microbubble of radius, $R_0$, with initial velocity,$v_0$, has an internal gas pressure of $p_{G_0} = p_\infty(0) - p_v(T_\infty) + \frac{2S}{R_0} + \frac{4\nu_L v_0}{R_0}$. In the case of a laser-induced shockwave, a bubble reaches equilibrium at its maximum bubble size, $R_m$. Moreover, several  Lastly, solving Equation (4.4) in terms of $\ddot{R}(t)$ yields:

$$\ddot{R} = \frac{1}{R}\left(\frac{p_v(T_\infty) - p_\infty(t)}{\rho_L} + \frac{p_{G_0}}{\rho_L}\left(\frac{R_0}{R}\right)^{3\gamma} - \frac{3\dot{R}^2}{2} - \frac{4\nu_L\dot{R}}{R} - \frac{2S}{\rho_L R}\right) \quad (4.6)$$

Given the appropriate initial conditions, a numerical solution can be obtained to $R(t)$  using Equation (4.6). In this case, a few assumptions about initial conditions are made: (1) there is no bubble present prior to delivery of a laser pulse thus, a sudden change of pressure $p_{G_0}$occurs at the time of plasma formation, $t = t_{plasma}$, (2) the initial bubble size, $R_0$, is at least the size of the maximum plasma axial length, and (3) the initial velocity of the bubble, $v_0$, is at least the average velocity of the plasma front. These approximations for initial conditions are subsequently optimized using the method of least squares to fit numerical solutions to Equation(4.4) to experimental data. For a laser pulse with a gaussian temporal profile,

$$I_n(t) = I_0 \exp\left[\frac{-2(t_0 - t)^2}{\tau^2}\right] \quad (4.7)$$

Each pulse was energy $E_n$ with peak irradiance $I_0$. Under the assumption that there exists a threshold laser irradiance at which plasma is formed, $I_{th}$, then

Equation (1.7) is solved for $t_{plasma}$; the time at which a lser pulse with peak irradiance, $I_n$, reaches the threshold irradiance for plasma formation: $I_n(t_n) = I_{th}$ . [5] Furthermore, in a Gaussian pulse shape the total energy and peak irradiance have a linear relation, implying that; $\beta = \frac{I_{th}}{I_{0,n}} = \frac{E_{th}}{E_n}$ .[5]

$$t_{plasma} = t_0 - \sqrt{Log\left(\frac{I_{0,n}}{I_{th}}\right)} = t_0 - \sqrt{Log\left(\frac{E_{0,n}}{E_{th}}\right)} \quad (4.8)$$

Here, the threshold energy is empirically determined while the initial pulse energy is set by the experimenter. In our model, $t_0$ is determined beforehand and the second term of Equation (4.8) is assumed $t_{plasma}$ for values of $E_{0,n} \geq E_{th}$, otherwise, when $E_{0,n} < E_{th}$ then $t_{plasma} = \frac{\tau}{2}$. An approximation of the plasma radius at time $t_{plasma}$ is determined finding the maximum plasma length, $z_{max}$. Assuming the breakdown threshold is independent of beam diameter and the threshold is constant in time, for a Gaussian shape and beam profile, Docchio derived $z_{max} = z_R\sqrt{\beta - 1}$, where $z_R = \frac{\pi\omega_0^2}{\lambda}$ is the Rayleigh range and $\omega_0$ is the radius of the beam, focal spot.[6] Moreover, an approximate, average initial velocity, $v_0$, can be obtained for the expansion rate of the plasma front by utilizing the pulse-width, $\tau$, of the pump laser such that $v_0 = \frac{z_{max}}{\tau}$. [6] It is evident that non-zero, real values of $z_{max}$ are only found when $E_{0,n} \geq E_{th}$. Thus, for modelling purposes when $E_{0,n} < E_{th}$, $z_{max} = z_R$ and $v_0 = \frac{2z_{max}}{\tau}$.

Additional calculations are made to determine the maximum potential energy of a bubble by calculating,[7]

$$E_b = \frac{4\pi}{3}(p_\infty - p_v)R_{max}^3 \ (4.9)$$

Subsequently, the efficiency of laser-induced bubble cavitation can be found from $\eta = \frac{E_b}{E_{0,n}}$ .

### 4.4.2. Calculation of Shear Stress

Imaging of bubble dynamics provides a means of quantifying the spatial and temporal evolution of both the radial position $R_B(t)$ and the velocity $V_B(t)$ of the bubble wall. A similar analysis of wall shear stresses on the surface of red blood cells resulting from shock-induced and bubble-induced flows in a shockwave lithotripsy[8] is performed here. Conservation of mass for an incompressible fluid provides the following relationship between the external fluid velocity and the bubble dynamics:

$$V_\infty(r,t) = V_B(t)\left[\frac{R_B(t)}{r}\right]^2 \quad (4.10)$$

Equation (4.10) is only valid at locations sufficiently removed from the boundary presented by the underlying glass coverslip since, the standard no-slip boundary applies at the boundary ($z = 0$). Therefore, there is a thin fluid layer proximal to the boundary in which the fluid velocity varies as a function of both $z$ and $t$. In order to examine the velocity distribution within this boundary layer, we first consider Stokes' first problem for impulsively started flow along a solid boundary with constant fluid velocity $V_\infty$. The momentum equation in x-direction or the direction of flow is a diffusion equation given by:

$$\frac{dv_x}{dt} = \mu \frac{d^2 v_x}{dz^2} \quad (4.11)$$

Where the z-direction is normal to the boundary layer and $\mu$ is the kinematic viscosity. Equation(4.11) is subject to boundary conditions:

$$v_x(y, 0) = V_\infty \quad (y > 0)$$

$$v_x(0, t) = 0 \quad (t > 0)$$

The solution to the above equation can be obtained by using similarity variables and can be found in any standard textbook. The solution is given by:

$$v_x(z, t) = V_\infty \operatorname{erf}(\eta) \quad (4.12)$$

Where $\operatorname{erf}(x) = \frac{2}{\sqrt{\pi}} \int_0^x \exp(-\eta^2)\, d\eta$ and $\eta = \frac{z}{2\sqrt{\mu t}}$. From the above solution, one can obtain the vorticity at the wall:

$$\omega(0, t) = \left[\frac{\partial v_x}{\partial z}\right]_{z=0} = \frac{V_\infty}{\sqrt{\mu t}} \quad (4.13)$$

Therefore, the tangential stress on the solid boundary or the fluid shear stress is given by,

$$\tau_w = \nu_L \left[\frac{\partial v_x}{\partial z}\right]_{z=0} = \frac{\nu_L V_\infty}{\sqrt{\pi \mu t}} = \rho V_\infty \sqrt{\frac{\mu}{\pi t}} \quad (4.14)$$

The above solution is now modified for spherical coordinates such that the direction of flow is radial outwards and to account for a finite rise in time, or any arbitrary $V_\infty(t)$. Assume that the fluid motion at $t$ is built up by infinitesimal impulses $dV_\infty(t')$, of the far field, at some time $t'$. Then,

$$dV(r,z,t) = dV_\infty(r,t')\,\mathrm{erf}\left(\frac{z}{2*\sqrt{\mu(t-t')}}\right) \quad (4.15)$$

The complete flow is given by the integral

$$V(r,z,t) = \int_0^t \frac{dV_\infty(r,t')}{dt'}\,\mathrm{erf}\left(\frac{z}{2*\sqrt{\mu(t-t')}}\right)dt' \quad (4.16)$$

and the wall stress is given by

$$\tau_w(r,t) = \rho\mu\left[\frac{\partial V}{\partial z}\right]_{z=0} = \rho\sqrt{\frac{\mu}{\pi}}\int_0^t \frac{dV_\infty(t')}{dt'}\frac{dt'}{\sqrt{(t-t')}} \quad (4.17)$$

Equations (4.16) and (4.17) provide a complete description of the velocity field and wall shear stress at any location before the arrival of the bubble wall. Moreover, the predictions given by these equations result from the application of the conservation of mass and momentum to the experimental data and contain no adjustable parameters.[9] Calculations of peak shear stress at a radial position away from the laser-induced cavitation epicenter from bubble dynamics data shown in **Figure 4.10** and **Figure 4.11** are shown in **Figure 4.12**. A maximum, peak stress of 3.7 MPa shown in **Figure 4.12** is found at 10 µm from the epicenter but falls off exceptionally fast to 7 kPa by 230 µm or at about the maximum size of the bubble for this data set. At nearly twice the maximum bubble distance or 400 µm away from the epicenter, the peak shear stress falls to 2.3 kPa. In general, the decay in peak stress as one moves away from the epicenter is drastic as evident by the log scale on the vertical axes.

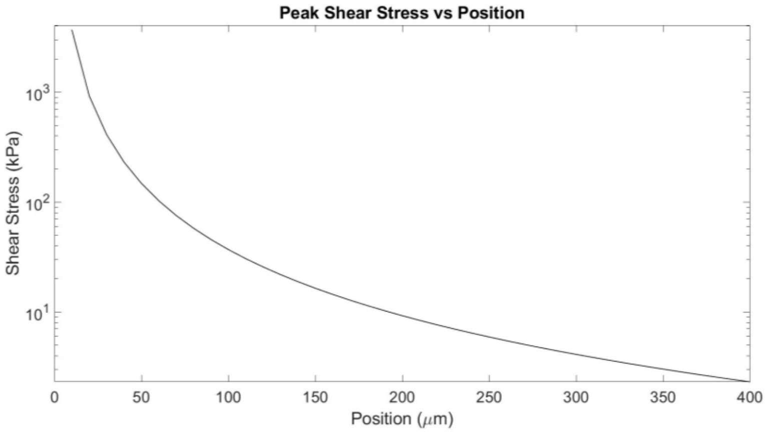

Figure 4.12 – Peak shear stress at a radial position away from the epicenter of laser-induced bubble cavitation.

### 4.4.3. Laser-Induced Shockwave Generation Using Low Magnification Objectives

Laser-induced shockwaves provide a means for generating consistent, spatiotemporal profiles of shear stress in vitro. In order to assess the effects of shear stress on whole cultures across large distances in real-time it becomes of interest to utilize lower magnification objectives that provide greater fields of view. However, low magnification objectives have the trade-off of a lower numerical aperture and, subsequently, reduces overall power delivered at the focal spot. The bubble dynamics and maximum bubble size are directly linked to the amount of energy absorbed at the focal spot. Thus, observed bubble dynamics and resulting shear stress profiles using 40x/1.3 and 20x/0.75 objectives are compared.

Since, the power threshold for plasma formation varies for each objective a ratio of power used to threshold power is used to compare experimentally found values for each objective. In **Figure 4.13** the bubble wall positions resulting from a fit

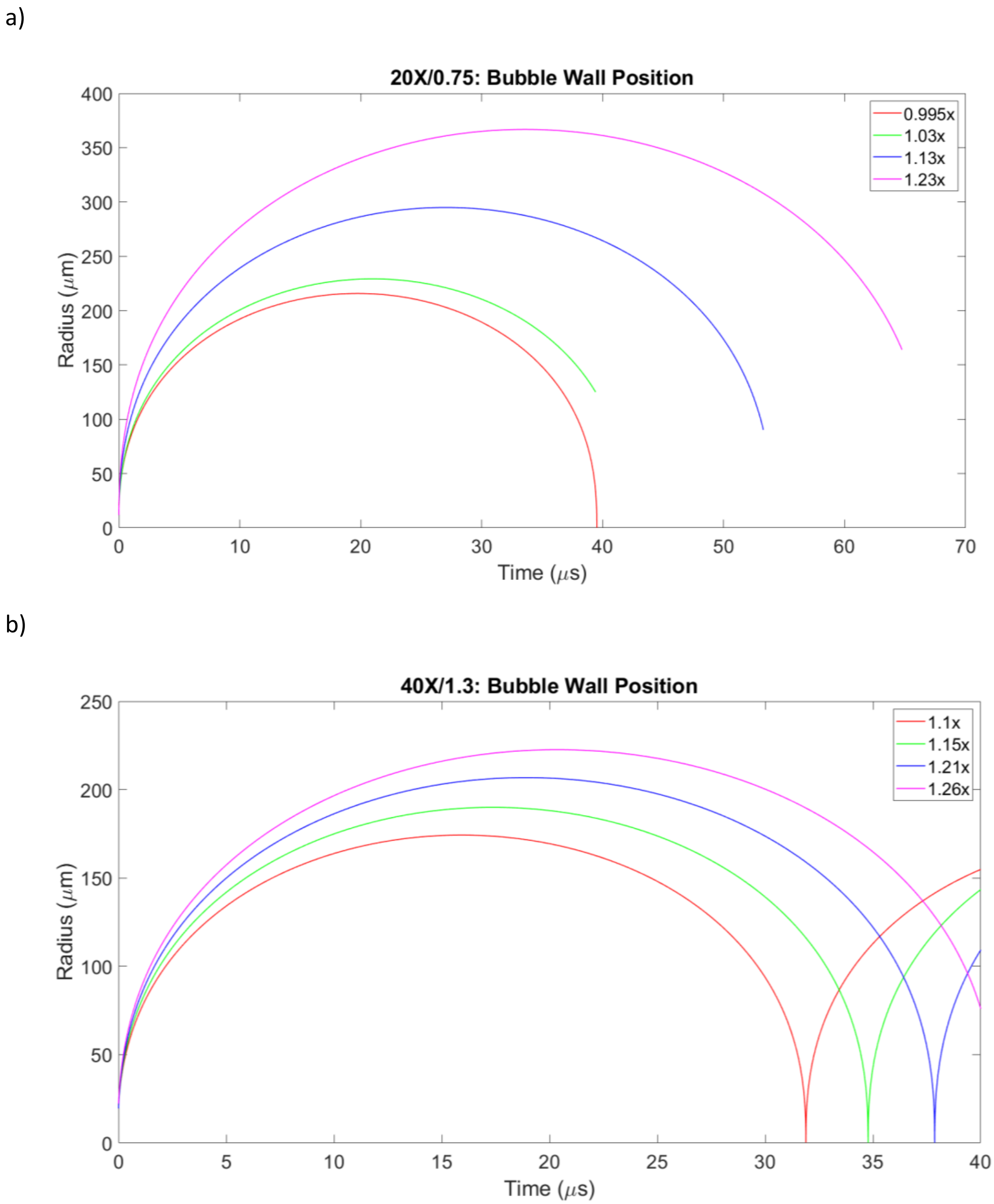

Figure 4.13 – Bubble wall positions resulting from Rayleigh-Plesset fit of experimental data for a) 20X/0.75 and b)40x/1.3 objectives. Here, each curve represents data found by using varying multiples of energy threshold.

of the Rayleigh-Plesset equation to experimental data is shown for both the 20X/0.75 objective **Figure 4.13a** and the 40X/1.3 objective **Figure 4.13b**. While the Rayleigh-Plesset describes the initial bubble period of expansion it does not account for energy loss that would result in a dampening of maximum bubble radii values at subsequent periods, which is shown in **Figure 4.13b**. The maximum radius of the bubble wall is compared between objectives in **Figure 4.14**. The resulting peak stresses calculated at a relative distance from the laser-induced bubble cavitation epicenter are shown in **Figure 4.15**. These peak stresses are compared between each objective in **Figure 4.16** and are plotted against maximum radius values shown in **Figure 4.15**.

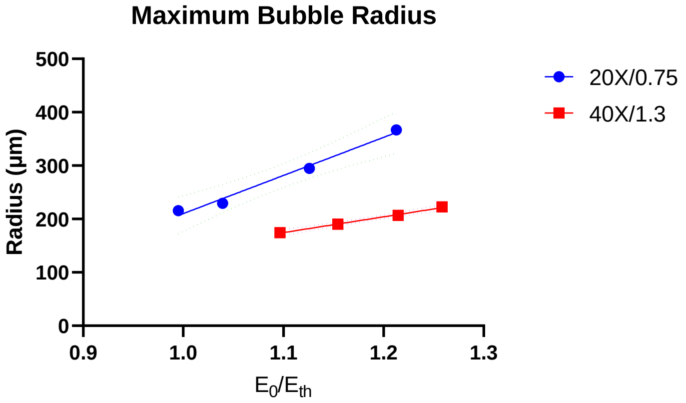

Figure 4.14 – Maximum bubble radius plotted against multiples of plasma formation energy threshold. Results are shown for different objectives 20X/0.75 (circle,blue) and 40X/1.4 (triange,red). Each data set has a line with 95% confidence intervals resulting from linear regression analysis.

From the data, it is evident that using the 20X/0.75 objective results in larger maximum bubble sizes and, subsequently, larger peak shear stresses. Interestingly, the beam spot size is effectively magnified twice as much, however, the threshold for plasma formation is increased by about 47%. From **Figure 4.16** it a ppears that the peak shear stress shares a linear relationship with the maximum bubble radius observed that at one point even seems to intersect between both objectives. It is unclear whether the relationship between maximum bubble radius and peak shear stress translates between objectives since, linear behavior is typically observed at values acquired at pump pulse energies exceeding that of the threshold value. However, there appears to be a close linear relationship between pump pulse energy and maximum bubble radius. Most likely, the initial

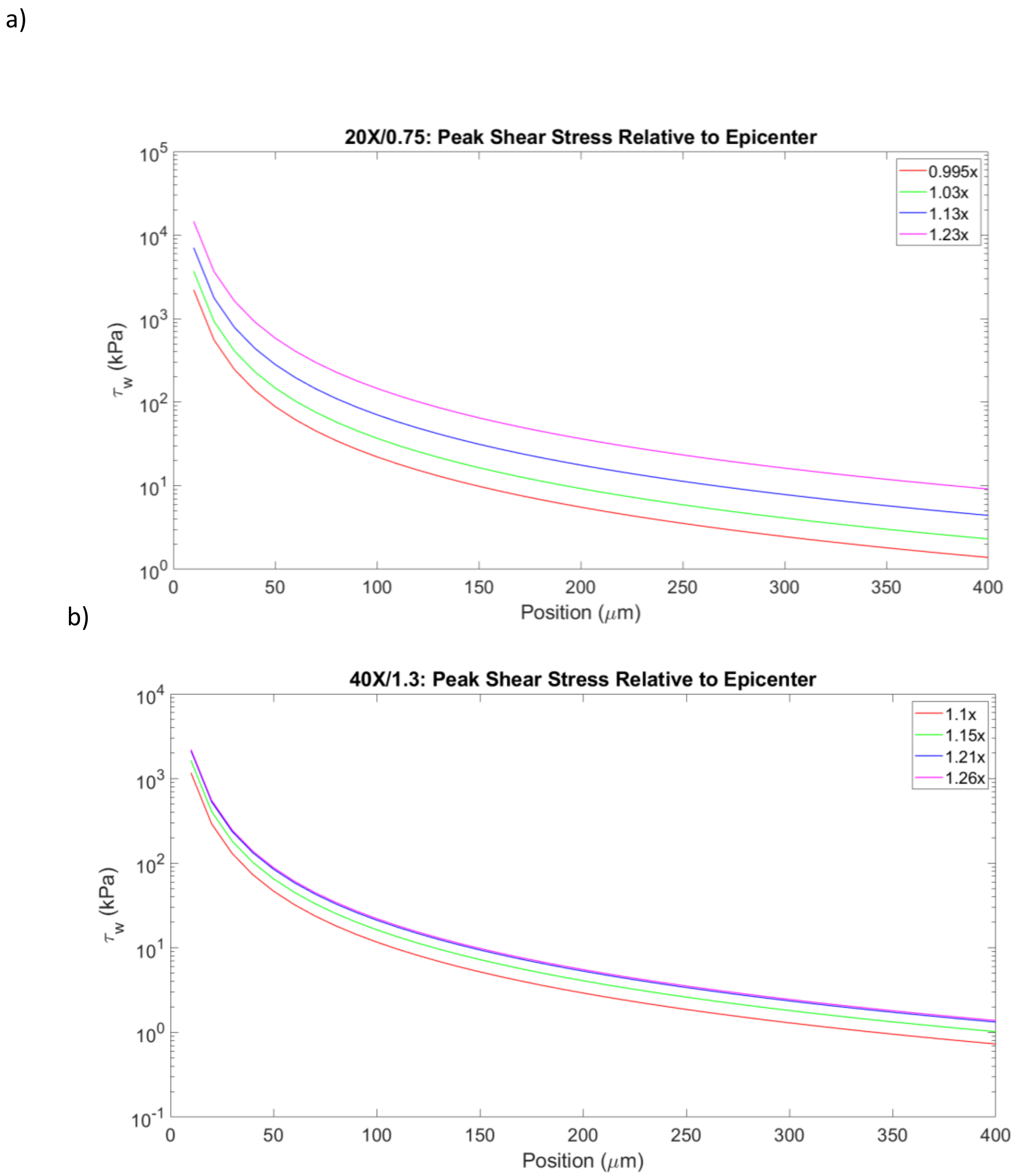

Figure 4.15 – Peak shear stress relative to position from laser-induced bubble cavitation epicenter. Calculations are generated from experimental data in Figure 5.12 for both a) 20X/0.75 and b)40x/1.4 objectives. Here, each curve represents data found by using varying multiples of energy threshold.

bubble size is constrained by the maximum plasma length, which is partly dependent on the energy density of a pump pulse in the focal volume. Larger maximum bubble sizes are dependent on larger initial bubble sizes. Therefore, lower-numerical aperture objectives with lower magnification generate larger initial bubble sizes and, subsequently, larger peak shear stresses. In addition, the use of a lower magnification objective would subject larger populations of cell culture to a broader range of forces in comparison to the use of higher numerical aperture and higher magnification objectives.

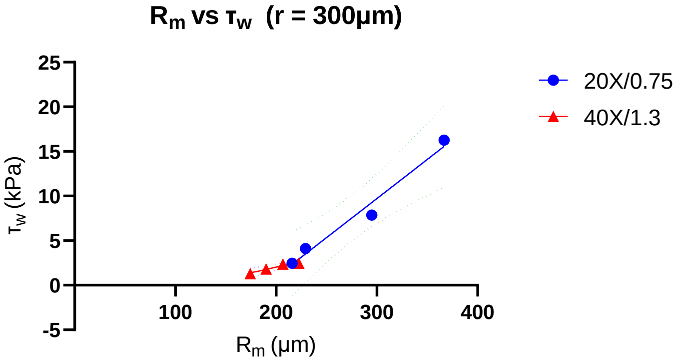

Figure 4.16 – Maximum bubble radius plotted against peak shear at a distance relative to the laser-induced bubble cavitation epicenter. Results are shown for different objectives 20X/0.75 (circle,blue) and 40X/1.3 (triange,red). Each data set has a line with 95% confidence intervals resulting from linear regression analysis.

## 4.5. Discussion

### 4.5.1. Comparison to Current Techniques

Among several in vitro TBI models, apparatuses have been developed to apply blast-like impacts to cell cultures. One model developed by Panzer and colleagues utilizes a shock tube capable of generating a peak pressure of up to 650 kPa with a positivity duty-cycle between 0.3 and 3 msec. [10] A chamber located at one end of the shock tube separated by a PET membrane is gradually filled with pressurized gas until the membrane ruptures, which leads to the propagation of a shock wave through the shock tube. Another design proposed by Ravin and colleagues makes use of an air gun to generate a wave of pressurized gas, which is then directed onto a cell culture well. [10,11] In a recent review[10] of in vitro TBI models, only three studies[11-13] were found that implemented a novel blast model. Vogel and colleagues applied a shockwave with a peak pressure of 336 kPa, which was closest to the estimate lethal range of 414-552 kPa or 60-80 psi. [12,14] Interestingly, Arun and colleagues applied only 145 kPa or 21 psi, which is about a quarter of the lethal range.[13] Additional studies found that measures of neuronal function were significantly altered at exposures of 336 kPa with positive duty-cycles of 0.84 ms or 86.5 kPa*ms.[15] Thus, functional changes occur below the threshold for cell death. Interestingly, a study by Ravin and colleagues indicated that neurons under pressure without concomitant shear forces, peaking between 0.3 to 0.7 at the cell surface, could tolerate overpressures as high as 220 psi.[16]

While these discrepancies result from differences in study aims and apparatus design, more consistent approaches would allow for more accurate characterization of cellular behaviors. There is a clear capacity for LIS to offer more consistent, studies of shear stress while providing for large ranges of pressure. Because of the current, untreatable condition of TBI, there is great motivation for high-throughput methods in order to assess the effectiveness of potential therapeutic candidates. The well-defined spatiotemporal profile of LISs allow for a more accurate assessment on functional changes resulting from the variation of applied shear stress by monitoring neurons by distance from the blast epicenter. The ideal in vitro model captures transient changes and allows for subsequent access to later timepoints to capture long-term functional changes. LISs is a non-contact method that preserves the sterility and minimizes damage to cells outside of experimentation thus, this technique offers the ability to pursue long-term studies on in vitro models. In addition, models should account for the structural complexities of the brain since, current in vitro models do not. The force measurement system utilized here is highly adaptable to any microscope system and more easily adaptable to different models of specimens.

### 4.5.2. Future Applications

Later studies will utilize the Coherent FlareNx 1030nm in order to open the entire visible light spectrum for data acquisition purposes while performing fluorescent microscopy experiments. The above analysis can be applied with minor modifications accounting for the difference in wavelength of the pump pulse source. This change in wavelength will indirectly change approximations of time of plasma formation and maximum plasma length. However, the beam spot size used in earlier studies was well above the diffraction limit at nearly half a micron. Thus, the effects are likely negligible, and one should say peak shear stresses within the same order of magnitude as seen between differing objectives above.

With the current system real-time measurements are possible by an indirect method that uses maximum bubble size data to determine peak shear stress. Otherwise, there is not enough temporal resolution to accurately resolve a single time-series acquisition using our current configuration.

## CHAPTER REFERENCES

1. A. N. Hellman, “Biophysical response to pulsed laser microbeam-induced cell lysis and molecular delivery,” vol. 35, no. 1, pp. 24–35, 2008.

2. H. J. Eichler, U. Klein, and D. Langhans, “Measurement of orientational relaxation times of rhodamine 6G with a streak camera,” *Chem. Phys. Lett.*, vol. 67, no. 1, pp. 21–23, 1979.

3. Brennen, C. E. (2013). *Cavitation and Bubble Dynamics*. *Cavitation and Bubble Dynamics*. Cambridge: Cambridge University Press.

4. A. Vogel, J. Noack, G. Hüttman, and G. Paltauf, “Mechanisms of femtosecond laser nanosurgery of cells and tissues,” *Appl. Phys. B Lasers Opt.*, vol. 81, no. 8, pp. 1015–1047, 2005.

5. Evans, R., Camacho-López, S., Pérez-Gutiérrez, F. G., & Aguilar, G., “Pump-probe imaging of nanosecond laser-induced bubbles in agar gel,” Optics Express, 16(10), 7481, 2008.

6. A. Vogel, K. Nahen, D. Theisen, and J. Noack, “Plasma formation in water by picosecond and nanosecond Nd:YAG laser pulses - Part I: Optical breakdown at threshold and superthreshold irradiance,” *IEEE J. Sel. Top. Quantum Electron.*, vol. 2, no. 4, pp. 847–859, 1996.

7. W. Lauterborn and A. Vogel, *Shock Wave Emission by Laser Generated Bubbles*. 2013.

8. M. Lokhandwalla and B. Sturtevant, “Mechanical haemolysis in shock wave lithotripsy (SWL): I. Analysis of cell deformation due to SWL flow-fields,” *Phys. Med. Biol.*, vol. 46, pp. 413–437, 2001.

9. K. R. Rau, P. A. Quinto-Su, A. N. Hellman, and V. Venugopalan, “Pulsed laser microbeam-induced cell lysis: Time-resolved imaging and analysis of hydrodynamic effects,” *Biophys. J.*, vol. 91, pp. 317–329, 2006.

10. Y. H. Wu, S. Rosset, T. R. Lee, M. Dragunow, T. Park, and V. Shim, “In Vitro Models of Traumatic Brain Injury: A Systematic Review,” *J. Neurotrauma*, vol. 38, no. 17, pp. 2336–2372, 2021.

11. R. Ravin, P.S. Blank, B. Busse, N. Ravin,S. Vira, L. Bezrukov, H. Waters, H. Guerrero-Cazares, A. Quinones-Hinojosa, P.R. Lee, R.D. Fields, S.M. Bezrukov, and J. Zimmerberg, ”Blast shockwaves propagate Ca2+ activity via purinergic astrocyte networks in human central nervous system cells,” *Sci. Rep.*, vol. 6, 2016.

12. E.W. Vogel 3rd, F.N. Morales, D.F. Meaney, C.R. Bass, and B. Morrison 3rd, “Phosphodiesterase-4 inhibition restored hippocampal long term potentiation after primary blast,” *Exp. Neurol.*, vol. 293, pp. 91–100, 2017.

13. P. Arun, J. Spadaro, J. John, R.B. Gharavi, T.B. Bentley, and M.P. Nambiar, “Studies on blast traumatic brain injury using in-vitro model with shock tube,” *Neuroreport*, vol. 22, no. 8, pp. 379–384, 2011.

14. Committee on Gulf War and Health: Long-Term Effects of Blast Exposures; Board on the Health of Select Populations; Institute of Medicine. Gulf War and Health, Volume 9: Long-Term Effects of Blast Exposures. Washington (DC): National Academies Press (US); 2014 Apr 14.

15. N. E. Zander, T. Piehler, M. E. Boggs, R. Banton, and R. Benjamin, “In vitro studies of primary explosive blast loading on neurons,” *J. Neurosci. Res.*, vol. 93, no. 9, pp. 1353–1363, 2015.

16. R. Ravin, P.S. Blank, A. Steinkamp, S.M. Rappaport, N. Ravin, L. Bezrukov, H. Guerrero-Cazares, A. Quinones-Hinojosa, S.M. Bezrukov, and J. Zimmerberg, “Shear forces during blast, not abrupt changes in pressure alone, generate calcium activity in human brain cells,” *PLoS One*, vol. 7, no. 6, 2012.

# Chapter 5: Conclusions

## 5.1. Summary

The studies in Chapter 2 on the cultivation of primary, dissociated cortical neurons highlight practical considerations for producing viable cultures. Neuronal cultures were sensitive to changes in osmolarity resulting from evaporation during incubation. From these studies, it is unclear how sensitive cortical neuronal cultures are to increases in osmolarity and whether there are perceived differences between the rate of change in osmolarity. Previous studies have indicated a rise of >50 mOsm is lethal to neuronal cultures[1], which would be about 116% of physiological osmolarity or 305 mOsm. While the lethal effects of increasing osmolarity is visually evident after several weeks of routine maintenance, it is unknown to what extent shifts in osmolarity prompt significant deviations from physiologically relevant in vitro conditions or how these deviations could vary across different cell types. Moreover, improving the consistency across in vitro cell cultures by accounting for shifts in osmolarity could improve the reproducibility of experimentation between different disease models and/or pharmacological studies. A generalized model for evaporation of media within a culture dish as a function of relative humidity (Equation (2.2)), can be utilized to approximate evaporation rates given real-time measurements of humidity or average, empirically determined values. Changes in volume were calculated by measuring changes in mass over time thus, a potential improvement in current incubators would be the addition of weight sensors to monitor and to account for changes. Furthermore, evaporation can be mitigated using hydrophobic, semi-permeable plate sealing membranes and PDMS fabricated lids.

From results in Chapter 3, the spontaneous intracellular calcium activity of BACHD cortical neurons differ significantly from activity observed in wild type neurons. Moreover, it appears inhibition of excitatory activity recapitulates trends observed in BACHD values for inhibited, wildtype samples in the nucleus. Early stages of HD are linked to striatal spiny neurons (SPNs), which are the first neurons to show dysfunction and loss, that suppress cortical excitation.[1] Sustained reductions in frequency of intracellular calcium activity may be suggestive of reduced responses to excitatory activity independent of inhibition from SPNs. Furthermore, inhibition of excitatory activity revealed lower frequencies of transient calcium events which is suggestive of lower levels of calcium-mediated intracellular activity. In this manner, parametrization and statistical analysis of Fluo 4 emissions activity appears capable of resolving characteristic differences of intracellular calcium activity in BACHD cortical neurons. Elevated basal levels of intracellular calcium is a hallmark of various chronic neurodegenerative disorders. However, further experiments are needed to fully characterize the cause of elevated basal levels of intracellular calcium encountered in BACHD cortical neurons. The data here suggest that excitatory activity is linked to the onset of sustained elevations of basal intracellular calcium levels observed in BACHD cortical neurons, the mechanisms of which are unclear from calcium-imaging data alone. There are clear benefits to performing additional experiments at later DIVs to resolve differences between genotypes over time, which may further highlight sustained differences in parameters. It would be of significant interest to monitor gene expression in relation to changes in calcium-imaging data. Future experiments seeking to resolve differences in intracellular calcium may find more success at or after 13-14 DIVs where

BACHD neurons have reached a metastable calcium homeostasis in the absence of sustained environmental stress.

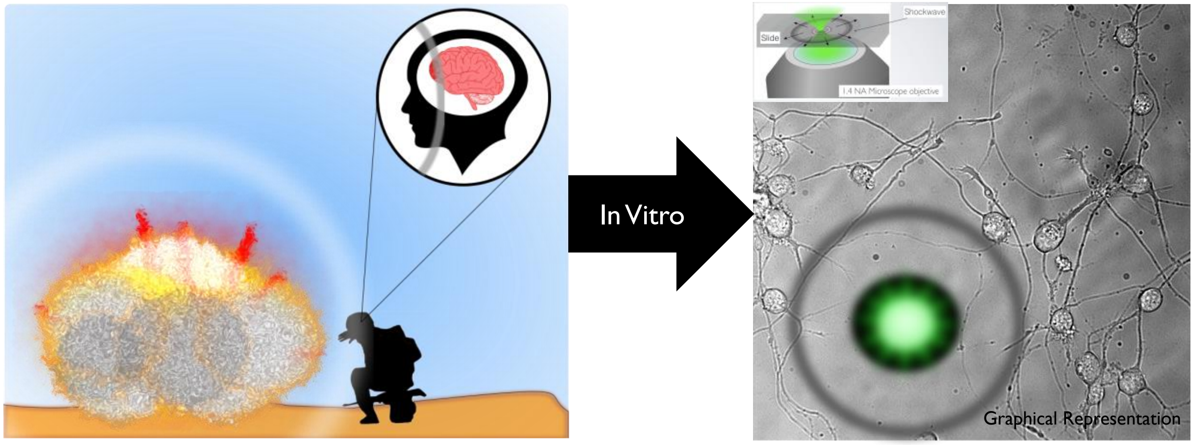

Figure 5.1 – Laser-induced shockwaves as a blast-injury model for early pathology of traumatic brain injury (TBI).

Among several in vitro TBI models, apparatuses have been developed to apply blast-like impacts to cell cultures. However, there are discrepancies in the magnitude of forces used resulting from differences in study aims and apparatus design, more consistent approaches would allow for more accurate characterization of cellular behaviors. From the results in Chapter 4, there is a clear capacity for laser-induced shockwaves (LISs), depicted in **Figure 5.1** to offer a more reproducible means of generating shear stress while providing a large range of pressures. Because of the current, untreatable condition of TBI, there is great motivation for high-throughput methods in order to assess the effectiveness of potential therapeutic candidates. The well-defined spatiotemporal profile of LISs allow for a more accurate assessment of functional changes resulting from the varying magnitudes of applied shear stress by monitoring neurons at varying distances from the blast epicenter. In addition, the utilization of low-magnification objectives increases the population size of samples exposed to varying magnitudes of shear stress by imaging larger fields of view and generating larger blast radii. The ideal TBI in vitro model captures transient changes and allows for subsequent access to later timepoints to capture long-term functional changes. LISs is a non-contact method that preserves the sterility of samples and minimizes damage to cells outside of experimentation thus, this technique offers the ability to pursue long-term studies on in vitro models. Furthermore, LISs can provide great insight into the early pathology induced by blast-injury at a molecular level.

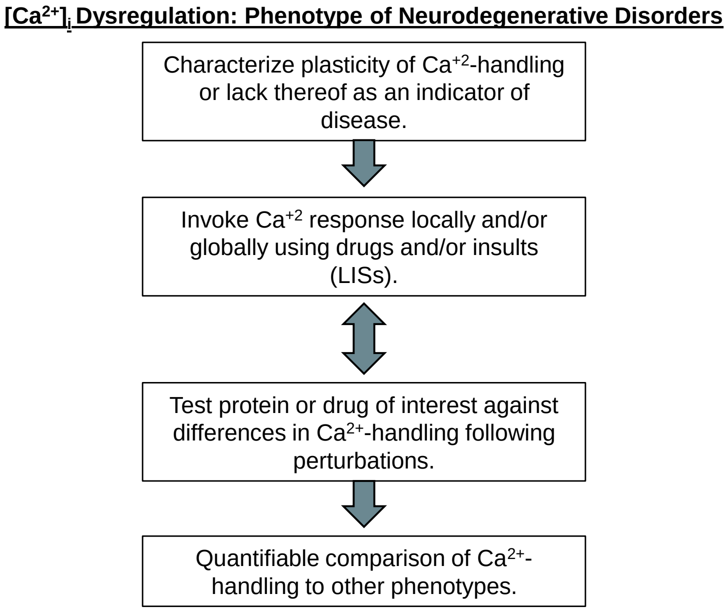

Figure 5.2 – Workflow for investigating intracellular calcium dysregulation.

## 5.2. Discussion

The results from the studies described in this dissertation offers solutions towards the pursuit of high-throughput experiments of chronic neurodegenerative disorders with regards to calcium-imaging. The calcium-imaging studies in this dissertation compare well-defined parameters that characterize transient, peaks in calcium-dependent emissions intensity data. Huntington’s disease like several other chronic neurodegenerative disorders manifest symptoms over long periods of time. Thus, the differences between the control and disease cell models are highlighted in aged cultures. To date there has not been a comprehensive characterization of intracellular calcium activity in the BACHD cortical neuron and to the author's knowledge no analysis of the kind in this dissertation has yet been performed. Moreover, the parametrization of calcium-based fluorescence offers a novel way of quantifying relative differences between control and disease cell models. While calcium facilitates quick and transient signals, it is evident that subtle, functional differences in the presence of pathological conditions can be observed over time. While the reasons behind calcium dysregulation can vary between disease models, the ability to characterize intracellular calcium over time can help elucidate potential treatments and mechanisms. In general, whether calcium dysregulation is a cause or effect of pathology in HD is unclear. If the characterization of intracellular calcium differs dramatically between different chronic neurodegenerative disorders then that would be suggestive of very different mechanisms resulting in calcium dysregulation. Otherwise, comparable, cumulative differences in intracellular calcium activity over longer periods of time may be suggestive of a symptomatic role for calcium dysregulation. **Figure 5.2** depicts a potential work flow for utilizing calcium dysregulation as a tool for drug discovery and or diagnostics.

## 5.3. Future Approaches

Utilizing intracellular calcium dysregulation as a phenotypic marker for neurodegenerative disorders could supplement and aid the discovery of potential avenues of therapy. Careful control of cell incubation conditions ensure reproducible and consistent results while pursuing high-throughput methods of calcium-imaging studies. By automating the analysis of calcium-imaging, experimenters have easier access to the analysis of several trials and time-points to characterize intracellular calcium activity in the context of neurodegeneration. Tracking intracellular calcium activity can identify windows of experimentation that highlight chronic neurodegeneration as opposed to perturbations in cell development that result from a disease model. The strengths of the methods and analytical tools described in this dissertation are evident from its scalability to high-throughput experimentation and its capacity to resolve subtle differences in emissions between diseased and control cells. Following proper characterization of disease models of interest with regards to intracellular calcium activity comparing the application of potential treatments could help elucidate candidates for additional experimentation. Future experiments would involve comparisons of spontaneous calcium activity with or without treatment. In addition, calcium dysregulation within the cell may lead to higher activity of phosphokinases such as PKC and, subsequently, lead to higher levels of phosphorylated proteins.[2] Thus, another avenue of linking functional differences resulting from intracellular calcium dysregulation in cells would be to monitor intracellular phosphorylation activity. Moreover, characterizing subtle differences in intracellular calcium activity between treated and untreated samples could aid in the discovery of disease-modifying treatments that are not exclusive to chronic neurodegeneration.

## 5.4. Acknowledgements

This research was supported by grants from the Beckman Laser Institute Foundation, the Institute of Engineering and Medicine, the Air Force Office of Scientific research under FA9550-14-1-0034, and the National Institute for Neurological Disorders and Stroke of the National Institutes of Health under P01NS092525-01A1.

## CHAPTER REFERENCES

1. L.A. Raymond, ”Striatal synaptic dysfunction and altered calcium regulation in Huntington disease,” *Biochemical and Biophysical Research Communications*, 2016.

2. A. C. Newton, M. D. Bootman, and J. Scott, “Second messengers,” *Cold Spring Harb. Perspect. Biol.*, vol. 8, no. 8, 2016.

# Appendix

## A. Supplemental Data

### A.i. Mouse Colony Statistics

### A.i.a. Pregnancy Rate in Colony

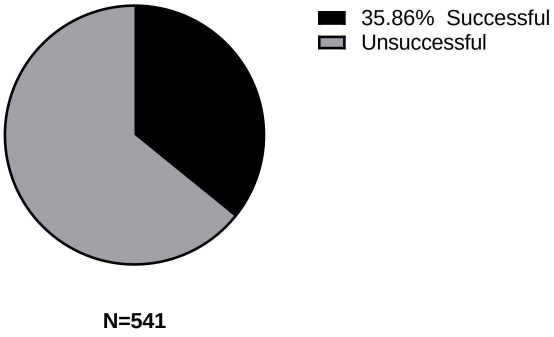

Figure A.i.a – Distribution of successful and unsuccessful breeding pairs of mice in colony. Pregnancy rate or percentage of successful pregnancies found for total number of breeder pairs set-up.

### A.i.b. Pregnancies by Age

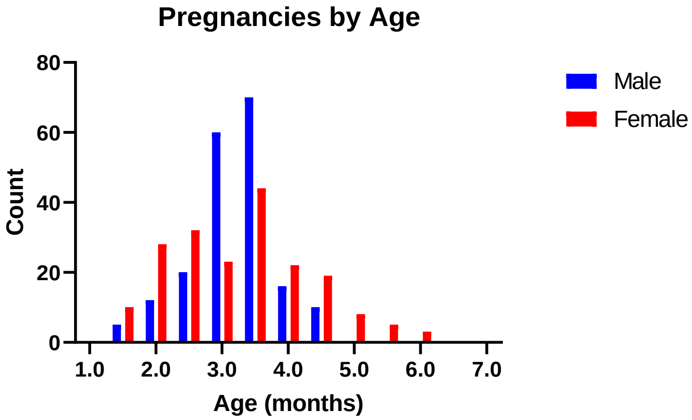

Figure A.i.b – Count of successful breeder pairs or pregnancies binned by months with bin width of 0.5 months. Total counts at particular ages are shown for male (blue) and female (red) mice.

### A.i.c. Probabilities of Pregnancy by Age for Gender and Genotype

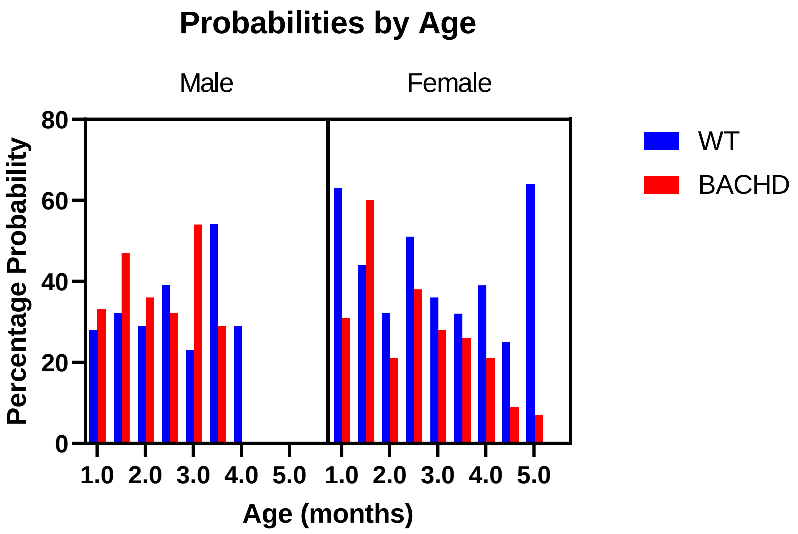

Figure A.i.c – Probability of successful pregnancy for given partner of specified gender and genotype. Probabilities are calculated from binned events having a bin width of 0.5 months.

### A.i.d. Average Chance of Pregnancy by Gender and Genotype

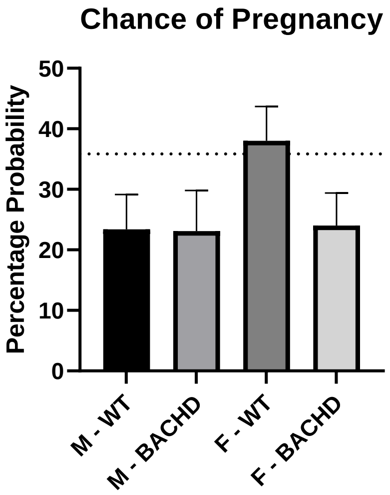

Figure A.i.d – Chance of pregnancy for specified breeding partner with gender and genotype. Dotted line indicated average pregnancy rate given in Figure A.i.a.

## B. Protocols

### B.i. BACHD Genotyping

Time: ~4 hours

Genotyping of mice via PCR of tail-derived DNA samples on 2% agarose gel. Tail samples are assumed collected and dissolved in 300 µL of a 50 mM solution of NaOH and, with caps closed, incubated for at least 1 hour at 90ºC. This ensures the dissolution of tissue and the release of DNA into the solution. After incubation, tubes are left on ice or at room temperature for at least 5 minutes. Then, an addition of 60 µL of 0.5 M Tris-HCL at pH 8.0 is made to neutralize the sample. Finally, samples are centrifuged at 13k RPM for 2 minutes before use or storage at -20ºC. Frozen samples are thawed and returned to storage.

Materials:

- Distilled water
- 1X Tris-acetate-EDTA (**TAE**) buffer
- Taq 2X Mean Green Master Mix (**Mean Green**)
- Primers (yields bands of ~130bp)
  - HTT5': GAG CCA TGA TTG TGC TAT CG
  - HTT3': AGC TAC GCT GCT CAC AGA AA

Equipment:

- T100 Thermal Cycler (Biorad, Herculeus, CA, USA)
- ChemiDoc XRS+ System (Biorad, Herculeus, CA, USA)
- 2% agarose gel
- Electrophoresis cell
- Voltage generator

1. Load 2% agarose gel into electrophoresis cell with 1X TAE buffer so that wells on the gel are submerged.

2. Prepare a stock solution of 9 µL per sample, in addition to two control samples, that contains 5 µL Mean Green, 0.1 µL HTT5' (100 µM), 0.1 µL HTT3'(100 µM), and 3.8 µL of distilled water.

3. Then, aliquot 9 µL from stock into PCR tubes for use in PCR thermal cycler.

4. Add 1 µL of the tail-derived, DNA sample into each PCR tube for a total sample volume of 10 µL.

5. PCR thermal cycle conditions:

    i. Initial Denature: 94ºC for 3 minutes
    ii. Denature: 94ºC for 30 seconds
    iii. Anneal: 55ºC for 45 seconds
    iv. Extend: 72ºC for 30 seconds
    v. Final Extend: 72ºC for 3 mins
    vi. Repeat ii-v 32 times (~2.5 hours)

6. Following completion of PCR, carefully load each 10 µL into an individual well along the agarose gel.

7. Ensure current flow from top of well to bottom of well is negative to positive then, run voltage at 100V for 30min or until color separations of blue and yellow bands are clearly visible along gel. Use ChemiDoc gel imaging system to visualize any bands under UV exposure. By comparing positive and negative controls one can determine genotype.

B.ii. 2% Agarose Gel Preparation

Time: 30-45 mins

Volumes here are chosen to mold a 40-well gel for use in an electrophoresis cell.

Materials:

- 1X Tris-acetate-EDTA (**TAE**) buffer
- Agarose
- Green Glo Safe DNA Dye

Equipment:

- FS-20 Tabletop Ultrasonic Cleaner (Fisher Scientific)

1. Fill an Erlenmeyer flask with 100 mL of 1x TAE buffer.

2. Heat up container in microwave for about 30 seconds or until boiling.

3. While swirling liquid in glass flask, dissolve 2 g of agarose into 100 mL of 1x TAE Buffer.
4. Continue swirling liquid until agarose is fully dissolved. Repeat step 2 as necessary.
5. Ensure volume of 100 mL and replace TAE buffer if excessive boiling has occurred.
6. Let agarose gel solution cool until it is warm to touch comfortably. Optional: Degas to remove excess bubbles as describes below.
7. Mix 5 µL of Green Glo Safe DNA dye into the agarose gel solution and swirl glass to mix.
8. Prepare agarose gel mold with well moldings and pour out agarose gel solution.
9. Allow the gel to cool and solidify.
10. Take gel plate and wrap with saran wrap and store in fridge until ready to use.

De-gassing:

1. Ensure water bath in ultrasonic cleaner is heated to at least 40ºC.
2. Place agarose contained in erlyenmer flask into ultrasonic cleaner ensuring the correct water level.
3. Set degas option for 20 min and activate sonication mode.
4. Repeat for 5 minute intervals if bubbles are still present.

### B.iii. Coverslip and Glass Bottom Dish Wash Protocol

Time: 4-5hrs

This protocol details the preparation of glass coverslips for cell culture use. The workflow follows soaking, swirling, and sonicating coverslips in various solutions in order to clean and to sterilize the glass prior to its use to plate cells. The sonication step with soapy water ensures de-greasing of coverslips as the arrive from manufacturers. The subsequent rinses and sonication with distilled and double distilled water ensure the removal of soapy residue and any remaining organic materials. Ethylenediaminetetraacetic acid (EDTA) is used in order to chelate all ions and prevent their precipitation upon drying of coverslips. In addition to sterilizing, the first rinse with 70% ethanol aids in the removal any residual EDTA via precipitation and rinsing. The final rinse with 100% ethanol aids in further removal of any residual EDTA, organisms, and acts as a solvent for long-term storage of the coverslips.

The protocol is the same for glass bottom dishes and iBidi polymer bottom dishes, however, none of the steps require heating since, this will weaken the adhesive between glass and plastic so, coverslips detach rendering the dish useless. Thus far, it seems dishes can be rewashed a few times before discarding from wear.

Note: Used dishes should first be soaked with 30% HCl, and set on rotary stage on low overnight to remove any persistent debris that is adhered to the coverslip from previous use. This includes culture well plates.

Materials:

- Fisher Scientific Water Bath Sonicator (FS20D)
    - Be sure to keep the FS20D bath sonicator filled 1 in from top before operating. Fill following evaporation of solution using distilled water.
    - If the soapy water appears cloudy be sure to change out the cleaning solution by unplugging the unit and rinsing the bath out in the sink a few times using DI water.
    - The FS20D has a capacity of 2.8 L, after cleaning refill with 1% Versa Clean diluted in DI water.
- Sonics & Materials, Inc. Vibracell VC100 (VCX100): Submersible Sonicator Probe
    - Be sure to rinse VCX100 sonicating probe tip with double distilled before using it to sonicate each solution. You can turn on the sonicator probe briefly to immediately vaporize any residual liquid.
    - For proper usage, center and submerged soincator probe tip at least 1 cm into solution. In the case of 500 mL beakers filled to the 100 mL line,

the tip should reach the 50 mL line of the beaker located ~1 cm from 100 mL line. In most cases, you will want to fill the beaker to its maximum, metered volume unless minimized use of solvent is desired.

- 500 mL beaker
- 1% Versa-Clean™ (cat no. 18-200-701, Fisher Scientific)
- 1 mM Ethylenediaminetetraacetic acid (EDTA)
- Glass jar with lid for storage

1. Place coverslips <u>one at a time</u> into the water-bath sonicator (FS20D) pre-heated to 60°C and containing 1% Versa-Clean™ detergent solution. Take care to separate coverslips that are stuck together and toss if unable to separate. <u>If washing glass/polymer bottom dishes do not have water-bath sonicator pre-heated and do not incubate dishes in water bath!</u>

2. Sonicate coverslips in heated, water-bath sonicator for 60 mins.

3. Rinse coverslips 10 times by gently, swirling with distilled water. <u>Swirl with enough force to allow greater surface area exposure of coverslips that might have stacked, but not enough to break them.</u>

4. Fill beaker with distilled water and take to cold room in order to sonicate with VCX100 for 30 mins while heating in water-bath incubator.
5. Rinse coverslips 10 times by swirling with double-distilled water.

6. Fill beaker with double-distilled water and take to cold room in order to sonicate with VCX100 for 30 mins while heating in water-bath incubator.
7. Afterwards, Rinse coverslips 3 times by filling beaker enough to submerge all coverslips and by swirling with 1 mM EDTA.

8. Fill beaker with enough 1 mM EDTA to submerge contents and take to cold room in order to sonicate with VCX100 for 30 mins while heating in water-bath incubator.

9. Rinse coverslips 3 times by filling beaker half-full (250 mL) and by swirling with 70 % ethanol. Toss solvent used on the first rinse, but collect solvent from subsequent rinse <u>in original container and re-use</u>.

10. Fill beaker with enough 70% ethanol to submerge contents and take to cold room in order to sonicate with VCX100 for 30 mins while heating in water-bath incubator.

11. Rinse coverslips 3 times by filling beaker half-full (250 mL) used 100% ethanol and by gently swirling. Toss solvent used on the first rinse, but collect solvent from subsequent rinses <u>into a separate container clearly labelled used for later use</u>.

12. Fill beaker with enough unused, 100% ethanol to submerge contents and take to cold room in order to sonicate with VCX100 for 30 mins while heating in water-bath incubator. Collect this ethanol into a container labelled used 100% ethanol for later use.

13. Rinse coverslips once more with 100% ethanol.

14. Rinse out a clean glass jar for storage of cleaned coverslips/dishes with a minimal amount of fresh 100% ethanol. Collect solvent for later use.

15. Swirl beaker with glass coverslips in order to suspend them in solution and then, pour out coverslips into storage jar. Repeat as necessary in order to fully transfer coverslips into glass jar. Collect any excess ethanol for later use.
16. Seal container with parafilm and store at room temperature.

Practical Considerations:

- While the rinse with 70% ethanol does sterilize cover glass surfaces, it is also used to remove residual EDTA. It is cleared out by first rinse and in order to prevent build up of EDTA in the stock of solvent the first rinse is tossed.

- In general, re-use of ethanol is recommended to prevent depletion of our stocks and minimize cost without reducing efficacy. One can re-use “used” 100% ethanol in order to refill stock solution of 70% ethanol prior to using fresh 70% ethanol.

- The protocol can be carried out over multiple days, just make sure to label all beakers. Also, indicate whether or not contents have already been sonicated in current solvent.

### B.iv. Primary Neuron Culture Plating

Time: 6-48hrs

Primary dissociated neuron culture preparation requires two days of preparation assuming cleaned microfluidics are available by day *in vitro* -1 (DIV-1) and sterilized coverslips are available by DIV-1. DIV0 is day of mouse dissection, tissue harvest, and culture seeding. While not explicitly stated work is carried out in biosafety cabinet while practicing sterile technique. Similarly, preparation carried out through

DIV-2 – DIV-1 can be performed at most a week in advance with coverslips stored at 4°C until day of dissection or DIV0. All cell media used is prepared fresh or stored no longer than 2 weeks at 4°C prior to usage. For cases where only mass cultures are required microfluidics are not needed and 24 microwell plates are used in conjunction with Ø 12 mm circular coverslips as opposed to 24x30mm coverslips. When using 96-well plates no coverslips are used, but substrate coating of well bottom is still performed.

Materials:

- Poly-D-Lysine 1 mg/mL (**PDL**) (A-003-E, Sigma-Aldrich, USA).
- Laminin Mouse Protein, Natural (23017015, Gibco, USA).
- Hibernate E, Low Fluorescence (**Hib-E**) (HELF, Brainbits LLC, Springfield, IL, USA).
- Hanks Buffered Saline Solution 10x (**HBSS**) (14185052, Gibco, USA).
- Penicillin-Streptomycin 10,000 U/mL (**Pen/Strep**) (15140122, Gibco, USA).
- HEPES 1 M (15630080, Gibco, USA).
- GlutaMAX 100x (35050061, Gibco, USA).
- Neurobasal Neuronal Medium (**NB**) (21103049, Gibco, USA).
- B-27 Supplement 50x, serum free (17504044, Gibco, USA).
- DNase I, grade II 10 mg (101041597, Sigma-Aldrich, USA).
- TrypLE 10x, no phenol red (A1217701, Thermo Fisher Scientific, USA).
- Fetal Bovine Serum, Heat Inactivated (FBS) (10082147, Gibco, USA).
- Brainphys Neuronal Medium (**BP**) (5790, Stemcell Technologies, Cambridge, MA, USA).
- SM1 Neuronal Supplement (5711, Stemcell Technologies, Cambridge, MA, USA).
- Tissue Culture Plates/Dishes:
    - 24-well tissue culture plate, polystyrene, sterile, tissue culture treated, optically-clear flat bottom, pyrogen free (25-107, Genesee Scientific, San Diego, CA, USA).
    - 96-well-F tissue culture plate, sterile, (10062-900, Radnor, PA, VWR, USA).
    - Ø150 x 22 mm tisue culture dish, sterile, tissue culture treated, opitcally clear, pyrogen free (25-203, Genesee Scientific, San Diego, CA, USA).

- Glass coverslips:

    - 24x30 mm (Cat No. 2975-243, Corning Inc., Corning, NY, USA).
    - Ø12 mm (12-545-30, Fisherbrand, USA).

Equipment:

- Biosafety cabinet, with UV light cycle.
- Vacuum Aspirator
- Centrifuge
- Incubation chamber set at 37°C with 5% $CO_2$ and humidified.

Reagents by DIV:

DIV-2:

- PDL
- Borate buffered Saline pH 8.5 @ 25°C (BBS)
- Sterilized coverslips

DIV-1:

- Laminin
- Sterile $ddH_20$
- Sterilized microfluidic chambers
- Sterilized, PDL-coated coverslips

DIV0

- Sterile $ddH_20$.
- HBSS + 1% Pen/Strep + 2.5% HEPES solution (**HBSS+**)
- Plating media: NB, 2% B27, 1% GlutaMAX, 1% Pen/Strep, 10% FBS
- Fire-polished glass pipettes and bulb
- Brain tissue in Hib-E acquired via dissection
- 10x TrypLE
- 10 mg/mL (10x) DNAse

DIV1

- Maintenance media: BP, 3% SM1, 1%Glutamax.

DIV-2: (7 Steps)

1. Take stock PDL out of -20°C storage and place in biosafety cabinet to thaw.

2. Once thawed, vortex PDL stock for a few seconds.

3. Using aspirator with pipette tip, lift and place sterilized coverslips into large tissue culture dish and/or 24-microwell plate.

4. Dilute thawed, stock PDL to 150$\mu$g/mL in BBS and vortex.

5. Using a pipette, place 100 $\mu$L or 500 $\mu$L of PDL onto entire surface of Ø12mm or 24x30mm coverslip, respectively. Take care not to spill over edges of coverslip.

6. Place lid on tissue culture plate and leave in biosafety cabinet for overnight.

7. Prepare necessary volume of plating media and maintenance media needed for the next two weeks.

DIV-1: (13 Steps)

1. Using pipette, extract excess PDL from coverslips in tissue culture dish for re-use (max. three times) and aspirate remaining PDL.

2. Rinse coverslips with excess sterilized $ddH_2O$ and ensure no coverslips are adhering to bottom of the tissue culture dish.

3. Swirl tissue culture dish for a few seconds then aspirate $ddH_2O$.

4. Take coverslips and place on rotating plate then, leave for 30 mins.

5. Repeat 2-3 times. On final rinse for 24x30mm coverslips only before aspirating $ddH_2O$, use tweezers to dip coverslips repeatedly into water and carefully aspirate all visible fluid from surface of coverslip then leave propped on edge of lid to fully dry. *Important Note: Take care to ensure the PDL coated side of coverslip remains face up when propped for drying.*

6. Initiate UV cycle in biosafety cabinet and leave tissue culture dish and coverslips to fully dry. If storing for later use, seal tissue culture dish with Parafilm and store at 4°C for at most 2 weeks. If not using microfluidics skip to step 9.

7. Return to biosafety cabinet with microfluidic chambers.

8. Adhere microfluidic chambers by hand assembling to dried coverslips ensuring no air pockets are visible between PDMS and glass interface.

9. Take stock Laminin out of -20°C storage and place in biosafety cabinet to thaw.

10. Once thawed, dilute Laminin to working concentration of 2 $\mu g$/mL with sterile $ddH_2O$.

11. Dilute thawed, stock PDL to 150$\mu$g/mL in BBS and vortex.

12. Using a pipette, place 100 $\mu$L or fille microfluidic well, respectively. Take care not to spill over edges of coverslip.

13. Place lid on tissue culture plate and leave in biosafety cabinet for overnight.

<u>DIV0: (23 Steps)</u>

1. Aspirate excess laminin from surface of coverslips and rinse with $ddH_2O$ once, before leaving coverslips to dry.

2. Once coverslips are dry take plating media and fill all microfluidic chambers or microwells then, place chambers in incubator.

3. Proceed with dissection of necessary tissue to begin genotyping.

4. Proceed with brain tissue collection, storing individual brain samples in micro-cuvettes containing 750 $\mu$L of Hib-E while holding on ice.

5. After dissecting brain tissue, combine tissue of like region and genotype into 15 mL test tube.

6. Aspirate off Hib-E and rinse with HBSS+ repeating process a total of three times. Be cautious not to aspirate tissue, use a 200 $\mu$L pipette to remove the last bit of HBSS+ as necessary. On fourth replacement of HBSS+ add 900 $\mu$L (if more than 3 brains double to 1.8 mL of HBSS+).

7. Add 100 $\mu$L of 10x TrypLE to dissociate tissue.

8. Gently, swirl the tube to expose full surface area of tissue to solution before placing in heat bath for a total 15 mins. Return to re-swirl tissue after 7.5 minutes before removing from heat bath.

9. After removing the brain tissue in solution from the heat bath, return to biosafety cabinet and add 111 $\mu$L of 10x DNAse and gently swirl test tube to dissociate tissue.

10. Using fire-polished glass pipette, begin trituration by mindfully drawing and expelling volume of dissociated cell-suspension without generating bubbles. Repeat until significant breakdown of tissue has occurred and solution is cloudy.

11. Then, add at least 2 mL (2:1/PM:Suspension) of plating media to quench trypsin.

12. Allow tissue in cell-suspension to settle for at least 5 mins.

13. Using a pipette, draw off 300-1500 $\mu$L the supernatant from middle of test tube and place in 15 mL tube.

14. Centrifuge supernatant for 5 mins at 1 krpm.

15. Resuspend sample in 120-500 $\mu$L. May vary depending on required plating volumes.

16. Produce a 20 $\mu$L sample diluted 10x with tryphan blue in Eppendorf tube for counting in hemacytometer. *Recommended: dilute cell suspension by at most 10x as well.*

17. Using cell count, determine dilution needed to attain a cell suspension with plating density yielding a surface density of 500 cells/mm$^2$. Plating volumes will vary and should be determined ahead of time.

18. Remove microfluidic chambers or microwell plates from incubator and pipette all plating media from wells into a test tube then, place in heat bath for later use.

19. Gently mix final cell suspension with pipette, then begin seeding cells onto glass coverslips. *Note: Can check quality of trituration at this step by single seeding and, if necessary, breakdown cell suspension further by trituration using decreasing plastic, pipette tip sizes and shearing along test tube wall.*

20. After seeding, leave tissue dishes sitting in biosafety cabinet for 5 mins to all settling of cells onto coverslips. Take care not to lift or tilt seeded dishes/plates to ensure surface density uniformity of culture. If using microfluidics, fill lid of 50 mL test tube with sterile ddH$_2$O and place into tissue culture dish.

21. Carefully place seeded culture dishes in incubator for 20-30 mins to facilitate cell adhesion onto glass coverslips.

22. Remove seeded culture dishes from incubator and use heat bath incubated plating media to fill microfluidics and/or microwells. Then, leave cultures in incubator overnight.

23. Lastly, place volume of maintenance media equivalent to plating media used into 6-microwell dish and leave in incubator overnight.

DIV1: (3 Steps)

1. Remove maintaence media incubated overnight from incubator and place into biosafety cabinet. *Note: if media is not incubated overnight make sure to incubate media for at least 45 mins prior to media replacement.*

2. Remove cultures from incubator and using a pipette gentlye, remove and discard all plating media then, replace with maintenance media. If using microwell plate then, do this in a row-by-row manner making sure to replace pipette tip before replacing with maintenance media.

3. Return culture dishes to incubator until next media replacement or experiment.

Culture Maintenance:

- Every 48-72 hours, while accounting for evaporation remove half of the current well volume. Then, replace with incubated maintenance media to DIV1 well volume in order to ensure viability until experiment. If culture is in closed microfluidic then, replace media every 48 hours.

- Evaporation in 24-microwell plates varies depending on position of microwell relative to corner or edge. Rate of evaporation for edge positions (A2-5,B1,B6,C1,C6,D2-5) is 25 $\mu$L/day while, corner (A1,A6,D1,D6) and center (B2-5,C2-5) positions are 29 $\mu$L/day and 20 $\mu$L/day, respectively.

- Place a lid from a 50 mL test tube filled with sterile, $ddH_20$ to minimize evaporation in tissue culture dishes. Rates for microfluidics depend on number and well area of microfluidics in tissue culture dish and have an evaporation rate ranging from from 25 – 35 µL/day.

- Transport via 15 min walking trips. Facilitated by or after DIV6 with plates/dishes sealed with parafilm and stored in styrofoam cooler warmed by soaking absorbent cloth paper water incubated to 37°C.

### B.v. Dye Loading for Live-Cell Imaging (Time: 25-40 mins)

Dye loading was performed just before imaging live cells. Both Fluo-4 and Hoechst dyes are incubated in culture wells that are going to be imaged. Generally, cells were incubated before imaging for at least 20 mins following dye loading. Tyrode’s solution is prepared fresh at working concentration on day of experiment from sterilized stock salt solutions or the night before. Tyrode’s solution is used for dye loading solution preparation, rinsing, and as an imaging solution so, prepare at least triple the amount as needed to replace media of desired samples.

Materials:

- Tyrode's Solution (1X)
  - NaCl 129 mM
  - KCl 5 mM
  - $CaCl_2$ 2 mM
  - $MgCl_2$ 1 mM
  - Glucose 30 mM
  - HEPES 25 mM
- Fluo 4 AM 1 mM (50018, Biotium., Fremont, CA).
- Hoechst 33258 10 mg/mL (40044, Biotium., Fremont, CA).
- Probenecid 100X (50027, Biotium, Fremont, CA).
- Powerload™ 100X (P10020, Thermo Fisher Scientific, USA).

Equipment:

- Biosafety cabinet, with UV light cycle.
- Pipettes
- Vortex Mixer
- Incubation chamber set at 37°C with 5% $CO_2$ and humidified.

1. Incubate Tyrode's Solution in incubator overnight or for at least 20 minutes in heath beath at 37$^o$C.

2. Take stock Fluo 4 AM and Probenecid out of -20°C storage and place in biosafety cabinet to thaw.

3. Once thawed, vortex both Fluo 4 AM and Probenecid briefly.

4. Grab Powerload and incubated Tyrode's solution and place in biosafety cabinet.

5. Prepare Fluo 4 loading solution by diluting Fluo 4 AM to 4 $\mu$M, 1% Powerload, 1% Probenecid into Tyrode's solution with enough volume to replace media in all desired culture dishes for imaging.

6. Place cell culture samples in the biosafety cabinet.

7. Then, use a pipette to gently, aspirate the cell media of a well and replace with Fluo 4 loading solution.

8. Repeat as needed for each cell culture sample/well.

9. Then, incubate samples with loading solution for 15 mins in incubation chamber. Also, return Tyrode's solution to incubate as well.

10. Just before the 15 mins are completed, prepare Hoechst loading solution by diluting 0.2 µL of stock Hoechst 33258 per 1 mL of Tyrode's solution.

11. After incubation, place samples in biosafety cabinet.

12. Remove, half the volume per sample and replace with equivalent volume of Hoechst loading solution.

13. Place samples in darkness at room temperature and continue incubating for 15 minutes along with remaining Tyrode's solution.

14. After incubation is complete, return cell samples to biosafety cabinet and replace media with Tyrode's solution.

15. Following incubation at microscope sample stage, cells are now ready for imaging.

## B.vi. PDMS Molding Procedure

Materials:

- Chlorotrimethylsilane (CMS)
- Dow Sylgard™184 Silicone Encapsulant Kit. (PDMS kit)

Equipment:

- 3D-Printed mold
- Wooden stick
- Mixing vessel
- Ø150mm borosilicate bowl
- Vacuum, desiccation chamber
- Conventional oven

*For safety, steps 1-4 must be performed in chemical fume hood*

1. Take clean molding substrate and silanize by placing a few drops of chlorotrimethylsilane (CMS) in a sealed dish.

2. Place in desiccator and immediately open and close vacuum.

3. Leave substrate in vacuum chamber for 15 mins.

4. Unseal vacuum chamber and allow CMS to evaporate for 10 mins.

5. Mix PDMS base with PDMS curing agent at 10:1 ratio in mixing vessel. Use volume to determines desired thickness.

6. Mix vigorously with wooden stick to ensure homogeneity of both reagents.

7. Transfer mold to borosilicate bowl then, pour PDMS mixture over molding substrate.

8. Desiccate for about 20-30mins in order to clear all bubbles from uncured PDMS.

9. Release vacuum and repeat Step 8 until all bubbles are cleared. During the last repetition of Step 8 pre-heat oven to 100°C (212°F) and cure for 35 minutes.

10. Once bubbles are removed from uncured PDMS, remove from desiccator and move to pre-heated oven.

11. After waiting designated cure time, turn off oven and let PDMS mold sit in oven until it cools down to room temperature.

12. PDMS mold is now ready and care should be taken in removing from molding substrate to prevent tearing or damage.